Room 14-0551
77 Massachusetts Avenue
Cambridge, MA 02139
Ph: 617.253.5668 Fax: 617.253.1690
Email: docs@mit.edu
http://libraries.mit.edu/docs

DISCLAIMER OF QUALITY

Due to the condition of the original material, there are unavoidable flaws in this reproduction. We have made every effort possible to provide you with the best copy available. If you are dissatisfied with this product and find it unusable, please contact Document Services as soon as possible.

Thank you.

Some pages in the original document contain pictures or graphics that will not scan or reproduce well.

Surface Kinetics Modeling of Silicon Oxide Etching in Fluorocarbon Plasmas

by

Ohseung Kwon

B.S. Materials Science and Engineering
Korea Advanced Institute of Science and Technology (1991)

M.S. Electronic Materials Engineering
Korea Advanced Institute of Science and Technology (1993)

S.M. Materials Science and Engineering
Massachusetts Institute of Technology (1999)

Submitted to the Department of Materials Science and Engineering
in Partial Fulfillment of the Requirements for the Degree of

DOCTOR OF SCIENCE IN MATERIALS SCIENCE AND ENGINEERING
AT THE
MASSACHUSETTS INSTITUTE OF TECHNOLOGY

June 2004

© 2004 Massachusetts Institute of Technology, All rights reserved

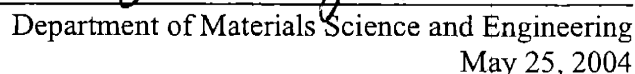

Signature of Author ______________________________
Department of Materials Science and Engineering
May 25, 2004

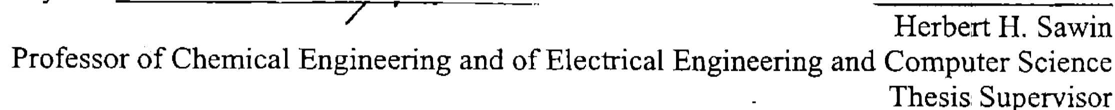

Certified by ______________________________
Herbert H. Sawin
Professor of Chemical Engineering and of Electrical Engineering and Computer Science
Thesis Supervisor

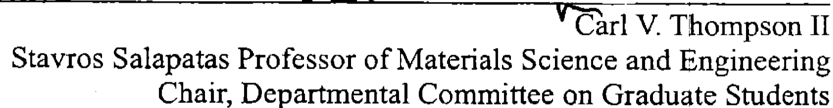

Accepted by ______________________________
Carl V. Thompson II
Stavros Salapatas Professor of Materials Science and Engineering
Chair, Departmental Committee on Graduate Students

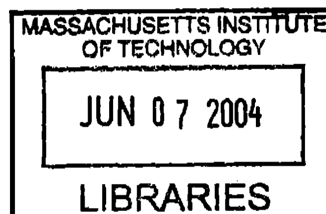
MASSACHUSETTS INSTITUTE OF TECHNOLOGY
JUN 07 2004
LIBRARIES

ARCHIVES

Surface Kinetics Modeling of
Silicon Oxide Etching in Fluorocarbon Plasmas

by

Ohseung Kwon

Submitted to the Department of Materials Science and Engineering on April 30, 2004
in Partial Fulfillment of the Requirements for the Degree of
Doctor of Science in Materials Science and Engineering

Abstract

Fluorocarbon plasma for silicon oxide etching is a complicated system involving many ion and neutral species. Depending on the plasma condition, many difficulties arise such as RIE lag, etch stop, and low selectivity to photoresist. For a better understanding of the process it is necessary to have an appropriate physical model to describe the surface kinetics including simultaneous etching and deposition.

A novel surface kinetic model, the translating mixed-layer (TML) model, has been developed. ABACUSS II, a modeling environment and simulator was used for solving differential algebraic equations that describes the surface kinetics. In the modeling, the effect of many variables were investigated including neutral and ion fluxes to the surface, sticking probabilities, surface composition, sputter etching reactions, ion enhanced chemical etching reactions and neutral-to-ion flux ratio.

The model has been applied to various systems including silicon etching with chlorine chemistry, silicon oxide etching with fluorine chemistry and silicon oxide etching with fluorocarbon plasma.

The verification of the model was done using measured etching yield data determined by quartz crystal microbalance (QCM) in conjunction with plasma neutral and ion concentrations/fluxes determined by mass spectrometry.

The etching and deposition rates have been measured as functions of ion impinging angle, sample temperature, which are necessary for profile evolution modeling of silicon oxide etching in inductively coupled plasma. Angular dependence of etching yield of oxide in fluorocarbon plasma shows very unique behavior unlike typical ion-induced chemical etching or physical sputtering. Ion-induced deposition model was suggested and tested.

Thesis Supervisor: Herbert H. Sawin

Title: Professor of Chemical Engineering and Electrical Engineering and Computer Science

Table of Contents

Chapter 1. Introduction 17

1.1 Plasma Processes in Semiconductor Fabrication 17

1.2 Silicon Oxide Etching with Fluorocarbon Plasmas 19

1.3 Modeling of Silicon Oxide Etching in Fluorocarbon Plasmas 21

1.4 Angular Dependence of Oxide Etching Yield 22

1.5 Post-Oxide Etching Dry Cleaning 23

1.6 Goal of the Research 24

1.7 References 25

Chapter 2. Measurement 29

2.1 Experimental 29

2.1.1 Inductively-coupled plasma (ICP) reactor 29

2.1.2 Quartz crystal microbalance (QCM) and chamber 31

2.1.3 Mass Spectrometer and Chamber 33

2.2 Surface plot: oxide etching yield as a function of incoming flux 35

2.3 Result and Discussion 37

2.3.1 C_2F_6 chemistry with varying RF coil power 38

2.3.2 C_2F_6 chemistry with varying operating pressure 43

2.3.3 C_4F_8 + 80% Ar chemistry with varying RF coil power 50

2.3.4 C_4F_8 + 80% Ar chemistry with varying operating pressure 55

2.4 Conclusion 61

2.5 References 61

Chapter 3. Translating Mixed-Layer (TML) Model 63

3.1 Translating Mixed-Layer (TML) Model 64
3.2 Silicon etching with chlorine chemistry 67
3.3 Silicon Oxide Etching with Fluorine Chemistry 72
3.4 Conclusion 76
3.5 REFERENCE 77
Chapter 4. Modeling of Silicon Oxide Etching in Fluorocarbon Chemistry 79
4.1 Translating Mixed-Layer (TML) Model 79
4.2 Determining Kinetic Parameters 86
4.3 Result and Discussion 88
4.3.1 CF_2-F surface plot 88
4.3.2 Verification of the model with measured data sets 89
4.3.3 A new surface plot – etching yield as a function of the composition in the translating mixed-layer 92
4.3.4 Effect of plasma variables 93
4.4 Conclusion 99
4.5 References 99
Chapter 5. Angular Dependence of Oxide Etching Yield in Fluorocarbon Chemistries . 101
5.1 Experimental 102
5.2 Result and Discussion 103
5.2.1 Effect of angular dependent etching yield on feature profile 103
5.3 Etching Yield vs. Ion Bombardment Energy 107
5.4 A Simple Model: Combined Ion-Induced Chemical Etching Yield and Isotropic Deposition 108
5.5 An Improved Model: Combined Ion-Induced Chemical Etching and Ion-Induced

Deposition ... 109

5.6 Conclusion ... 112

5.7 References ... 113

Chapter 6. Post Oxide Etching Cleaning ... 115

6.1 Apparatus ... 117

6.1.1 Integrated Process Apparatus (VAST tube: VAcuum Sample Transfer tube) .. 117

6.1.2 Inductively Coupled Plasma (ICP) Etcher ... 117

6.1.3 HF Vapor Cleaning Chamber ... 119

6.2 Experimental Procedure ... 120

6.2.1 Etching ... 121

6.2.2 Oxygen Plasma Cleaning ... 121

6.2.3 HF Vapor Cleaning ... 121

6.2.4 Sputter Cleaning ... 122

6.2.5 XPS Analysis ... 122

6.2.6 Contact Resistance Measurement ... 124

6.3 RESULTS AND DISCUSSION ... 125

6.3.1 Cleaning Planer Silicon Surface ... 125

6.3.2 Cleaning Line and Space Structure ... 126

6.3.3 Contact Resistance Measurement ... 128

6.4 Conclusion ... 132

6.5 References ... 132

Chapter 7. Conclusion ... 135

7.1 Summary of the work ... 135

7.2 Future Work ... 137

Appendix. ABACUSS II code 139

Silicon Etching with Chlorine Chemistry 139

Silicon Oxide Etching with Fluorine Chemistry 142

Silicon Oxide Etching with Fluorocarbon Chemistry 146

Mass Spectrometry Data 159

C_2F_6, 300 W RF coil power, varying pressure 159

C_2F_6, 5 mTorr, varying RF power 160

C_4F_8 + 80% Ar, 300 W RF coil power, varying pressure 161

C_4F_8 + 80% Ar, 5 mTorr, varying RF coil power 162

List of Figures

Figure 1.1 Dramatic decrease of DRAM 1/2 pitch and MPU Gate length 17

Figure 1.2 Schematic Diagram of Plasma Etching Process 18

Figure 2.1 Integrated processing system. 30

Figure 2.2 Schematic diagram of inductively-coupled plasma etcher 31

Figure 2.3 Schematic diagram of quartz crystal microbalance (QCM) chamber. 32

Figure 2.4 Sensitivity of mass spectroscopy measurement varying with molecular mass in amu. 34

Figure 2.5 Ionization efficiency of the mass spectrometer. 35

Figure 2.6 Oxide etching yield measured with three beams (CF_2, F and Ar^+)[2]. 36

Figure 2.7 Modified surface plot with deposition chemistry. 37

Figure 2.8 Etching yield as a function of RF coil power for C_2F_6 chemistry. 5 m Torr operating pressure, 300 eV DC bias. 38

Figure 2.9 Neutral composition change in C_2F_6 plasma with varying RF coil power at 5 mTorr operating pressure. (a) Neutral compositions. (b) F/C ratio in the neutral flux. 39

Figure 2.10 Ion current and ion-to-neutral flux ratio with varying RF coil power. C_2F_6 plasma, 5 mTorr operating pressure, 300 eV DC bias. (a) Total ion current and overall neutral-to-ion flux ratio. (b) Flux ratios for neutral gas species 40

Figure 2.11 Change in ion composition with varying RF coil power. C_2F_6 plasma, 5 mTorr operating pressure. (a) Mass spectrometry signal. (b) F/C ratio in the ion flux. 41

Figure 2.12 Qualitative representation of etching yield change with RF coil power in C_2F_6 chemistry. 42

Figure 2.13 Etching yield as a function of operating pressure for C_2F_6 chemistry. 300W RF coil power, 300 eV ion energy. 44

Figure 2.14 Neutral composition change in C_2F_6 plasma with varying operating pressure 300 W RF coil power. (a) Neutral compositions. (b) F/C ratio in the neutral flux.. 45

Figure 2.15 Ion current and neutral-to-ion flux ratio with varying operating pressure. C_2F_6 plasma, 300 W RF coil power, 300 eV DC bias. (a) Total ion current and overall neutral-to-ion flux ratio. (b) Flux ratios for neutral gas species. 46

Figure 2.16 Change in ion composition with varying operating pressure. C_2F_6 plasma, 300 W RF coil power. (a) Mass spectrometry signal. (b) F/C ratio in the ion flux. 47

Figure 2.17 Qualitative representation of etching yield change with operating pressure in C_2F_6 chemistry. 48

Figure 2.18 Etching yield as a function of RF coil power for C_4F_8 + 80% Ar chemistry. 50

Figure 2.19 Neutral composition change in C_4F_8 + 80% Ar plasma with RF coil power at 5 mTorr of pressure. (a) Neutral compositions. (b) F/C ratio in the neutral flux. ... 51

Figure 2.20 Ion current and neutral-to-ion ratio with varying RF coil power. C_4F_8 + 80% plasma, 5 mTorr operating pressure, 300 eV DC bias. (a) Total ion current and overall neutral-to-ion flux ratio. (b) Flux ratios for neutral gas species. 52

Figure 2.21 Change in ion composition with varying RF coil power. C_4F_8 + 80% Ar plasma, 5 mTorr operating pressure. (a) Mass spectrometry signal. (b) F/C ratio in thc ion flux. 53

Figure 2.22 Qualitative representation of etching yield change with RF coil power in

C_4F_8 + 80% Ar chemistry.......... 55

Figure 2.23 Etching yield as a function of operating pressure for C_4F_8 + 80% Ar chemistry. 300 W RF coil power, 300 eV ion energy.......... 56

Figure 2.24 Neutral composition change in C_4F_8 + 80% Ar plasma with varying operating pressure 300 W RF coil power. (a) Neutral compositions. (b) Neutral-to-ion flux ratios.......... 57

Figure 2.25 Ion current and neutral-to-ion flux ratio with varying operating pressure. C_4F_8 + 80% Ar plasma, 300 W RF coil power, 300 eV DC bias. (a) Total ion current and overall neutral-to-ion flux ratio. (b) Flux ratios for neutral gas species.......... 58

Figure 2.26 Change in ion composition with varying operating pressure. C_4F_8 + 80% Ar plasma, 300 W RF coil power. (a) Mass spectrometry signal. (b) F/C ratio in the ion flux.......... 59

Figure 2.27 Qualitative representation of etching yield change with operating pressure in C_4F_8 + 80% Ar chemistry.......... 60

Figure 3.1 A graphical illustration of an active-site model for silicon etching with chlorine chemistry.......... 64

Figure 3.2 A graphical illustration of a translating mixed-layer model.......... 66

Figure 3.3 Translating mixed-layer simulation for silicon etching with chlorine chemistry, compared with experimental data and a Monte-Carlo simulation result. Ion energy is 100 eV.......... 70

Figure 3.4 A translating mixed-layer model calculation result for silicon oxide etching with fluorine chemistry compared with experimental data. Ion bombardment energy is 350 eV.......... 76

Figure 4.1 A flow diagram for determining kinetic parameters of oxide etching in

fluorocarbon chemistry. 86

Figure 4.2 A translating mixed-layer simulation result compared with experimental data for oxide etching with F and CF_2. 88

Figure 4.3 Translating mixed-layer simulation results compared with measured data for two chemistries. (C_2F_6 and C_4F_8 + 80% Ar) (a) C_2F_6 chemistry, varying operating pressure. (b) C_2F_6 chemistry, varying RF coil power. (c) C_4F_8 + 80%Ar chemistry, varying RF coil power. 90

Figure 4.4 Calculated etching yield as a function of carbon and fluorine concentration in the moving boundary layer. (a) Surface plot. (b) Connected wire plot showing results for C_2F_6 and C_4F_8 + 80% Ar chemistry. Under most etching conditions, the etching yield falls in the oval region. The data points represent simulation results with the following conditions: C_2F_6 plasma, 5 mTorr, 200-500 W RF coil power; C_2F_6 plasma, 300 W RF coil power, 5-20 mTorr; C_4F_8 + 80% Ar plasma, 5 mTorr, 200-500 W RF coil power. 91

Figure 4.5 Etching yield vs. carbon concentration in the translating mixed-layer at fluorine concentration of 0.3. 92

Figure 4.6 Effect of neutral composition on etching yield. 94

Figure 4.7 Effect of neutral-to-ion flux ratio on etching yield for (a) C_2F_6–like chemistry with 25% atomic fluorine in the neutral flux. (b) C_4F_8 + 80%-like Ar chemistry with 0.3% atomic fluorine in the neutral flux. 95

Figure 4.8 Effect of ion composition on etching yield for (a) C_2F_6–like chemistry with 25% atomic fluorine in the neutral flux. (b) C_4F_8 + 80%-like Ar chemistry with 0.3% atomic fluorine in the neutral flux. 95

Figure 4.9 Effect of ion composition on etching yield with varying CF_4 production rate

coefficient (α). (a) Etching yield change with ion composition for different alpha values. (b) slope of the curves in (a) with varying alpha. 97

Figure 4.10 Effect of F, CF, CF_2 and CF_3 on etching yield for C_2F_6 and C_4F_8 + 80% Ar chemistries. 98

Figure 5.1 A schematic diagram of the plasma beam / QCM apparatus. 102

Figure 5.2. Monte Carlo simulation result where the angular dependence of etching yield curve is independent of ion incident angle. (a) Angular dependence of etching yield curve. (b) Feature profile simulation result. 104

Figure 5.3. Monte Carlo simulation result where the angular dependence of etching yield curve shows a typical ion-induced chemical etching characteristics without ion scattering. (a) Angular dependence of etching yield curve. (b) Feature profile simulation result. 104

Figure 5.4. Monte Carlo simulation result where the angular dependence of etching yield curve shows a typical ion-induced chemical etching characteristics with ion scattering. (a) Angular dependence of etching yield curve. (b) Feature profile simulation result. 105

Figure 5.5. Monte Carlo simulation result where the angular dependence of etching yield curve shows a typical ion-induced chemical etching characteristics with isotropic deposition. (a) Angular dependence of etching yield curve. (b) Feature profile simulation result. 106

Figure 5.6. Oxide etching yield vs. ion bombardment energy. CHF_3 plasma, 5 mTorr, $20^{\circ}C$ sample temperature, 400 W RF source power. 107

Figure 5.7. A model for angular dependence of oxide etching yield curve. Ion-induced chemical etching and isotropic etching are assumed. 109

Figure 5.8 (a) Oxide etching yield curves according to the simple model with ion-induced chemical etching and isotropic deposition. (b) Oxide etching yield curves measured. 110

Figure 5.9 Oxide etching yield curves measured at two different temperatures. CHF_3, 5mTorr, 300 eV ion energy, 400 W source power. (a) 20 °C (b) –10°C. 111

Figure 5.10 Comparison of model fit with measured angular dependent etching yield curve. (a) Temperature variation. (b) Chemistry variation. 112

Figure 6.1 A schematic diagram of contamination and damage after a typical plasma etching process 115

Figure 6.2 A schematic diagram of the Integrated Process Apparatus VAST tube (VAcuum Sample Transfer tube). 117

Figure 6.3 A schematic diagram of inductively coupled plasma etcher used in this research 118

Figure 6.4 A schematic diagram of HF vapor cleaning apparatus. 119

Figure 6.5 A schematic diagram of contaminated/damaged films and the removal procedure. 120

Figure 6.6 Condensation and non-condensation regimes in HF vapor etching[14]. 122

Figure 6.7 A Schematic diagram of angle resolved XPS showing normal take-off angle and 25-degree take-off angle 124

Figure 6.8 Contact chain structure used for measuring contact resistance.... 124

Figure 6.9 A histogram showing amount of carbon, oxygen and fluorine contamination left on the surface after each process step. 125

Figure 6.10 XPS spectra showing carbon contamination on the surface after each processing step. (a) Normal take-off angle. (b) 25 degree take-off angle. 127

Figure 6.11 Contact resistance and standard deviation for a chain of 50 contacts with 1.0 μm contact size. The contact resistance values shown are for 50 contacts. The chain measurement voltage was 3 V. The minimum expected contact chain resistance assuming 'ideal' contacts is 1.75 kΩ. 130

Figure 6.12 Contact resistance and standard deviation for a chain of 50 contacts with 1.5 μm contact size. The contact resistance values shown are for 50 contacts. The chain measurement voltage was 3 V. The minimum expected contact chain resistance assuming 'ideal' contacts is 1.47 kΩ. 131

List of Tables

Table 1.1 Typical chemical and water consumption in a semiconductor manufacturing facility producing 200,000 of 8" wafers per month (as of 1999). 24

Table 3.1 List of symbols used in equations.......... 66

Table 3.2 Kinetic parameters used for the translating mixed-layer model compared with parameters for the active-site model[3] in modeling silicon etching with chlorine chemistry. Ion energy is 100 eV.......... 71

Table 3.3 Kinetic parameters used for the translating mixed-layer model compared with parameters for the active-site model[4] in modeling silicon oxide etching with fluorine chemistry. Ion bombardment energy is 350 eV.......... 75

Table 4.1 List of symbols used in equations.......... 80

Table 4.2 Adsorption Reactions of silicon oxide etching with fluorocarbon chemistry. . 81

Table 4.3 The lumped etching reactions.......... 83

Table 4.4 Kinetic parameters of translating mixed-layer model for silicon oxide etching in fluorocarbon plasmas. Ion energy is 300 eV.......... 87

Chapter 1. Introduction

1.1 Plasma Processes in Semiconductor Fabrication

Since the beginning of the integrated circuit (IC) era in 1958, technology has been advancing tremendously. The size of a chip has been shrunk exponentially. The speed of these chips has been improved as the length scale has drastically decreased. Figure 1.1 shows a ITRS roadmap showing the projected exponential decrease in feature scale for next 10 years[1].

To fabricate microelectronic devices, many processes are used and plasma etching processes are essential for pattern transfers. About 40% of the steps in the fabrication of microelectronics require the use of plasma processes.

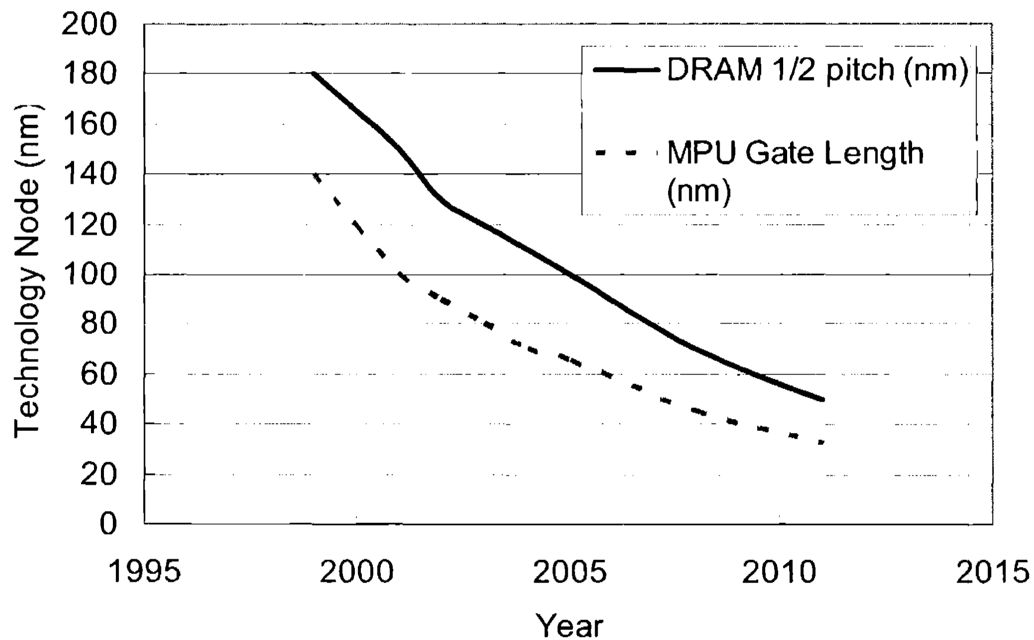

Figure 1.1 Dramatic decrease of DRAM 1/2 pitch and MPU Gate length[1].

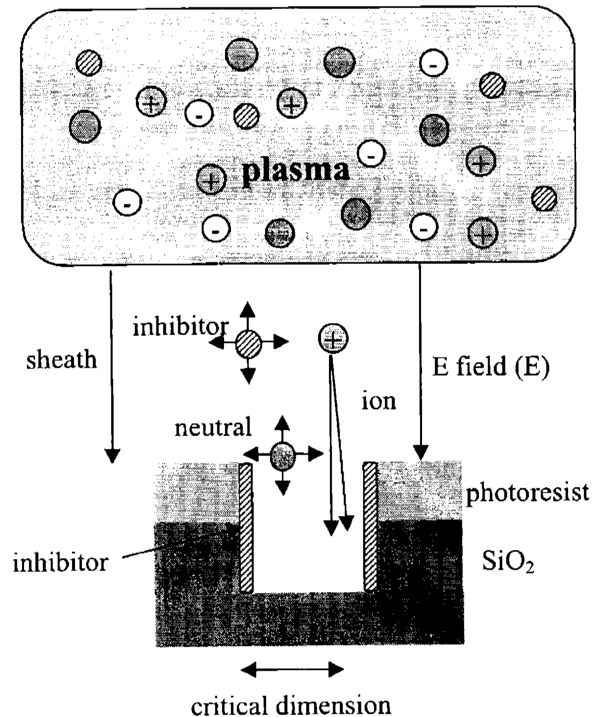

Figure 1.2 Schematic Diagram of Plasma Etching Process.

Figure 1.2 is a schematic diagram of a typical plasma processing used in semiconductor fabrication. Plasma is a partially ionized gas containing ions, electrons, and neutrals. Various reactive ions and neutrals are generated in plasma by electron impact reactions. Reactive ions are accelerated by an electric field in the sheath region. These energetic and directional ions make anisotropic etching possible, which is critical in semiconductor processing. Etching inhibitors are often generated in plasmas to deposit polymer layers on sidewall and bottom of features and intentionally used to achieve good etching selectivity, especially in dielectric material etching using fluorocarbon chemistries.

1.2 Silicon Oxide Etching with Fluorocarbon Plasmas

For silicon oxide etching, various fluorine containing compounds and their mixtures are used. It has been known that fluorine is very effective in etching silicon oxide film. Fluorocarbon chemistries that inherently have simultaneous etching and deposition are usually used for oxide patterning. Although deposition component in the fluorocarbon chemistry makes the process complicated, deposition chemistries are intentionally used to control the feature profile.

It has been reported that etching and deposition characteristics of silicon oxide etching with fluorocarbon chemistry can be determined by F/C ratio of the feed gas species and applied bias[2]. Typical oxide etching uses the parameter space which is close to the transition line between the etching regime and the deposition regime. Under these conditions, the top and the bottom of the feature with more ion bombardment are in the net etching regime while polymeric deposition is build up on the sidewalls because of less ion bombardment to be in the net deposition regime. By carefully designing the process and utilizing the sidewall deposition, desired feature profile with vertical sidewall can be achieved.

If not controlled adequately, however, oxide etching process may show many undesired phenomena and artifacts including tapered sidewall, bowed sidewall, micro trenching, etch stop, RIE lag, inverse RIE lag, etc.

Among the major phenomena to consider for etching processes, there are etching selectivity, uniformity, anisotropic etching, and etching rate. Selective etching is one of the major issues when pattern transfer is made. In general, selective etching of SiO_2 films over Si, Si_3N_4, or photoresist has been achieved by making plasma generate more polymer precursors (CF_x, x=1-3). Hydrogen is often added or feed gases of high C/F ratio are used to increase

fluorocarbon polymer precursors. Thick fluorocarbon film is formed on Si surfaces while little film is formed on SiO_2 surfaces during plasma etching[3].

It is known that H radicals combine with F to form HF, reducing the concentration of F, the major etchant for Si, and increasing the concentration of polymer precursors[2]. Also it is believed that the oxygen in the SiO_2 film combines with the carbon on the surface forming volatile species and reduces fluorocarbon polymer on oxide surfaces.

In plasma etching processes, the high degree of dissociation causes production of more fluorocarbon deposition precursors (CF_x) and the fluorocarbon films thickness on the SiO_2 surface is around 10 – 20 Å. Rueger *et al.*[4] and Schaepkens *et al.*[5] showed a general trend that substrate etch rate of Si, SiO_2 and Si_3N_4 is inversely proportional to the thickness of fluorocarbon films on the surfaces. Most of these studies show oxide etching rate at flat surfaces. However, for the profile control, etching characteristic of inside feature is important but many phenomena are not understood yet.

Fluorocarbon high-density plasmas are being used in silicon dioxide etching due to high etching rate, better directionality of ions, and low device damage. As copper is integrated in devices recently, dual damascene processing is becoming popular and the demand for better feature control of dielectric materials increased. As feature dimensions have decreased and aspect ratio of depth/width has increased, etching rate dependence on aspect ratio becomes a large concern in industry. The dependence of etching rate on feature dimensions has been referred as reactive ion etching (RIE) lag, or aspect ratio dependent etching (ARDE). It is called RIE lag when etching rate reduces as the aspect ratio of depth/width increases and inverse RIE lag when etching rate increases[6-9]. Many factors are known to be involved in RIE lag or inverse RIE lag. Those factors include transport of neutrals, ion shadowing, neutral shadowing, and differential charging of the insulating microstructure[8]. With oxide etching in inductively-coupled

plasmas, the fluorocarbon deposition rate is determined from transport of polymer precursors and ions inside the microstructure and could be an important factor to determine the oxide etching characteristics.

1.3 Modeling of Silicon Oxide Etching in Fluorocarbon Plasmas

Traditionally, the active site model[10-12] approach has been used to model etching surface kinetics. This simple modeling approach works well for simpler system such as silicon etching with chlorine chemistry. In this model, the number of silicon atoms is assumed constant. The generation of Si atoms as etching occurs is associated with the assumed flux of silicon into the surface as this layer moves into the surface during silicon etching. The number of atoms (and therefore thickness) in the layer is a function of the extent of halogenation θ. Because of these assumptions it is impossible to handle deposition and is very difficult if not impossible to model etching with multiple etching species. Although the deposition phenomena itself can be handled using the active site model approach assuming a lumped surface reaction[13], the simultaneous etching and deposition cannot be handled using a simple active site model.

When silicon oxide etching in fluorocarbon chemistry has been modeled, it has been assumed that there is a finite thickness of fluorocarbon film on oxide surface[4,5,14-16]. Zhang *et al.*[16] assumed that fluorine and other species diffuse through the steady-state film to have etching reactions at the interface between the fluorocarbon film and the oxide. Rueger *et al.*[4] suggested that the deposited fluorocarbon layer, which has a finite thickness, reacts with oxide. Schaepkens *et al.*[5] modeled silicon oxide etching in fluorocarbon chemistry using a steady-state fluorocarbon film model showing etching yield is inversely proportional to the steady-state fluorocarbon

thickness. Tatsumi *et al.*[14] attributed lower etching rate with thicker fluorocarbon film to the ion bombardment energy loss.

During plasma etching processes, however, surface reactions do not occur at the very top layer of the surface with a finite thickness of fluorocarbon film: There is a finite volume where all the reactions occur including adsorption, desorption, etching surface reaction. The thickness of the reaction volume can be as much as about 10 monolayers or 30-40 Å, depending on experimental conditions[17,18].

In addition, the assumption of atomic fluorine being the major etchant cannot be justified when atomic fluorine concentration is very low, for example, C_4F_8 chemistry, which is described in Chapter 2

In this thesis, a novel surface kinetics modeling technique is developed, which can be applied to fluorocarbon chemistry with simultaneous etching and deposition using an assumption of 'well-mixed' surface layer.

1.4 Angular Dependence of Oxide Etching Yield

Recently, plasma etching feature profile modeling tools have been developed by several research groups and were able to capture many of the effects seen in real operating plasma conditions[18-23]. These modeling tools, however, cannot be used properly without adequate measurements of experimental parameters. Angular dependence of silicon oxide etching yield is one of the most significant experimental parameters that should be determined.

There have been a number of beam studies using neutral and ion beam systems to measure etching yields. In these systems, separate ion and neutral beams were used to mimic a real plasma[12,24-26]. This approach is relatively easy for simple ion-induced chemical etching

processes, such as silicon etching with chlorine plasma because there are only a few ion and neutral species involved with the process. In oxide etching process, however, it is difficult to make a beam experimental system to simulate a real plasma for there are many chemical species involved including polymerizing neutrals.

There have been several investigations on angular dependence of oxide etching yield[15,24,27-31]. But these measured angular dependence of etching yields show disagreements: some of them show sputtering-like angular dependence[15,27-31] while others reported both ion-induced chemical etching characteristics and sputtering-like characteristics[24].

In oxide etching with fluorocarbon plasma, measurement is very sensitive to many experimental parameters including surface temperature, ion-to-neutral flux ratio, ion scattering, etc. Therefore, in order to make a precise measurement representing a real plasma process, these parameters must be controlled accurately. The variation of the previous measurements done by several research groups may be attributed to the variation of experimental conditions under which the measurements were conducted.

In this research, angular dependence of oxide etching yield has been measured accurately and a surface kinetic model to explain the uniqueness of the shape of the yield curve.

1.5 Post-Oxide Etching Dry Cleaning

Wafer cleaning processes have become more important as the critical size of microelectronic devices shrink.

Traditionally, wet cleaning processes have been used. The wet cleaning processes, however, have many drawbacks. Firstly, drying of the rinse water after the cleaning process is a difficult task, especially with small-scale devices.[32] Secondly, wet benches are one of the largest

machines in a cleanroom, occupying up to 1/3 of the total cleanroom area. If a dry cleaning process is employed the size of the cleanroom may be reduced, significantly saving the initial investment cost.[33] Finally, wet cleaning process use large amount of high purity chemicals and DI water, which are very costly, as shown in Table 1.1.

In this thesis, a new vacuum-integrated post oxide etching dry cleaning process has been proposed and demonstrated for a next generation semiconductor processing.

Table 1.1 Typical chemical and water consumption in a semiconductor manufacturing facility producing 200,000 of 8" wafers per month (as of 1999).

Chemical	Consumption
Water	23,000,000 gal/month
H_2SO_4	10,000 gal/month
NH_4OH	3,500 gal/month
HF	4,000 gal/month
H_2O_2	13,000 gal/month

1.6 Goal of the Research

The goal of this research is to provide insight to reaction kinetics of oxide plasma etching with fluorocarbons in various conditions.

A profile evolution modeling approach has been studied to predict feature profiles and provided useful insights to many difficulties such as RIE lag, inverse RIE lag, bowing, trenching, faceting and so on. This approach, however, requires a set of kinetic parameters with a proper surface kinetic model. Many beam experiments have been used to determine etching yields in

relatively simple chemistries[11,12,34-36], but silicon oxide etching with fluorocarbon plasmas is too complicated for the beam study because many species are involved in the etching process.

The objectives of this research are:

1. To develop a surface kinetic model which can handle simultaneous etching and deposition.
2. To develop a new general modeling approach which can be applied to other systems than silicon oxide etching.
3. To understand the surface kinetics.
4. To measure and characterize the experimental condition which can be used in a feature profile simulator.

1.7 References

1 ITRS, ITRS roadmap (2001).

2 J. W. Coburn, J. Appl. Phys. **50** (8), 5210 (1979).

3 G. S. Oehrlein and H. L. Williams, J. Appl. Phys. **62** (2), 662 (1987).

4 N. R. Rueger, J. J. Beulens, M. Schaepkens et al., J. Vac. Sci. Technol. A **15** (4), 1881 (1997).

5 M. Schaepkens, T.E.F.M. Standaert, N.R. Rueger et al., J. Vac. Sci. Technol. A **17** (1), 26 (1999).

6 A. D. Bailey and R. A. Gottscho, Jpn. J. Appl. Phys. Pt 1 **34** (4B), 2083 (1995).

[7] T. Akimoto, H. Nanbu, and E. Ikawa, J. Vac. Sci. Technol. B **13** (6), 2390 (1995).

[8] R. A. Gottscho, C. W. Jurgensen, and D. J. Vitkavage, J. Vac. Sci. Technol. B **10** (5), 2133 (1992).

[9] M. F. Doemling, N. R. Rueger, and G. S. Oehrlein, Appl. Phys. Lett. **68** (1), 10 (1996).

[10] J. W. Butterbaugh, D. C. Gray, and H. H. Sawin, J. Vac. Sci. Technol. B **9** (3), 1461 (1991).

[11] J. P. Chang and H. H. Sawin, J. Vac. Sci. Technol. A **15** (3), 610 (1997).

[12] D. C. Gray, I. Tepermeister, and H. H. Sawin, J. Vac. Sci. Technol. B **11** (4), 1243 (1993).

[13] H. Chae, S. A. Vitale, and H. H. Sawin, J Vac Sci Technol A **21** (2), 381 (2003).

[14] T. Tatsumi, M. Matsui, M. Okigawa et al., J. Vac. Sci. Technol. B **18** (4), 1897 (2000).

[15] M. Schaepkens, G. S. Oehrlein, C. Hedlund et al., J. Vac. Sci. Technol. A **16** (6), 3281 (1998).

[16] D. Zhang and M. J. Kushner, J. Vac. Sci. Technol. A **19** (2), 524 (2001).

[17] C. F. Abrams and D. B. Graves, IEEE Trans. Plasma Sci. **27** (5), 1426 (1999).

[18] A. P. Mahorowala and H. H. Sawin, J. Vac. Sci. Technol. B **20** (3), 1064 (2002).

[19] J. P. Chang, A. P. Mahorowala, and H. H. Sawin, J. Vac. Sci. Technol. A **16** (1), 217 (1998).

[20] R. J. Hoekstra, M. J. Grapperhaus, and M. J. Kushner, J. Vac. Sci. Technol. A **15** (4), 1913

(1997).

[21] Barbara Abraham-Shrauner, J. Vac. Sci. Technol. B **17** (1), 158 (1999).

[22] A. P. Mahorowala and H. H. Sawin, J. Vac. Sci. Technol. B **20** (3), 1077 (2002).

[23] A. P. Mahorowala and H. H. Sawin, J. Vac. Sci. Technol. B **20** (3), 1084 (2002).

[24] T. M. Mayer, R. A. Barker, and L. J. Whitman, J. Vac. Sci. Technol **18** (2), 349 (1981).

[25] J. W. Butterbaugh, D. C. Gray, and H. H. Sawin, J. Vac. Sci. Technol. B **9** (3), 1461 (1991).

[26] J. W. Coburn and H. F. Winters, J. Appl. Phys. **50** (5), 3189 (1979).

[27] S. Matsui, T. Yamato, H. Aritome et al., Jpn. J. Appl. Phys. **19** (3), L126 (1980).

[28] A. M. Barklund and H. O. Blom, J. Vac. Sci. Technol. A **11** (4, pt.1), 1226 (1993).

[29] B. O. Cho, S. W. Hwang, G. R. Lee et al., J Vac Sci Technol A **18** (6), 2791 (2000).

[30] D. P. Hamblen and A. Cha Lin, J. Electrochem. Soc **135** (7), 1816 (1988).

[31] C. Hedlund, C. Strandman, I. V. Katardjiev et al., J. Vac. Sci. Technol. B **14** (5), 3239 (1996).

[32] M. R. Baklanov, E. Kondoh, R. A. Donaton et al., J. Electrochem. Soc **145** (9), 3240 (1998).

[33] Y-P. Han, Ph.D. thesis, Massachusetts Institute of Technology, 1999.

[34] T. M. Mayer and R. A. Barker, J. Vac. Sci. Technol **21** (3), 757 (1982).

[35] T. M. Mayer and R. A. Barker, J. Electrochem. Soc **129** (3), 585 (1982).

[36] R. A. Barker, T. M. Mayer, and W. C. Pearson, J. Vac. Sci. Technol. B **1** (1), 37 (1983).

Chapter 2. Measurement

Fluorocarbon high-density plasmas are used in silicon dioxide etching due to high etching rate, better directionality of ions, and low device damage. As copper is integrated in devices recently, dual damascene processing is becoming popular and the demand for better feature control of dielectric materials increases. As feature dimensions have decreased and aspect ratio of depth/width has increased, etching rate dependence on aspect ratio becomes a large concern in industry.

Understanding the oxide etching processes, however, is complicated because of the complex nature of fluorocarbon chemistry. In this study, the relationship between the plasma chemistry and the etching yield is investigated using an inductively coupled plasma etcher with a mass spectrometry and quartz crystal microbalance (QCM).

2.1 Experimental

2.1.1 Inductively-coupled plasma (ICP) reactor

An inductively-coupled plasma etcher has been used as a high-density plasma source for studying surface kinetics of oxide etching in fluorocarbon chemistry. Two side chambers, a mass spectrometer chamber and a quartz crystal microbalance (QCM) chamber, are attached to the main plasma etcher and both of them are pumped differentially using turbo-molecular pumps.

The main chamber is connected to a central sample transfer tube, of which pressure is $\sim 10^{-9}$ Torr. The entire sample transfer system is designed so that samples can be transferred between chambers without being exposed to the air to prevent contamination. (Figure 2.1)

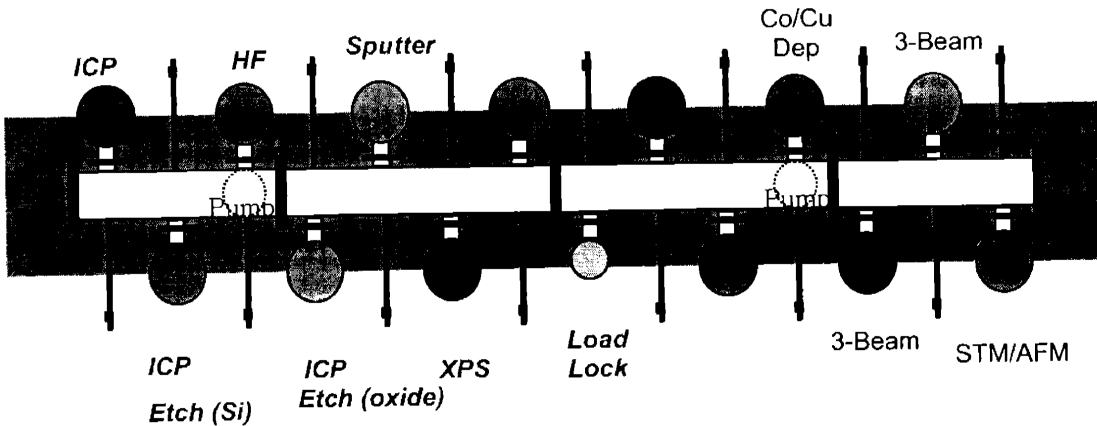

Figure 2.1 Integrated processing system.

Plasma is inductively generated by 13.56 MHz RF power (0-500 W) through the inductive coil placed on a 8 inch diameter quartz bell jar. Both ions and neutrals are extracted though extraction grids between the main etching chamber and QCM or mass spectrometer side chamber. The main etching chamber can accommodate a 4 inch wafer. The substrate can be biased using a 13.56 MHz RF power (0-200 W). The sample is cooled by electrostatic clamping and backside helium of which pressure is 5 Torr (Figure 2.2). The base pressure is maintained below 10^{-6} Torr, and typical operating pressure is 5-50 mTorr. The main etching process chamber is pumped by a 240 l/s turbomolecular pump, backed by a corrosive roots blower.

The etching rate of the processed wafer can be monitored by a full wafer interferometer (FWI) system with a CCD camera above the top of quartz dome.

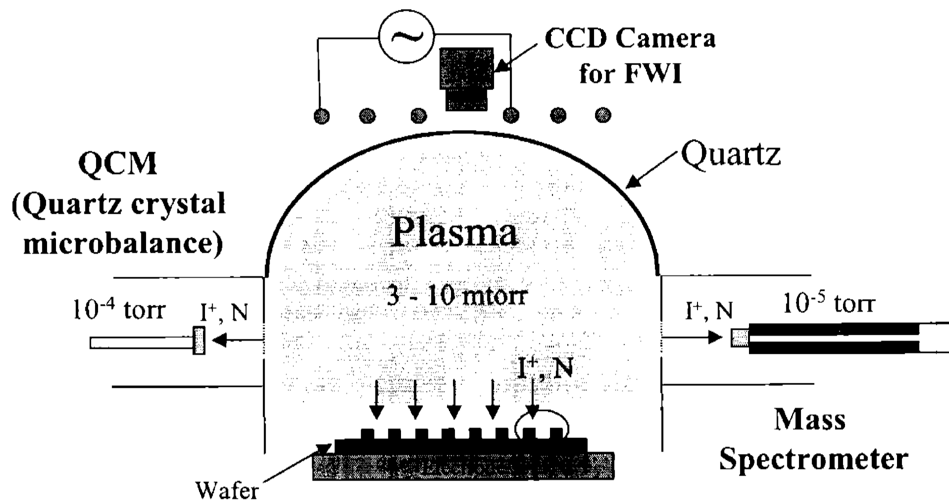

Figure 2.2 Schematic diagram of inductively-coupled plasma etcher.

2.1.2 Quartz crystal microbalance (QCM) and chamber

Figure 2.3 shows a schematic diagram of the quartz crystal microbalance (QCM) chamber. The QCM chamber is located at the side of etching chamber as shown in Figure 2.2. The side chamber is 4" in diameter and 10" long. This chamber is differentially pumped by a 210 l/s turbomolecular pump. A base pressure of 5 x 10^{-7} torr is maintained.

The QCM sample is coated with 10,000 Å of PECVD oxide to study oxide etching characteristics. The sample temperature is controlled by a cooling system of which coolant temperature can be varied from -30 °C to 80 °C. The QCM sample temperature is maintained to 20 °C, mentioned otherwise.

A double grid is installed between the main processing chamber and the QCM chamber for the extraction of ions and neutrals. This double grid design makes it possible to maintain a relatively uniform electric field across the extraction grid that enables to have a relatively directional ion beam. The distance between the grids is 0.22 inch. Ions will be accelerated

between ground mesh and orifice array. Electric field between ground mesh and orifice array is up to 900 V/cm. Ion current measured on the orifice array was between 0.5-1.5 mA depending on the plasma chemistry and process conditions.

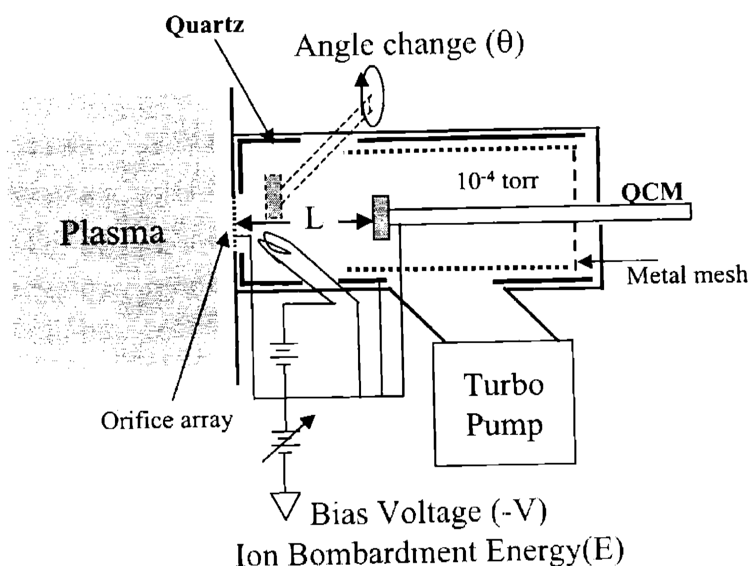

Figure 2.3 Schematic diagram of quartz crystal microbalance (QCM) chamber.

Inside the QCM chamber is insulated using a quartz liner and the potential of the entire QCM chamber is maintained uniform. The ion bombardment energy is varied by imposing a DC bias to the QCM sample -500 V.

To prevent a beam spreading and neutralize insulating surface including silicon oxide film on QCM sample, an electron emitting tungsten filament is used located between the extraction grid and the QCM sample. A 2.0 A of current is supplied to the filament, which provides sufficient thermionic electron emission.

Etching rate is measured by monitoring the change in the resonance frequency of QCM sample as the weight of the film changes with etching or deposition. Ion current is also measured by placing a metal plate and the etching yield (material removed per incident ion) is calculated.

The angle of the QCM sample is rotated to change ion impinging angle and angular dependent etching yield is investigated.

2.1.3 Mass Spectrometer and Chamber

A quadrupole mass spectrometer (QMS, UTI 100C) is used for ion and neutral composition analysis and is housed inside the mass spectrometer side chamber attached. It has a similar design to the QCM chamber.

A mass spectrometer consists of three major components of ionizer, mass filter, and detector. Gas molecules extracted from plasma by differential pumping are bombarded by high energy electrons emitted from the filament within the ionizer and are fragmented and ionized positively. Typically ionization energy of -25 V is applied, which is lower than a typical value, to minimize cracking of neutrals in the ionizer. The ionizer filament current is 2.0 mA. The ionizer is turned off when ion composition is measured.

A combined radio-frequency and electrostatic field is formed by two pairs of metal rods in the filter section. The ions created in the ionizer have a dynamically stable trajectory within the field formed by the voltages on the rods, and are dependent on their mass to charge ratio. Other ions are filtered out. By continuously varying the applied voltage, a range of mass-to-charge ratio can be sequentially stabilized, and these traverse the length of the filter assembly. The species traversing the filter are detected by an electron multiplier that amplifies the single charge of the ion into a current. The output current of the multiplier is referenced against the scan voltage, thereby producing a spectrum of peaks. The spectrum produced shows ion current as a function of the quotient mass-to-charge ratio in each peaks corresponding to a different ion mass. The amplitude is proportional to the quantity of each type of ion. Discrete peaks occur because the charged substances have discrete masses and discrete charges.

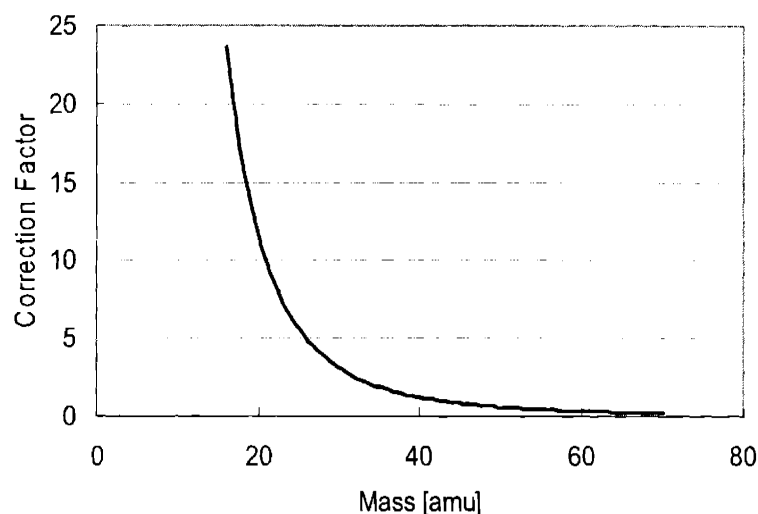

Figure 2.4 Sensitivity of mass spectroscopy measurement varying with molecular mass in amu.

To conduct a quantitative measurement with the mass spectrometer, the characteristics of the mass spectrometer must be determined carefully. To have an accurate measurement, the measured peak intensities are corrected for ionization efficiency (a combination of ionization cross-section and ionization potential), multiplier gain, and quadrupole transmission for each species. The combination of the multiplier gain and the quadrupole transmission for the mass spectroscopy analyzer is plotted in Figure 2.4[1]. The ionization efficiency is shown in Figure 2.5[1]. For neutral composition measurement, all of the three factors are considered, and for ion composition measurement only the multiplier gain and the quadrupole transmission are considered because ionizer is turned off when ion composition is measured.

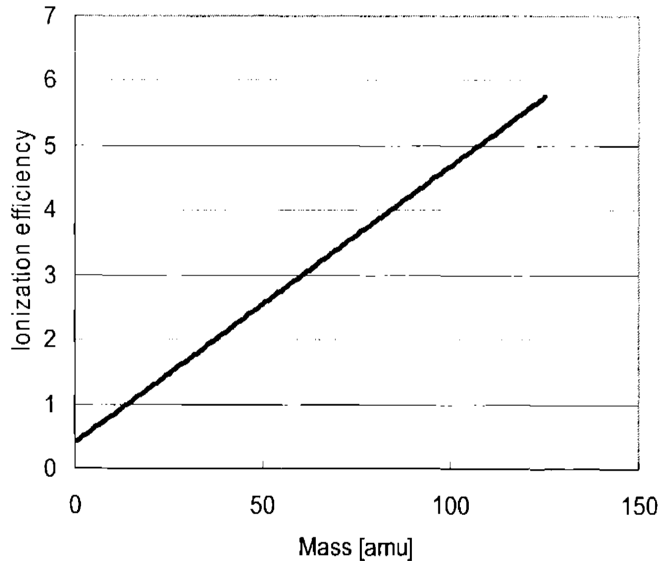

Figure 2.5 Ionization efficiency of the mass spectrometer.

2.2 Surface plot: oxide etching yield as a function of incoming flux

Butterbaugh *et al.*[2] suggested a surface plot representing oxide etching yield as a function of incoming fluxes, where F, CF_2 neutrals and Ar^+ ion beams are used to mimic a real oxide etching process. (Figure 2.6)

In this plot, there are three regimes. In the regime where F flux is low, the surface kinetics is dominated by CF_2 flux because the surface is covered with CF_2. In the regime where F flux is moderate, the surface is covered with both CF_2 and F. F is considered as the primary etchant and the etching yield is relatively independent of CF_2 flux, which is due to the CF_2 reduction by F flux. In the regime where F flux is high, the CF_2 reduction by F is very rapid and surface is primarily covered with F.

This picture, however, is a case when the effect of deposition is not significant. It has been reported by many researchers that when carbon fluxes (CF_x) increase, deposition

component becomes greater[3,4]. When the effect of deposition becomes important, the surface plot can be drawn as Figure 2.7, which is a modification of Figure 2.6 merely to add the etching yield depression with increased CF_x flux.

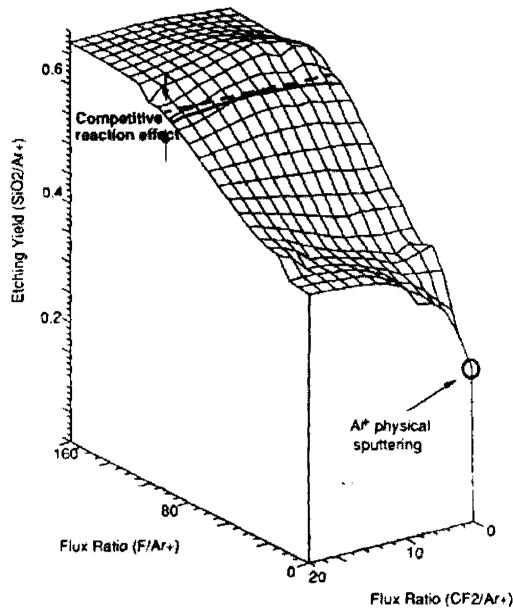

Figure 2.6 Oxide etching yield measured with three beams (CF_2, F and Ar^+)[2].

It is a modification of Butterbaugh's surface plot, where there is a reduction in etching yield as the CF_x flux increases due to the deposition on the surface. The next section discusses how the surface plot can be used to qualitatively describe the etching phenomena.

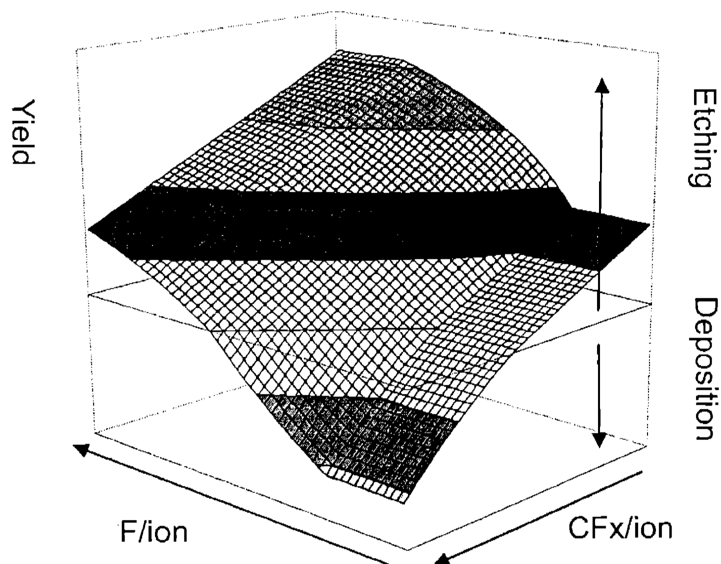

Figure 2.7 Modified surface plot with deposition chemistry.

2.3 Result and Discussion

The measurement of neutral and ion species and etching yield were conducted for two different chemistries: 100% C_2F_6 and C_4F_8 + 80% Ar. Plasma coil power was varied from 200 W to 500 W and pressure was varied from 5 mTorr to 50 mTorr. Mass spectrometry measurement and QCM measurement were carried with varying plasma conditions. Ion energy was set to 300 eV by biasing the QCM sample.

To explain the yield variation with varying plasma conditions, the surface plot in Figure 2.7 is used. Change in the gas composition is plotted to qualitatively show the variation in etching yield with varying plasma conditions.

2.3.1 C_2F_6 chemistry with varying RF coil power

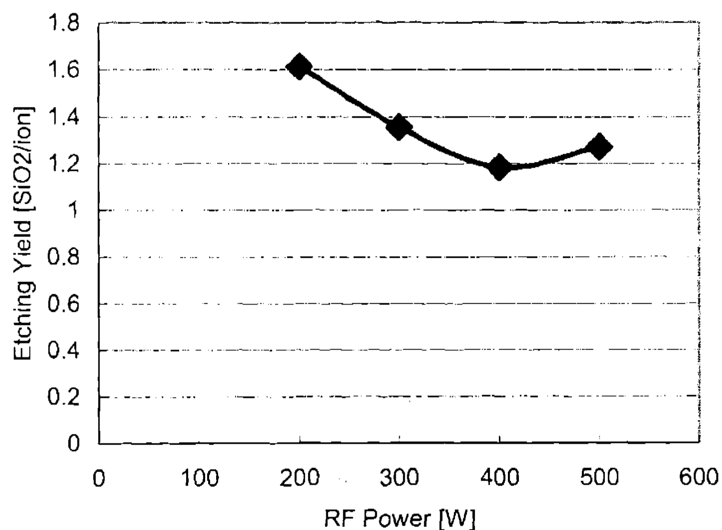

Figure 2.8 Etching yield as a function of RF coil power for C_2F_6 chemistry. 5 m Torr operating pressure, 300 eV DC bias.

Figure 2.8 is etching yield in C_2F_6 chemistry as a function of RF coil plasma power showing slight decrease in etching yield as RF coil power increases with a slight increase at 500 W coil power. To link the etching yield behavior to plasma chemistry, ion and neutral compositions in the C_2F_6 plasma were measured with varying RF coil power shown in Figure 2.9, Figure 2.10 and Figure 2.11.

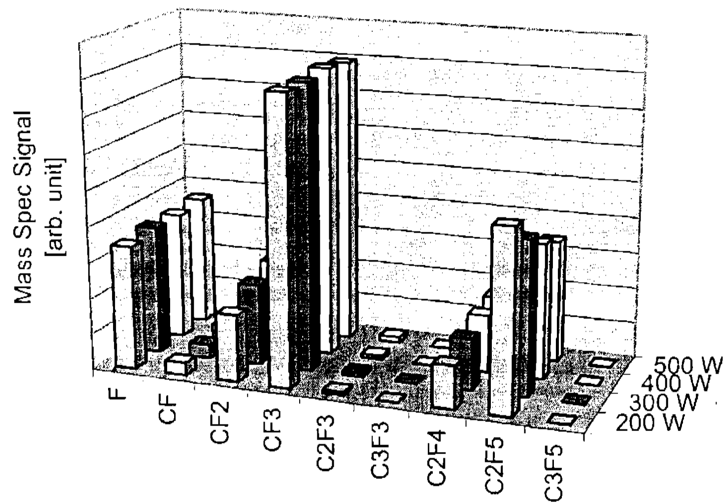

(a)

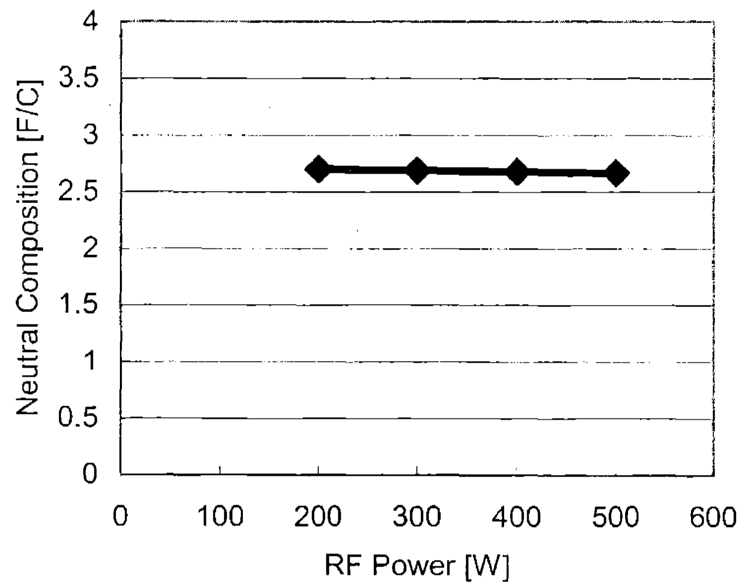

(b)

Figure 2.9 Neutral composition change in C_2F_6 plasma with varying RF coil power at 5 mTorr operating pressure. (a) Neutral compositions. (b) F/C ratio in the neutral flux.

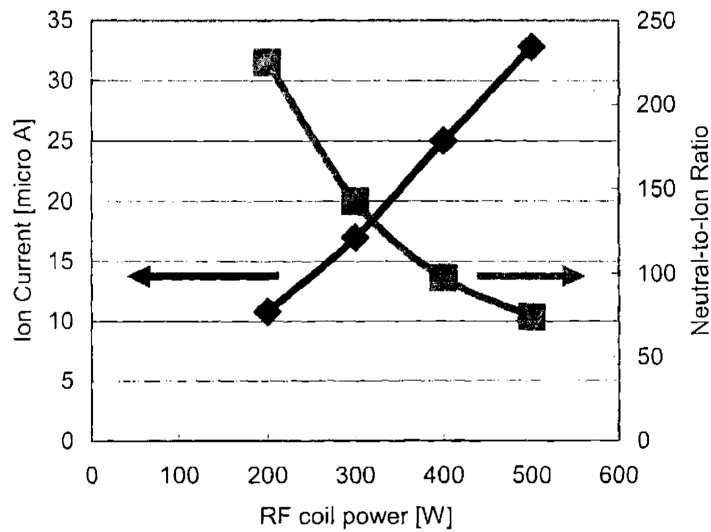

(a)

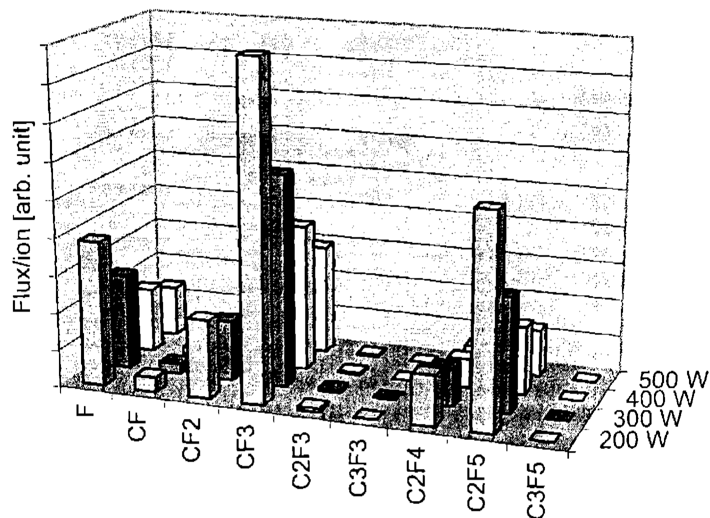

(b)

Figure 2.10 Ion current and ion-to-neutral flux ratio with varying RF coil power. C_2F_6 plasma, 5 mTorr operating pressure, 300 eV DC bias. (a) Total ion current and overall neutral-to-ion flux ratio. (b) Flux ratios for neutral gas species.

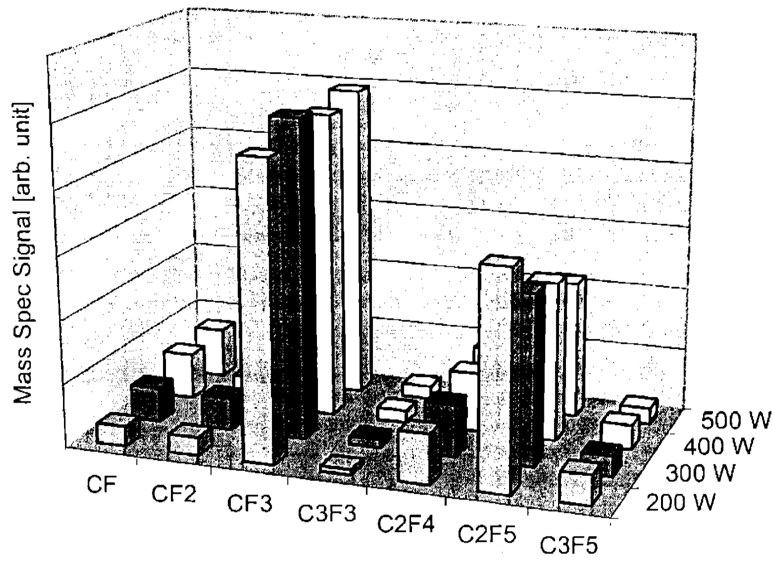

(a)

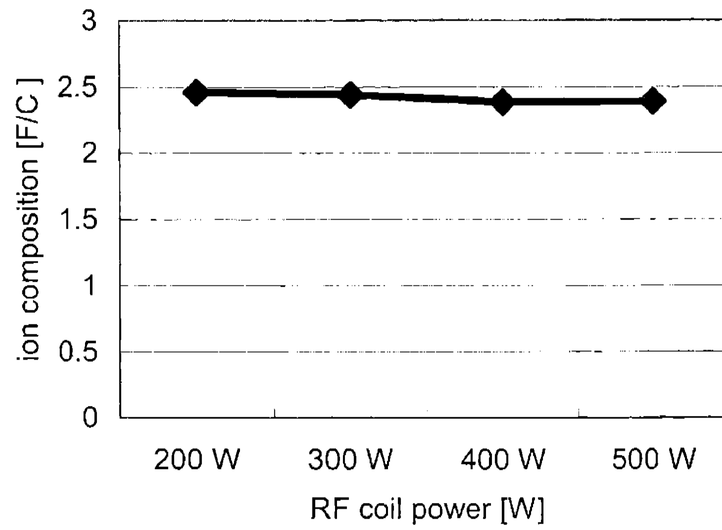

(b)

Figure 2.11 Change in ion composition with varying RF coil power. C_2F_6 plasma, 5 mTorr operating pressure. (a) Mass spectrometry signal. (b) F/C ratio in the ion flux.

Figure 2.9 shows the neutral composition change in C_2F_6 plasma with varying RF coil power. Figure 2.9(a) shows increase in CF_2 concentration and decrease C_2F_5 concentration. Figure 2.9(b) is a overall F/C ratio in the measured fluorocarbon neutrals showing that the value does not change with RF power, which is about 2.7. Looking at the neutral flux only with overall F/C ratio can be misleading because the role of fluorine in atomic fluorine flux is very different from the role of fluorine in fluorocarbon fluxes, which is discussed in detail in Chapter 4.

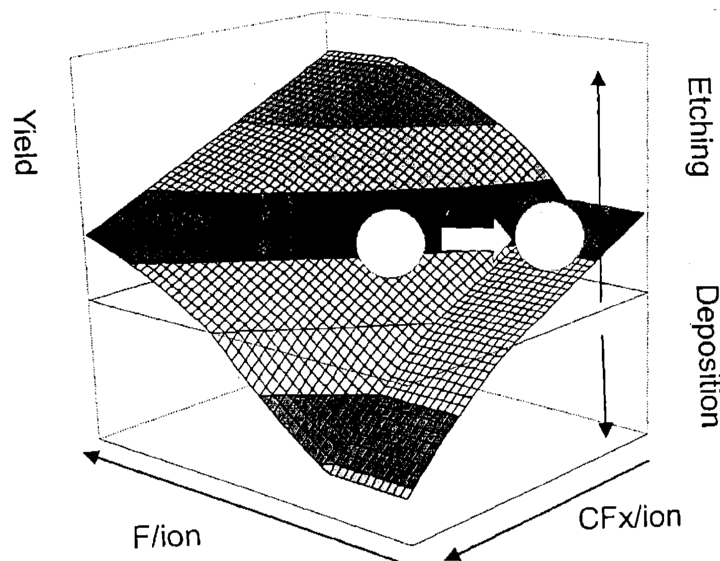

Figure 2.12 Qualitative representation of etching yield change with RF coil power in C_2F_6 chemistry.

When converted into flux ratios (F/ion or CF_x/ion), however, both F/ion and CF_x/ion decrease with increasing RF coil power as shown Figure 2.10. Figure 2.10(a) shows increase in the total ion current and decrease in the neutral-to-ion flux ratio with RF coil power. The flux ratios of individual neutral species are shown in Figure 2.10(b). Due to increase in ion current,

and hence the decrease in neutral-to-ion flux ratio, the entire F/ion and CF_x/ion decrease with increasing RF coil power. Increase in ion current is due to the increase in plasma density caused by higher RF power supplied.

Ion composition change with RF power is shown in Figure 2.11. Because ions are assumed to have 100% sticking probability to be 'implanted' into the surface layer, only overall composition of ions may be considered instead of flux of individual ion species. Ion composition dose not change significantly with varying RF coil power and has no significant effect on etching yield.

To plot the change in the incoming flux, Figure 2.12 qualitatively shows a slight decrease in etching yield, which agrees with the measured data in Figure 2.8. As RF coil power increases, both F/ion and CF_x/ion decrease and they are compensated by each other, with a slightly more effect of decrease in F/ion than CF_x/ion. Hence, the etching yield decreases slightly with increased RF coil power in C_2F_6 chemistry. The slight increase in etching yield at RF coil power of 500 W is due to the change in the region as shown in Figure 2.12. At 500 W of RF coil power, the low neutral-to-ion flux ratio causes low atomic fluorine flux and the effect of atomic fluorine becomes less significant, which is discussed in Chapter 4 with more detail.

2.3.2 C_2F_6 chemistry with varying operating pressure

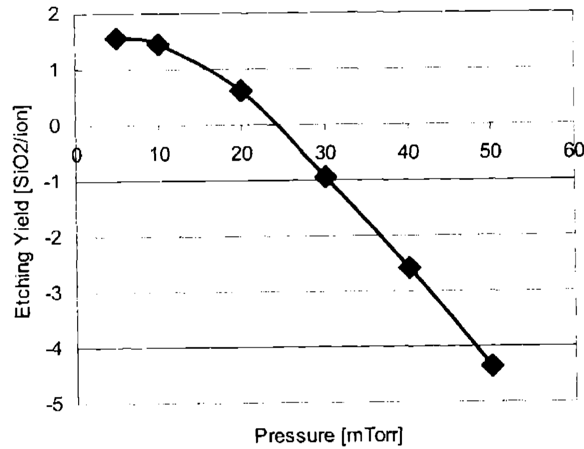

Figure 2.13 Etching yield as a function of operating pressure for C_2F_6 chemistry. 300W RF coil power, 300 eV ion energy.

Etching yield with varying operating pressure for C2F6 chemistry is shown in Figure 2.13. The etching yield decreases as the operating pressure increases and eventually goes to net deposition regime above about 25 mTorr. Depending on the experimental conditions, oxide etching in fluorocarbon chemistry often shows transition between etching and deposition[5-7].

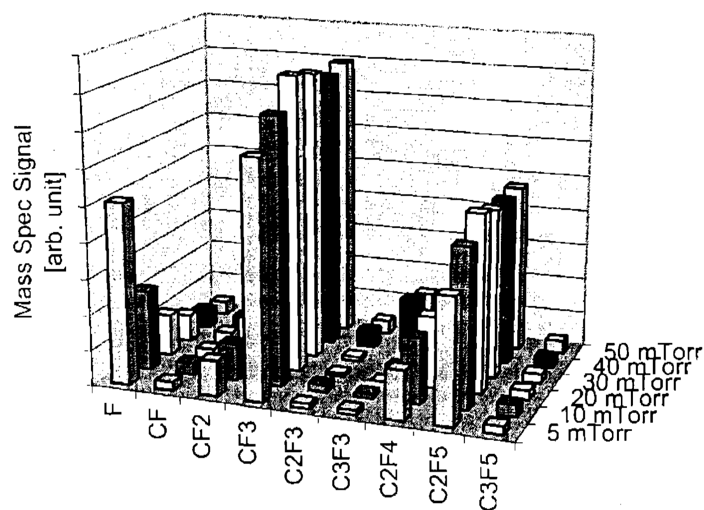

(a)

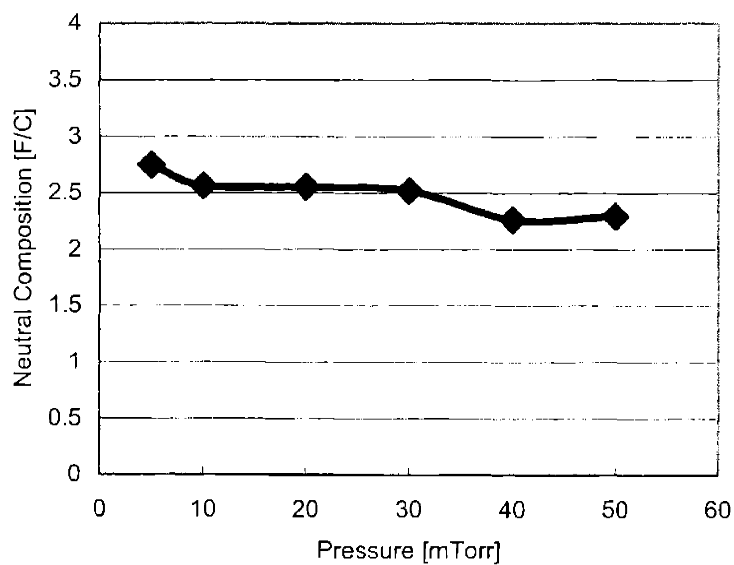

(b)

Figure 2.14 Neutral composition change in C_2F_6 plasma with varying operating pressure 300 W RF coil power. (a) Neutral compositions. (b) F/C ratio in the neutral flux.

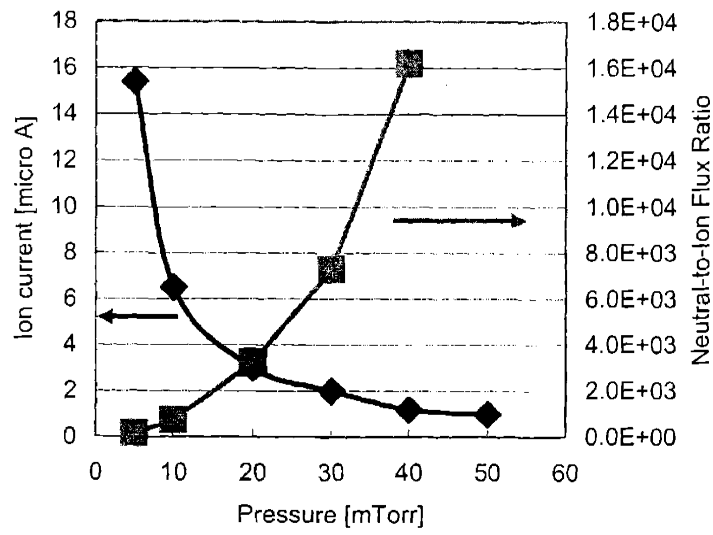

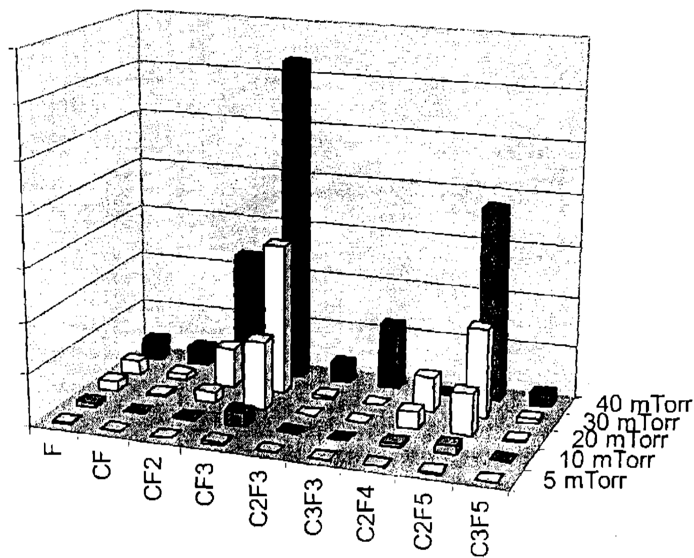

Figure 2.15 Ion current and neutral-to-ion flux ratio with varying operating pressure. C_2F_6 plasma, 300 W RF coil power, 300 eV DC bias. (a) Total ion current and overall neutral-to-ion flux ratio. (b) Flux ratios for neutral gas species.

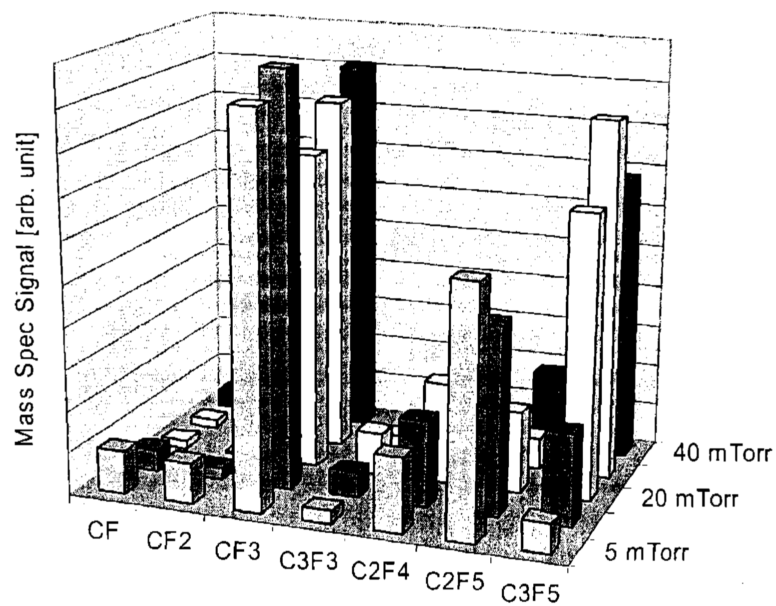

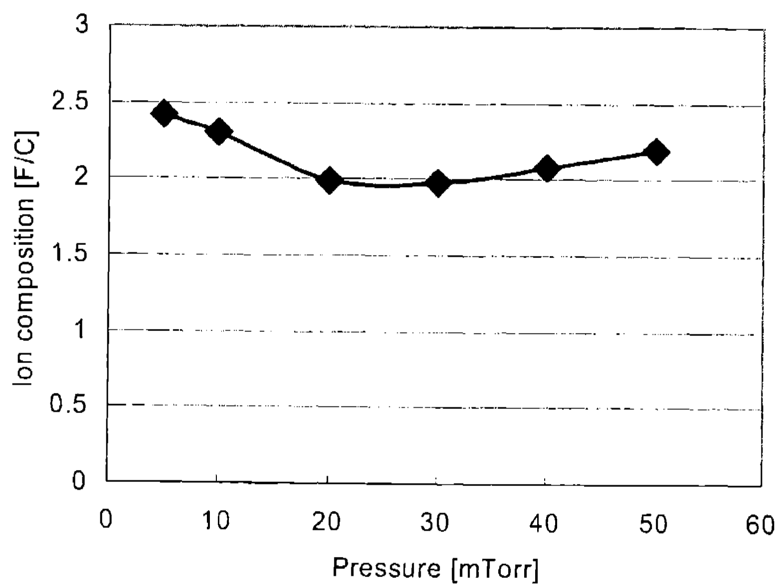

Figure 2.16 Change in ion composition with varying operating pressure. C_2F_6 plasma, 300 W RF coil power. (a) Mass spectrometry signal. (b) F/C ratio in the ion flux.

To explain the yield change with pressure variation, plasma gas compositions were measured. Figure 2.14 shows the neutral composition change in C_2F_6 plasma with varying operating pressure measured with mass spectroscopy. Figure 2.14(a) is the neutral composition of the plasma, and Figure 2.14(b) is F/C ratio in the neutral flux. As the operating pressure increases, atomic fluorine concentration decreases and CF_x increase. This could be because atomic fluorine is consumed by a surface recombination reaction[2] to produce CF_4 and the gas species are less fragmented at higher pressure. The slight decrease in F/C ratio in the neutral flux can be also because of the CF_4 surface production: Surface-produced CF4, which is F/C ratio of 4 is pumped to reduce overall F/C ratio in the neutral flux.

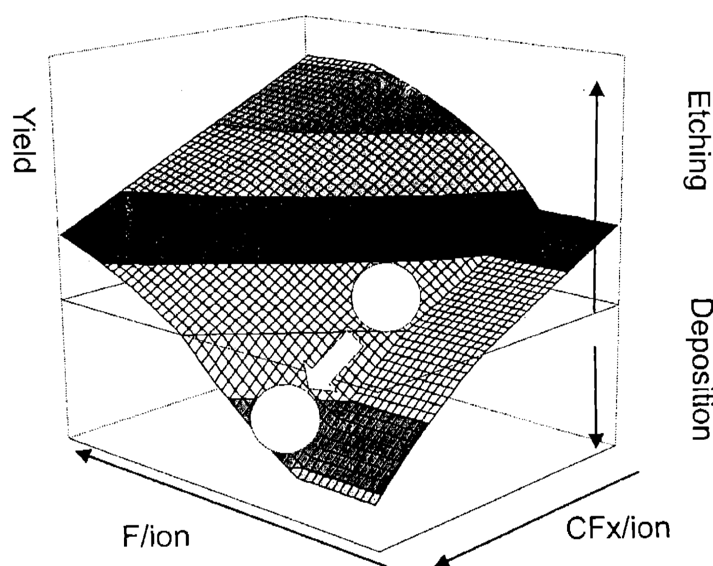

Figure 2.17 Qualitative representation of etching yield change with operating pressure in C_2F_6 chemistry.

When converted into neutral-to-ion flux ratio values, however, the entire changes in the neutral composition are dominated by the dramatic decrease in the ion current as shown in

Figure 2.15. The decrease in the ion current is because ionization process becomes less efficient as pressure increases. As pressure increases, mean free path of electrons becomes shorter and the electron energy declines increasing the relative rate of lower energy processes to ionization.

Ion composition change with operating pressure is shown in Figure 2.16. The overall the ion composition does not change significantly and the effect of the ion composition change should be negligible.

The compositional change in the incoming flux is plotted in the surface plot in Figure 2.17, which qualitatively shows the trend of measured data in Figure 2.13. Since both F/ion and CF_x/ion decrease dramatically (with more significant decrease in CF_x/ion), etching yield should follow the arrow in the surface plot to decrease in value and eventually make transition from net etching regime to net deposition regime. The decrease in the etching yield with decreased ion flux is because etching process is primarily ion-induced etching process while polymerization reduces as ion flux increases[8]. Decrease in ion flux diminishes etching component, while increase in neutral flux enhances deposition process.

2.3.3 C_4F_8 + 80% Ar chemistry with varying RF coil power

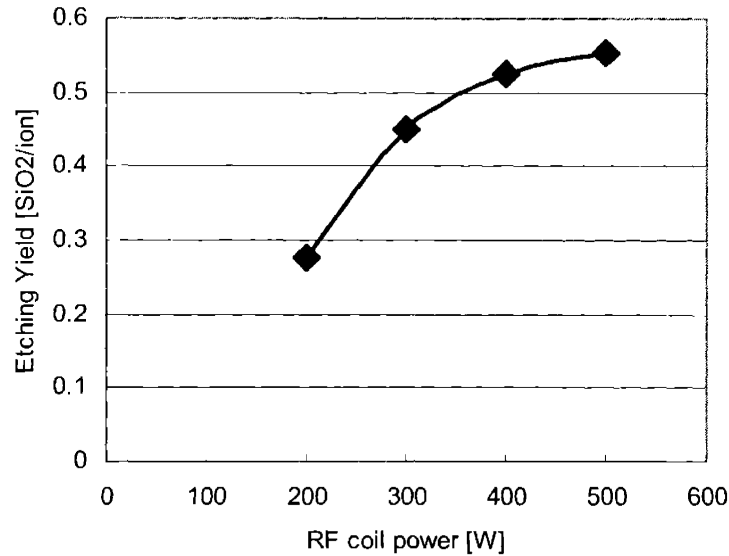

Figure 2.18 Etching yield as a function of RF coil power for C_4F_8 + 80% Ar chemistry.

A similar analysis was done for C_4F_8 + 80% Ar chemistry. Figure 2.18 is etching yield in C_4F_8 + 80% Ar chemistry as a function of RF coil plasma power showing increase in etching yield as RF coil power increases.

Neutral composition is shown in Figure 2.19. Figure 2.19(a) shows the neutral composition change with varying RF coil power in C_4F_8 + 80% Ar chemistry and Figure 2.19(b) is overall F/C ratio in the measured neutral flux. The neutral composition does not change significantly with power change.

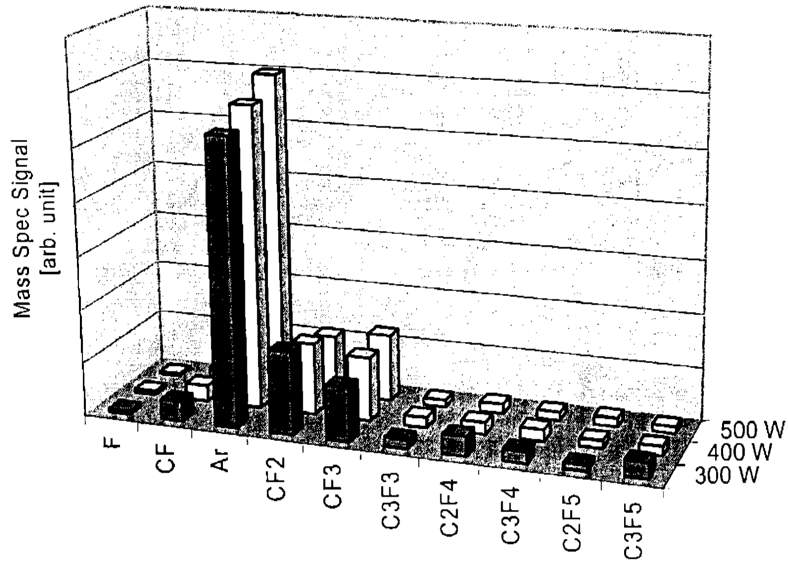

(a)

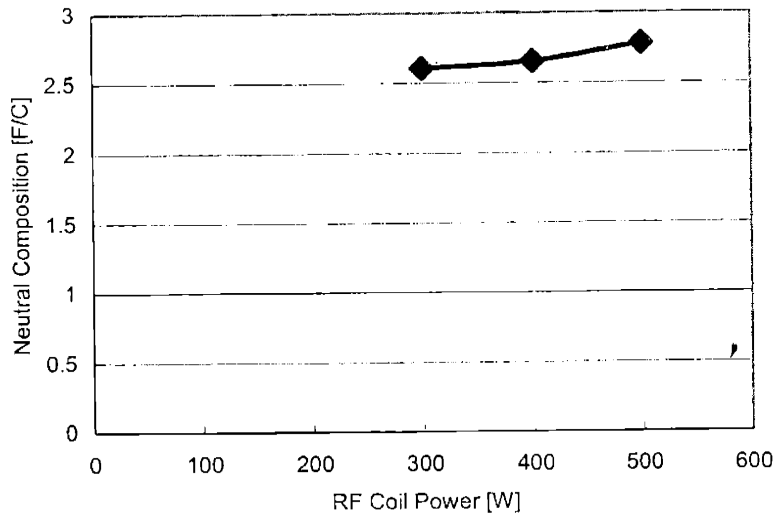

(b)

Figure 2.19 Neutral composition change in C_4F_8 + 80% Ar plasma with RF coil power at 5 mTorr of pressure. (a) Neutral compositions. (b) F/C ratio in the neutral flux.

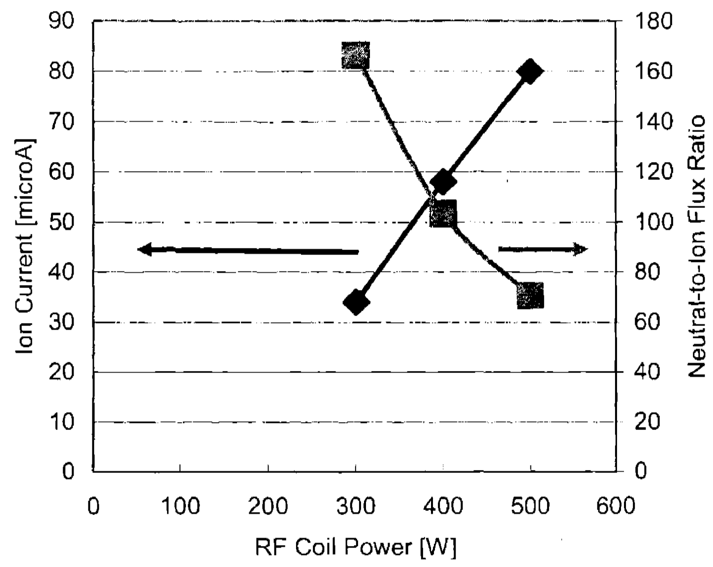

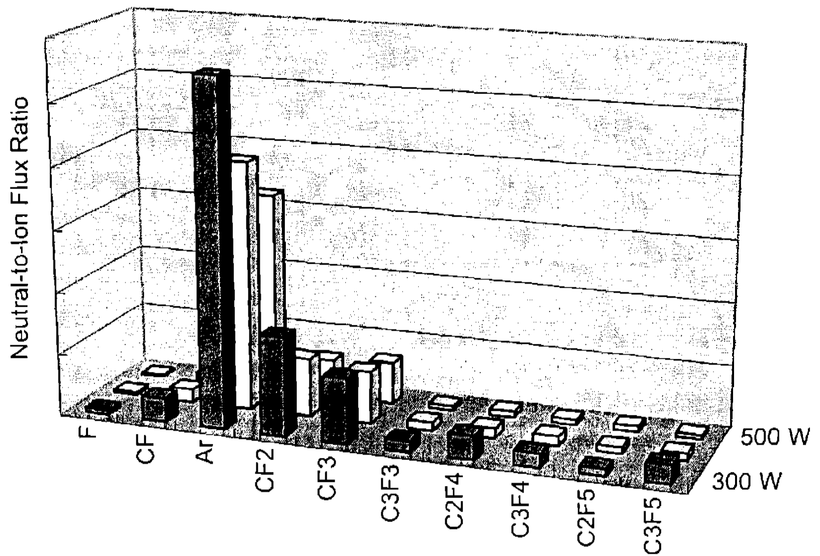

Figure 2.20 Ion current and neutral-to-ion ratio with varying RF coil power. C_4F_8 + 80% plasma, 5 mTorr operating pressure, 300 eV DC bias. (a) Total ion current and overall neutral-to-ion flux ratio. (b) Flux ratios for neutral gas species.

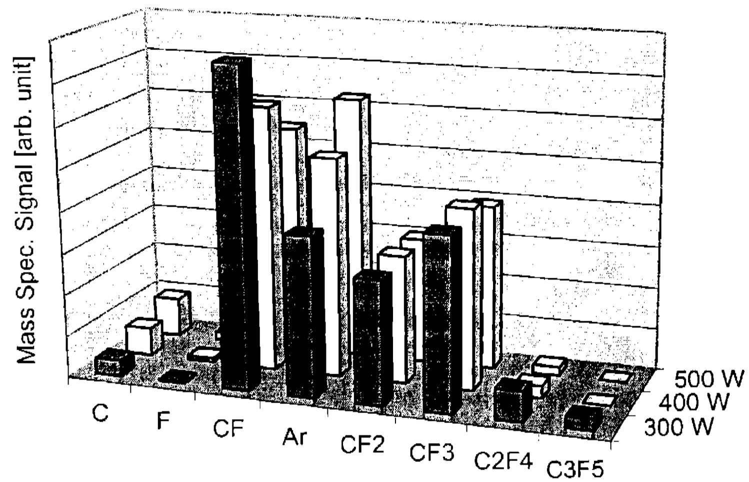

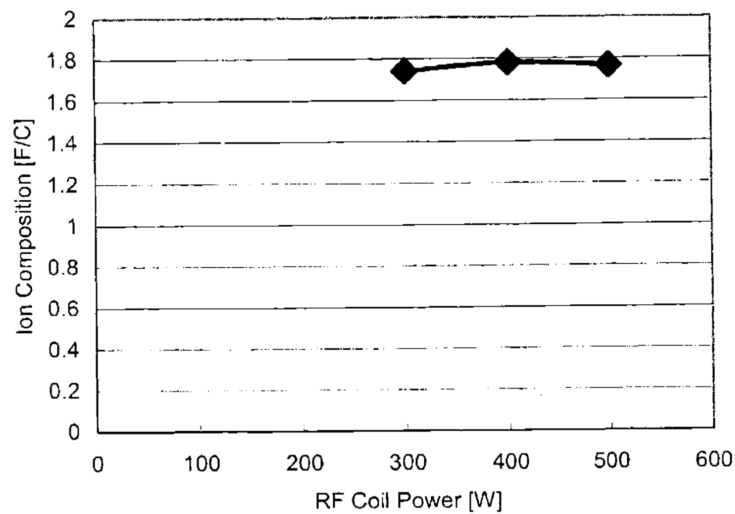

Figure 2.21 Change in ion composition with varying RF coil power. C_4F_8 + 80% Ar plasma, 5 mTorr operating pressure. (a) Mass spectrometry signal. (b) F/C ratio in the ion flux.

When they are converted into neutral-to-ion flux ratios, the entire flux ratio values show significant decrease in all the neutral flux ratios with increasing RF coil power as shown in Figure 2.20. This is because of the dramatic increase in the ion current with increasing RF coil power (Figure 2.20(a)), which is also observed in C_2F_6 chemistry (Figure 2.10) indicating plasma density is increased by increasing RF coil power.

The most significant characteristic of C_4F_8 + 80% Ar chemistry that differentiates it from C_2F_6 chemistry is very low concentration of atomic fluorine. In C_4F_8 + 80% Ar chemistry atomic fluorine percentage in the neutral flux is less than 0.5%, while in C_2F_6 chemistry it is 5~25%.

The ion composition does not show any significant change with varying RF coil power (Figure 2.21) and the effect of ion composition is assumed to be negligible.

The change in the composition of the incoming flux is plotted in the surface plot shown in Figure 2.22, which shows the qualitative trend of the measured data in Figure 2.18. Since there is not significant amount of atomic fluorine flux, the compositional change follows the arrow shown in Figure 2.22, which represents the decrease in CF_x/ion flux at very low F/ion region.

The increase in etching yield with increasing RF coil power is a result of the decrease in CF_x/ion flux ratio in C_4F_8 + 80% Ar chemistry.

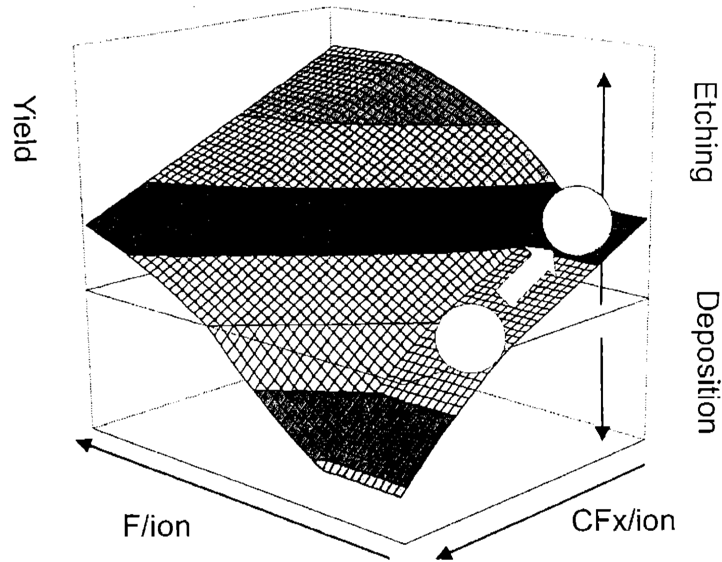

Figure 2.22 Qualitative representation of etching yield change with RF coil power in C_4F_8 + 80% Ar chemistry.

2.3.4 C_4F_8 + 80% Ar chemistry with varying operating pressure

Figure 2.23 is etching yield in C_4F_8 + 80% Ar chemistry as a function of operating pressure showing a dramatic decrease in etching yield as pressure increases. Similar to C_2F_6 chemistry, C_4F_8 + 80% Ar chemistry also shows an etching-to-deposition transition in etching yield measurement. The crossover is at ~12 mTorr.

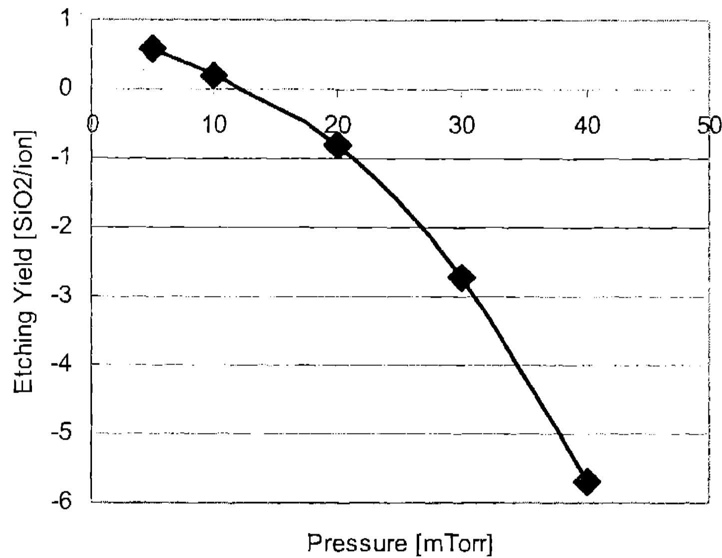

Figure 2.23 Etching yield as a function of operating pressure for C_4F_8 + 80% Ar chemistry. 300 W RF coil power, 300 eV ion energy.

Figure 2.24 shows the neutral composition in the plasma measured by mass spectroscopy. Similar to C_2F_6 chemistry, neutral composition shows no significant variation with operating pressure change (Figure 2.24). After converted to neutral-to-ion flux ratios, however, the entire neutral flux ratios increase dramatically (Figure 2.25 (b)) because of the dramatic drop in ion current (Figure 2.25(a)). The decreased ion current is due to the inefficiency of ionization process at higher pressure, as explained in C_2F_6 section.

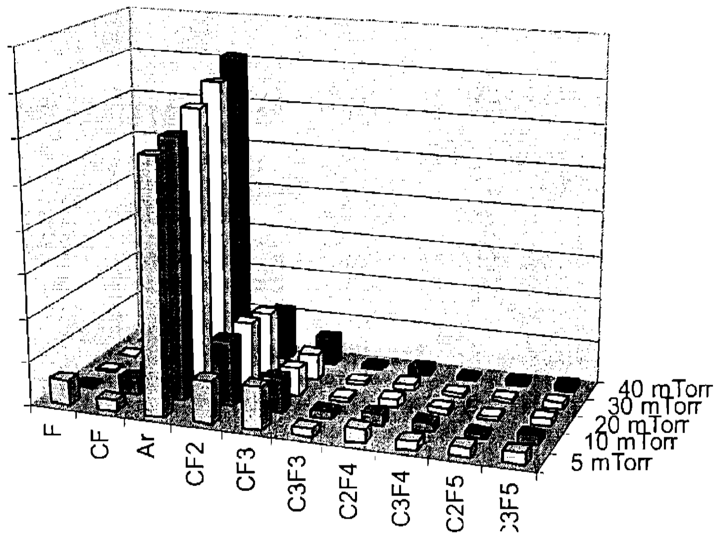

(a)

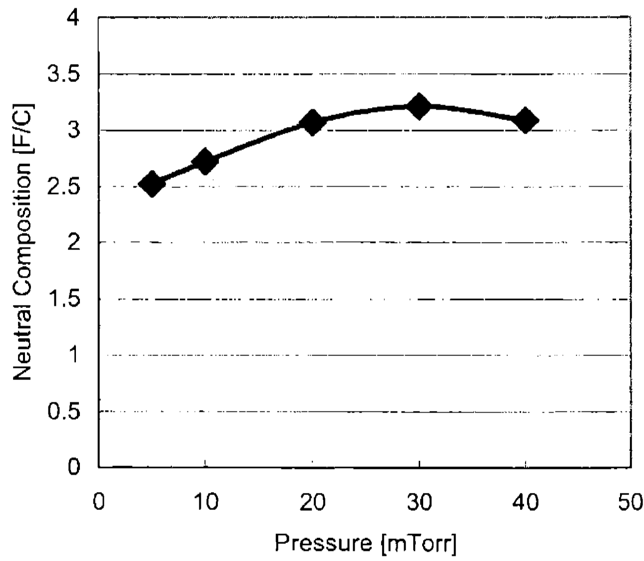

(b)

Figure 2.24 Neutral composition change in C_4F_8 + 80% Ar plasma with varying operating pressure 300 W RF coil power. (a) Neutral compositions. (b) Neutral-to-ion flux ratios.

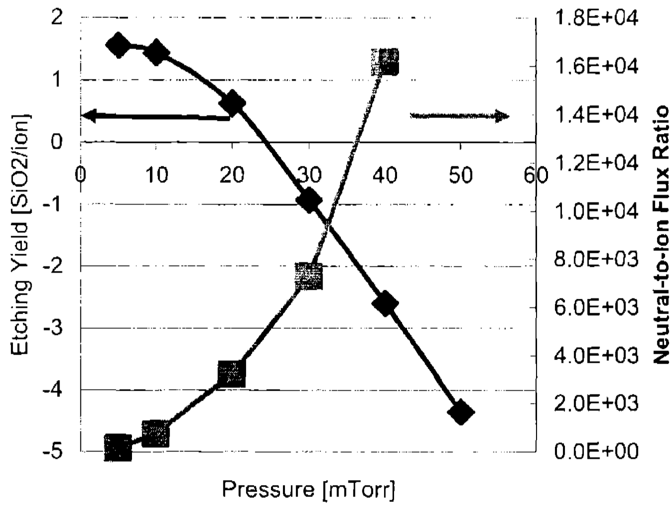

(a)

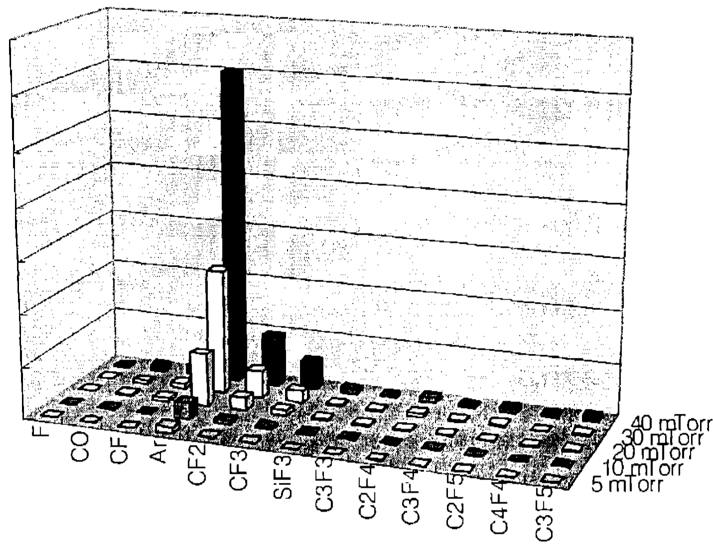

(b)

Figure 2.25 Ion current and neutral-to-ion flux ratio with varying operating pressure. C_4F_8 + 80% Ar plasma, 300 W RF coil power, 300 eV DC bias. (a) Total ion current and overall neutral-to-ion flux ratio. (b) Flux ratios for neutral gas species.

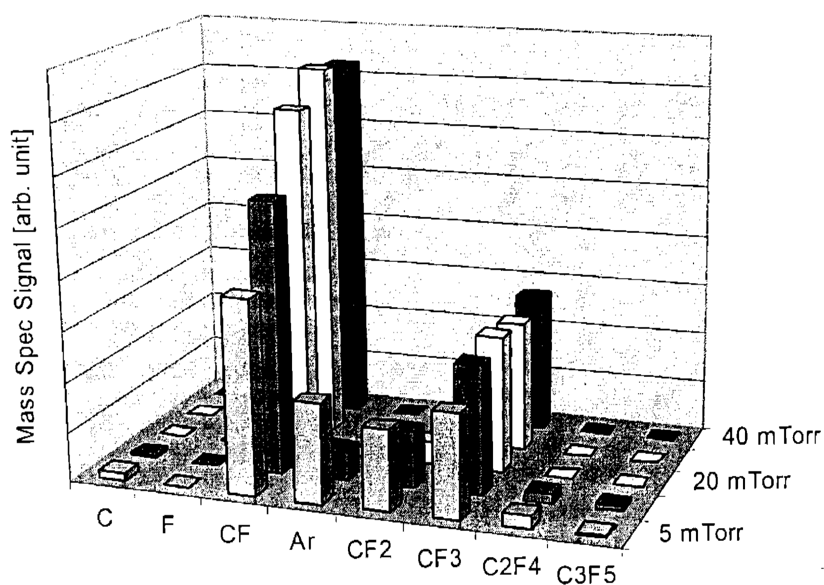

(a)

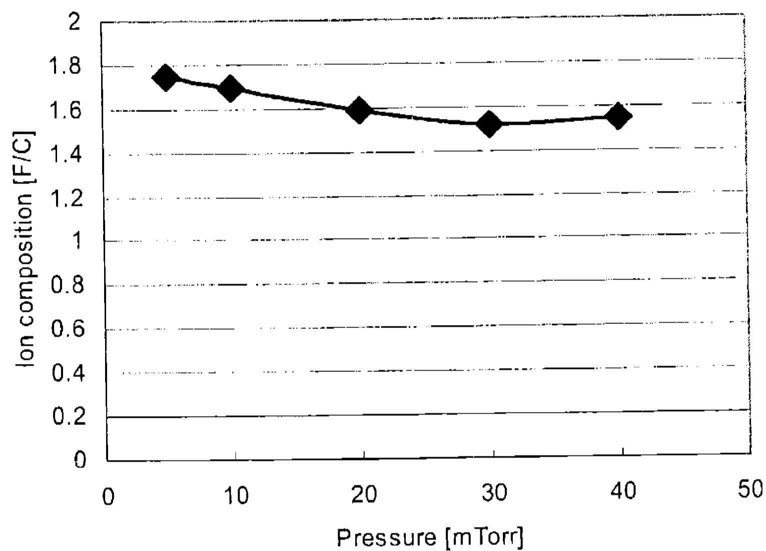

(b)

Figure 2.26 Change in ion composition with varying operating pressure. C_4F_8 + 80% Ar plasma, 300 W RF coil power. (a) Mass spectrometry signal. (b) F/C ratio in the ion flux.

The effect of ion composition change is negligible because ion composition does not change significantly with pressure (Figure 2.26).

The compositional change in the incoming flux is plotted in the surface plot in Figure 2.27, which qualitatively shows the trend of measured data in Figure 2.23. Since CF_x/ion increased dramatically (with no effect of F/ion because atomic fluorine concentration is negligible), etching yield should follow the arrow in the surface plot to decrease in value and eventually make transition from net etching regime to net deposition regime. As explained in the C_2F_6 section, the decrease in the etching yield with decreased ion flux is because of slower etching process and higher polymerization at lower ion flux.

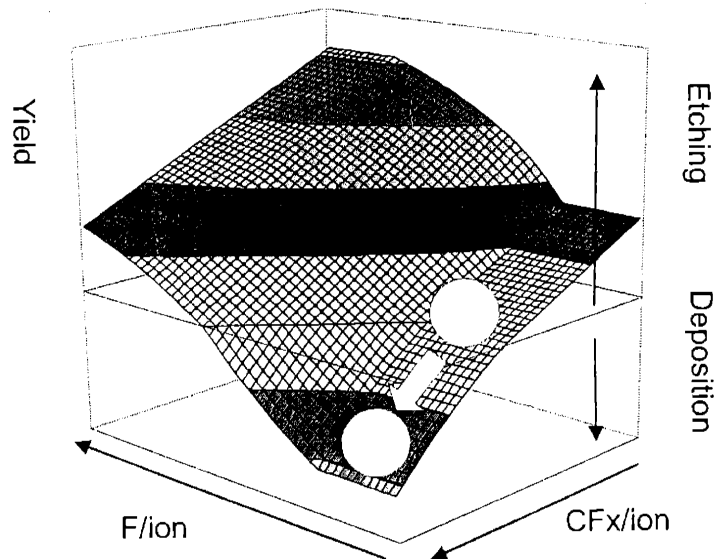

Figure 2.27 Qualitative representation of etching yield change with operating pressure in C_4F_8 + 80% Ar chemistry.

2.4 Conclusion

Etching yield and gas composition for C_2F_6 and C_4F_8 + 80% Ar varying RF coil power and pressure were measured. In C_2F_6 plasma, concentration of atomic fluorine in the neutral flux was 5~25% while there was less than 0.5% of atomic fluorine in C_4F_8 + 80% Ar plasma. A surface plot representing etching yield as a function of incoming fluxes has been constructed and using the surface plot etching yield behaviors were qualitatively explained using the surface plot.

In C_2F_6 chemistry, etching yield decreases slightly with increasing RF coil power. This is because of the decrease in both F/ion and CFx/ion which is caused by increase in ion flux with more significant effect of decrease in F/ion. In C_4F_8 + 80% Ar chemistry, however, etching yield increases with increasing RF coil power. This is attributed to the decrease in CF_x without the effect of F/ion because of low atomic fluorine concentration.

With increase operating pressure, etching yield decreases for both chemistries because as the pressure increases ion current decreases and CF_x neutral concentration increases to have more deposition and less etching.

Using the suggested surface plot, which is etching yield vs. incoming fluxes (F/ion and CFx/ion), etching yield change with changing RF coil power and operating pressure for C_2F_6 and C_4F_8 + 80% Ar chemistries were explained qualitatively.

2.5 References

1. S. A. Vitale, Ph.D. thesis, MIT, 2001.

2. J. W. Butterbaugh, D. C. Gray, and H. H. Sawin, J. Vac. Sci. Technol. B **9** (3), 1461 (1991).

[3] T. Tatsumi, M. Matsui, M. Okigawa et al., J. Vac. Sci. Technol. B **18** (4), 1897 (2000).

[4] K. Teii, M. Hori, T. Goto et al., J. Appl. Phys. **87** (10), 7185 (2000).

[5] M. Schaepkens, G. S. Oehrlein, C. Hedlund et al., J. Vac. Sci. Technol. A **16** (6), 3281 (1998).

[6] M. Schaepkens, T.E.F.M. Standaert, N.R. Rueger et al., J. Vac. Sci. Technol. A **17** (1), 26 (1999).

[7] H. Chae, S. A. Vitale, and H. H. Sawin, J Vac Sci Technol A **21** (2), 381 (2003).

[8] A. J. Bariya, C. W. Frank, and J. P. Mcvittie, J. Electrochem. Soc **137** (8), 2575 (1990).

Chapter 3. Translating Mixed-Layer (TML) Model

Plasma etching processes are very complicated. There are many process variables that can be changed to control etching characteristics and feature profile. There are three types of variables involved in plasma etching processes: process variables, plasma variables and etching characteristics.

Process variables are the ones that are directly controlled by the operator and they are plasma RF power, substrate bias, processing pressure, feed gas chemistry, etc. The process variables are the inputs of the process, which control the characteristics of the plasma. Plasma variables are the ones that are controlled by process variables and that control etching characteristics such as etching yield and etching feature profile. They include neutral composition, ion composition, ion-to-neutral flux ratio, ion bombardment etc. The relationship between process variables and plasma variables are described by means of plasma physics and relationship between plasma variables and etching characteristics are characterized by surface kinetics.

Traditionally the active-site model approach has been used to explain surface kinetics in plasma etching process[1-3]. In the active-site modeling approach, energetic ion bombardment creates active sites on the surface, which provide adsorption sites for chemically active species. Ion-induced chemical reactions occur to remove the material from the surface.

Figure 3.1 graphically illustrates an active-site model, an example of silicon etching with chlorine chemistry. The detailed description about the model is reported by many researchers[1,3,4]. The active-site model approach, however, cannot handle simultaneous etching and deposition when the depositing material is different from the material being etched, which often occur in

many plasma etching processes. Moreover, in case of multiple etching species, active-site model becomes very complicated and hard to solve.

In this research a novel modeling approach is studied to describe surface kinetics of etching characteristics as functions of plasma variables.

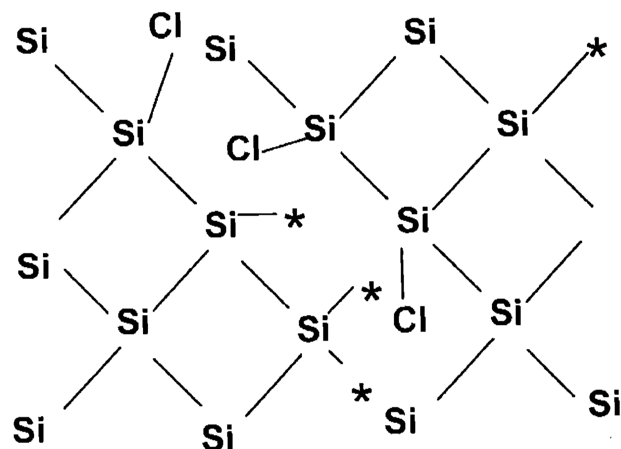

Figure 3.1 A graphical illustration of an active-site model for silicon etching with chlorine chemistry.

3.1 Translating Mixed-Layer (TML) Model

During plasma etching processes, surface reactions do not occur at the very top layer of the surface: There is a finite volume where all the reactions occur including adsorption, desorption, etching surface reaction. The thickness of the reaction volume can be as much as about 10 monolayers or 30-40 Å, depending on experimental conditions[5,6].

Based on the idea of well-mixed layer, a translating mixed-layer surface kinetic model is developed. The assumptions made for the model are:

1. Within the translating mixed-layer, the composition is homogeneous; i.e., well mixed by ion bombardment so that there is no concentration gradient.
2. The total number of atoms in the translating mixed-layer is conserved. The difference between the adsorption flux (flux from the gas phase to the surface) and the removal flux (flux from the surface to the gas phase) equals the movement flux (the flux from the substrate volume to the surface translating mixed-layer). The sign of the movement flux can be either positive or negative depending on the relative magnitude of adsorption and removal flux. When the adsorption flux is greater than the removal flux, the direction of the movement flux is from the translating mixed-layer to the substrate, representing net deposition. When the adsorption flux is smaller than the removal flux, direction of the movement flux is from the substrate volume to the translating mixed-layer, representing net etching.
3. All the reactions, which include ion bombardment, adsorption reaction, ion enhanced chemical etching surface reaction, physical sputtering, and deposition, occur in the translating mixed-layer volume.

Figure 3.2 shows a graphical illustration of a translating mixed-layer model. Although the etching yield could be modeled as a function of the incoming fluxes to the surface only, such a representation has difficulties in dealing with variations in the composition of the material being etched, which often occur as a result of deposition on the surface.

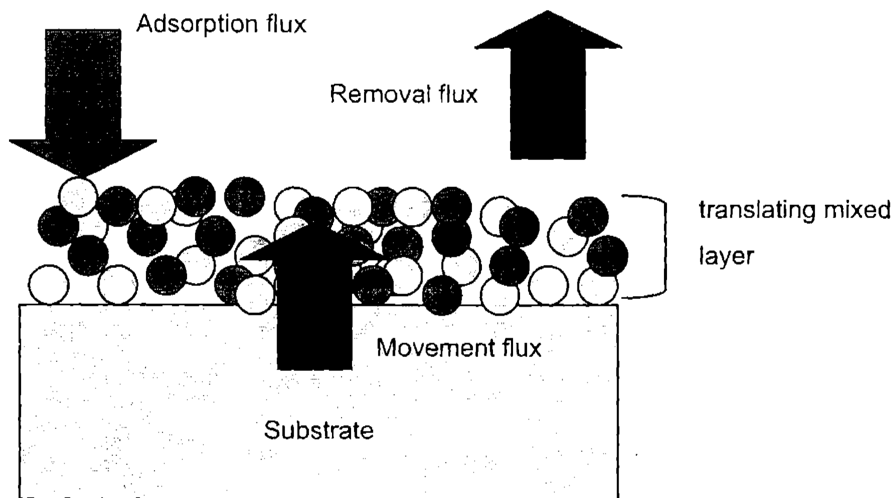

Figure 3.2 A graphical illustration of a translating mixed-layer model.

Once the translating mixed-layer modeling scheme is established, the steady-state composition of the layer, and hence, the etching yield can be calculated as a function of incoming fluxes.

In the next section, silicon etching with chlorine chemistry is modeled using the translating mixed-layer model.

Table 3.1 List of symbols used in equations.

symbol	comment
s	sticking coefficient
R_i	flux of species *i* divided by total ion flux
β	reaction coefficient of ion-induced etching
Y_i	sputtering yield coefficient of species *i*
x_i	concentration of species *i* in the well-mixed moving film
r_i	reaction rate in yield unit (reaction rate divided by total ion flux)

3.2 Silicon etching with chlorine chemistry

The list of symbols used in the equations used for describing the model is listed Table 3.1

The reaction rates are expressed in yield unit. The actual reaction rates are divided by total ion flux converting etching rates to etching yield.

For example, a typical ion-induced chemical etching process is

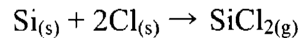

$$Si_{(s)} + 2Cl_{(s)} \rightarrow SiCl_{2(g)}$$

The corresponding etching rate is

$$R_3 = \beta \cdot x_{Cl} \cdot I^+$$

where I^+ is the total ion flux.

Dividing both sides by I^+, the equations becomes

$$r_3 = \beta \cdot x_{Cl}$$

making reaction rates expressed in etching yield unit instead of etching rate unit

Since most of the surface reactions are ion-induced, it is convenient to express rate expressions in etching yield unit instead of etching rate unit.

1. Adsorption

Chlorine neutrals striking the surface sticks with a sticking probability (s_1).

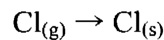

$$Cl_{(g)} \rightarrow Cl_{(s)}$$

with reaction rate

$$r_1 = s_1 \cdot R_{Cl} \cdot (x_{Si} - \frac{1}{2} x_{Cl})$$

The adsorption reaction rate is a product of sticking probability s_1, flux of Cl and effective Si concentration for Cl adsorption.

When calculating the effective concentration for adsorption, number of available sites is considered. The effective Si concentration for Cl adsorption is

$$x_{Si} - \frac{1}{2} x_{Cl}$$

because we assume that there are two possible active sites per silicon and the maximum number of chlorines per silicon is two.

It is addressed, however, that chlorine ions stick to the surface with a rate which is independent of surface composition because ions with high energy are considered to be implanted in the surface mixed layer. The reaction is written

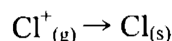

$$Cl^{+}_{(g)} \rightarrow Cl_{(s)}$$

with reaction rate expression

$$r_2 = s_2 \cdot R_{Cl^+}$$

The sticking coefficient for this reaction, s_2, is set to unity.

Inert ions, such as Ar^+ are assumed to provide only ion bombardment without any chemical effect.

2. Surface reactions

Ion-enhanced chemical etching reaction is

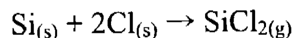

$$Si_{(s)} + 2Cl_{(s)} \rightarrow SiCl_{2(g)}$$

with reaction rate

$$r_3 = \beta \cdot x_{Cl}$$

The rate of production of $SiCl_2$ is proportional to chlorine concentration in the well-mixed moving film.

Physical sputtering reactions are

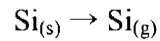

with reaction rate

$$r_4 = Y_{Si} \cdot x_{Si}$$

and

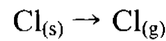

with reaction rate

$$r_5 = Y_{Cl} \cdot x_{Cl}$$

Ion-induced reaction coefficients, which include ion-induced etching coefficient (β) and sputtering yield coefficient (Y_i) have ion energy dependence, therefore, theses values will vary with the ion bombardment energy modeled.

3. Movement flux or convection flux

The difference between incoming flux and removal flux is compensated by setting up a compensation flux. Knowing that there is net etching with silicon etching with chlorine chemistry,

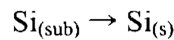

with reaction rate

$$\begin{aligned} r_6 &= (adsorption) - (etching) \\ &= -r_1 - r_2 + 3r_3 + r_4 + r_5 \end{aligned}$$

and the movement flux is essentially the etching yield because it is the net flux removed.

4. Calculating the etching yield and the surface composition

Time derivatives of species in the surface translating mixed-layer volume based on the elemental mass balance are

$$\frac{dx_{Si}}{dt} = -r_3 - r_4 + r_6$$

$$\frac{dx_{Cl}}{dt} = r_1 + r_2 - 2r_3 - r_5$$

Integrating the equations until they reach a steady state with initial condition of pure silicon (x_{si}=1) gives the steady state concentration in the translating mixed-layer and etching yield (or the movement flux, r_6) in terms of incoming fluxes. To solve the differential algebraic equations, ABACUSS II simulation package was used [7]. ABACUSSII is a programming language and simulation environment that was developed to solve differential equations with algebraic constraints. For simple system such as silicon etching with chlorine chemistry, which is demonstrated here, the equations could be solved analytically by setting the time derivatives shown above to zero, which represents a steady-state. But for the more complicated systems which involves more elements, this simple calculation fails and this will be discussed further in Chapter 4.

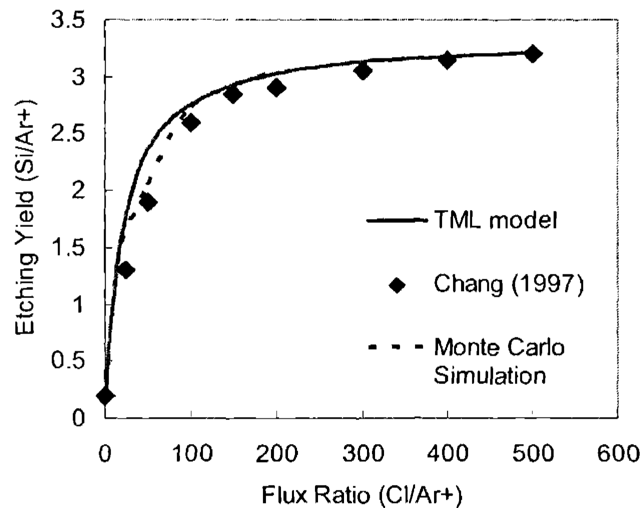

Figure 3.3 Translating mixed-layer simulation for silicon etching with chlorine chemistry, compared with experimental data and a Monte-Carlo simulation result. Ion energy is 100 eV.

Figure 3.3 is a result of a calculation compared with a Monte-Carlo simulation result and a set of data from a literature by Chang *et al.*[3] showing the translating mixed-layer model calculation agrees with Monte-Carlo simulation as well as the measured data. One of the advantages of the translating mixed-layer modeling over Monte-Carlo simulation is calculation speed. The calculation time for the translating mixed-layer simulation was 100 to 10000 times faster than that of Monte-Carlo simulation calculation with a given condition. Calculation time for Monte-Carlo simulation in Figure 3.3 was 6 hours while that of translating mixed-layer simulation was 15 seconds. The ion energy used was 100 eV.

Table 3.2 Kinetic parameters used for the translating mixed-layer model compared with parameters for the active-site model[3] in modeling silicon etching with chlorine chemistry. Ion energy is 100 eV.

Parameter	TML model	Active-site model
s_l	0.3	0.3
β	5.0	3.59
Y_{Cl}	0	0
Y_{Si}	0.07	0.07

Calculating the model, the set of parameters listed in Table 3.2 is used to correctly represent the measured data.

The sticking coefficient of chlorine, s_l=0.3, is the value used to model the system using the active-site model[8]. β used in this model is 5.0 while it is 3.59 for Chang's active-site model[8]. This is because the reaction expression of the translating mixed-layer model is different from that of the active-site model. In the active-site model, ion-induced etching yield is proportional to the extent of chlorination of which maximum value is 1.0 while in the translating mixed-layer model ion-induced etching yield is proportional to the chlorine concentration in the surface layer, of

which maximum value is 2/3. In addition to that, the active-site model assumed $SiCl_4$ as the etching product but our translating mixed-layer model's etching product is assumed to be $SiCl_2$, which has been experimentally verified by Jin *et al.*[9] The sputtering of chlorine is neglected and the sputtering yield coefficient for silicon is used the value from the active-site model, which should be independent of the choice of the model.

3.3 Silicon Oxide Etching with Fluorine Chemistry

Modeling of silicon oxide etching with fluorine chemistry is similar to that of silicon etching with chlorine chemistry, and the reactions and the corresponding reaction rate expressions can be written as the followings :

1. Adsorption

There are two adsorption reactions, which are fluorine adsorption on silicon and fluorine adsorption on oxygen.

Fluorine adsorption on silicon is

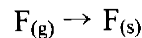

$$F_{(g)} \rightarrow F_{(s)}$$

with the rate expression of

$$r_1 = s_1 \cdot R_F \cdot (x_{Si} - \frac{1}{2} x_F \cdot \frac{2x_{Si}}{2x_{Si} + x_O})$$

assuming there are two sites available per silicon for fluorine adsorption. It is also assumed that the chemical affinities of fluorine to oxygen and to silicon are equal. The term in the parenthesis

$$x_F \cdot \frac{2x_{Si}}{2x_{Si} + x_O}$$

is the concentration of fluorine in the translating mixed-layer incorporated with silicon.

Similarly, fluorine adsorption on oxygen is

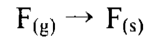

$$F_{(g)} \rightarrow F_{(s)}$$

with the rate expression of

$$r_2 = s_2 \cdot R_F \cdot (x_O - x_F \cdot \frac{x_O}{2x_{Si} + x_O})$$

because number of available adsorption sites per oxygen is assumed to be one.

Adsorption of ions are implantation-like, as we assumed for silicon etching case.

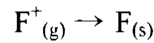

$$F^{+}_{(g)} \rightarrow F_{(s)}$$

with the rate expression of

$$r_3 = s_3 \cdot R_{F^+}$$

where the sticking coefficient is unity.

2. Surface reaction

There are two ion-induced chemical etching reactions. For silicon the reaction is

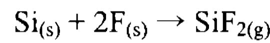

$$Si_{(s)} + 2F_{(s)} \rightarrow SiF_{2(g)}$$

with the rate expression of

$$r_4 = \beta_1 \cdot x_F \cdot \frac{2x_{Si}}{2x_{Si} + x_O}$$

which means the production of SiF_2 is proportional to the concentration of fluorine incorporated with silicon in the translating mixed-layer.

For oxygen adsorption, the reaction is

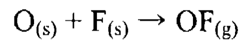

$$O_{(s)} + F_{(s)} \rightarrow OF_{(g)}$$

with the rate expression of

$$r_5 = \beta_2 \cdot x_F \cdot \frac{x_O}{2x_{Si} + x_O}$$

which indicates the production rate of OF is proportional to the concentration of fluorine

incorporated with oxygen.

Sputtering reaction of silicon is

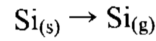

with the rate expression of

$$r_6 = Y_{Si} \cdot x_{Si}$$

For oxygen,

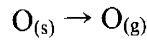

with the rate expression of

$$r_7 = Y_O \cdot x_O$$

And for fluorine,

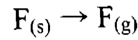

with the rate expression of

$$r_8 = Y_F \cdot x_F$$

3. Movement flux

For net etching regime, the movement flux compensating the difference between incoming adsorption and outgoing removal flux is from the substrate to the surface volume or the translating mixed-layer, which can be expressed as the following:

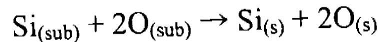

and the corresponding rate expression is

$$r_9 = \frac{1}{3}(-r_1 - r_2 - r_3 + 3r_4 + 2r_5 + r_6 + r_7 + r_8)$$

and the movement flux is essentially the etching yield because it is the net flux removed.

4. Calculating the etching yield and the surface composition

Using elemental mass balance,

$$\frac{dx_{Si}}{dt} = -r_4 - r_6 + r_9$$

$$\frac{dx_O}{dt} = -r_6 - r_7 + 2r_9$$

$$\frac{dx_F}{dt} = r_1 + r_2 + r_3 - 2r_4 - r_5 - r_8$$

Integrating the equations to a steady state gives the concentration of each species in the translating mixed-layer and the net etching yield (or the movement flux, r_9) in terms of incoming fluxes.

The calculation result is shown in Figure 3.4. It shows the translating mixed-layer simulation agrees with a set of data by Gray *et al.*[4] The ion bombardment energy used is 350 eV. To calculate the model, kinetic parameters used are listed in Table 3.3.

Table 3.3 Kinetic parameters used for the translating mixed-layer model compared with parameters for the active-site model[4] in modeling silicon oxide etching with fluorine chemistry. Ion bombardment energy is 350 eV.

parameter	TML model	Active-site model
s_1	0.04	0.033
s_2	0.04	N/A
β_1	1.3	0.740
β_2	1.3	N/A
Y_{Si}	0.2	0.2
Y_O	0.2	0.2
Y_F	0.2	N/A

In Gray's model, the assumed ion-induced etching reaction is

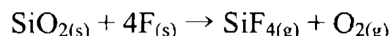

$$SiO_{2(s)} + 4F_{(s)} \rightarrow SiF_{4(g)} + O_{2(g)}$$

which indicates it involves only one reaction to remove both silicon and oxygen. But in our model, silicon and oxygen are assumed to be removed by separate reactions. As explained in the previous section, the ion-induced etching yield is set to be proportional to the extent of fluorination in the active-site model, while it is proportional to the concentration of fluorine in the translating mixed-layer model. Therefore, the kinetic parameter values used for our model are different from those for Gray's active-site model, although both models represent the same set of measured data.

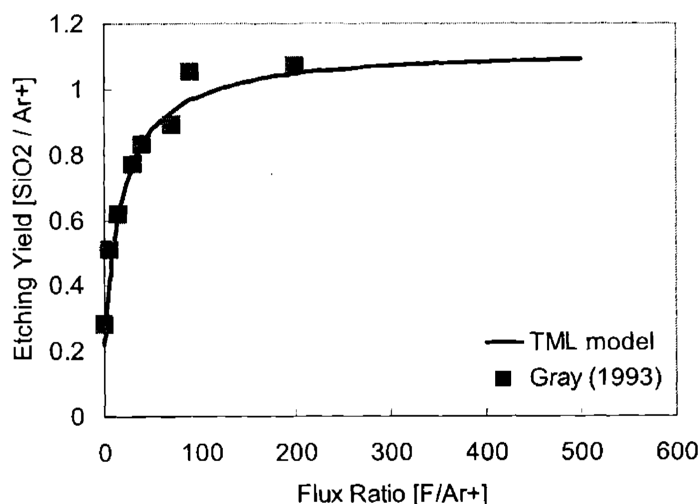

Figure 3.4 A translating mixed-layer model calculation result for silicon oxide etching with fluorine chemistry compared with experimental data. Ion bombardment energy is 350 eV.

3.4 Conclusion

A novel surface kinetic model using translating mixed-layer representation was proposed and demonstrated. In this model, a translating mixed-layer was constructed where total number of atoms is conserved as the etching proceeds, to have a convection or movement flux from or to

the substrate volume which corresponds to the difference between the adsorption flux and removal flux.

The model is demonstrated for silicon etching with chlorine chemistry and silicon oxide etching with fluorine chemistry showing that the result agrees well with measured data as well as previously developed Monte-Carlo simulation result. The computation speed of the translating mixed-layer model was 100 to 10000 times faster than that of Monte-Carlo simulation.

3.5 REFERENCE

1. J. W. Butterbaugh, D. C. Gray, and H. H. Sawin, J. Vac. Sci. Technol. B **9** (3), 1461 (1991).
2. H. Chae, S. A. Vitale, and H. H. Sawin, J Vac Sci Technol A **21** (2), 381 (2003).
3. J. P. Chang and H. H. Sawin, J. Vac. Sci. Technol. A **15** (3), 610 (1997).
4. D. C. Gray, I. Tepermeister, and H. H. Sawin, J. Vac. Sci. Technol. B **11** (4), 1243 (1993).
5. C. F. Abrams and D. B. Graves, IEEE Trans. Plasma Sci. **27** (5), 1426 (1999).
6. A. P. Mahorowala and H. H. Sawin, J. Vac. Sci. Technol. B **20** (3), 1064 (2002).
7. P. I. Barton, (MIT, 2001).
8. J. P. Chang, A. P. Mahorowala, and H. H. Sawin, J. Vac. Sci. Technol. A **16** (1), 217 (1998).
9. W Jin, Ph.D. thesis, MIT, 2004.

Chapter 4. Modeling of Silicon Oxide Etching in Fluorocarbon Chemistry

Fluorocarbon chemistry is by its nature very complex. Feed gas is fragmented into many neutral and ion species, and etching and deposition occur simultaneously. Because of the complexity it is difficult to understand the surface kinetics accurately. To understand the surface kinetics accurately the roles of variables such as gas composition, ion-to-neutral flux ratio, concentration of every species in the surface volume need to be understood.

In the past, the active-site model[1-3] approach has been used to model etching surface kinetics. This simple modeling approach works well for simpler system such as silicon etching with chlorine chemistry. In this model, the number of silicon atoms is assumed constant. The generation of Si atoms as etching occurs is associated with the assumed flux of silicon into the surface as this layer moves into the surface during silicon etching. The number of atoms (and therefore thickness) in the layer is a function of the extent of halogenation θ. Because of these assumptions it is impossible to handle deposition and is very difficult if not impossible to model etching with multiple etching species. Although the deposition phenomena itself can be handled using the active-site model approach assuming a lumped surface reaction[4], the simultaneous etching and deposition cannot be handled using a simple active-site model.

4.1 Translating Mixed-Layer (TML) Model

When silicon oxide etching in fluorocarbon chemistry has been modeled, it has been assumed that there is a finite thickness of fluorocarbon film on oxide surface[5-9]. Zhang *et al.*[8]

assumed that fluorine and other species diffuse through the steady-state film to have etching reactions at the interface between the fluorocarbon film and the oxide. Rueger *et al.*[9] suggested that the deposited fluorocarbon layer, which has a finite thickness, reacts with oxide. Schaepkens *et al.*[7] modeled silicon oxide etching in fluorocarbon chemistry using a steady-state fluorocarbon film model showing etching yield is inversely proportional to the steady-state fluorocarbon thickness. Tatsumi *et al.*[5] attributed lower etching rate with thicker fluorocarbon film to the ion bombardment energy loss.

The well-mixed moving film concept, which is explained in Chapter 3, is applied to oxide etching system. The thickness of the moving boundary layer is approximately 25 Å which is comparable with the range associated with the ion bombardment which causes incorporation and atomic mixing on this length scale[10-12]. Because of the mixing, we can reasonably represent the translating mixed-layer as having a uniform composition.

Table 4.1 is the list of symbols used in the equations for oxide etching modeling.

Table 4.1 List of symbols used in equations.

symbol	comment
s	Sticking coefficient
R_i	flux of species i divided by total ion flux
β	Reaction coefficient of ion-induced etching
a	Reaction coefficient of surface recombination reaction
Y_i	Sputtering yield coefficient of species i
x_i	Concentration of species i in the well-mixed moving film
r_i	Reaction rate in yield domain (reaction rate divided by total ion flux)

1. Adsorption

The adsorption reactions and the corresponding reaction rate equations for oxide etching in fluorocarbon plasma are listed in

Table 4.2.

Table 4.2 Adsorption Reactions of silicon oxide etching with fluorocarbon chemistry.

Reaction	Rate Expression	Comment
$F_{(g)} \rightarrow F_{(s)}$	$r_{A1} = s_{F_on_Si} \cdot R_F \cdot x_{Si_for_F}$	F neutral adsorption on Si
$F_{(g)} \rightarrow F_{(s)}$	$r_{A2} = s_{F_on_C} \cdot R_F \cdot x_{C_for_F}$	F neutral adsorption on C
$F^{+}_{(g)} \rightarrow F_{(s)}$	$r_{A3} = s_{F^+} \cdot R_{F^+}$	F ion adsorption
$C_xF_{y(g)} \rightarrow xC_{(s)} + yF_{(s)}$	$r_{A5} = s_{C_xF_y_on_O} \cdot R_{C_xF_y} \cdot x_{O_for_C}$	C_xF_y neutral adsorption on oxygen
$C_xF_{y(g)} \rightarrow xC_{(s)} + yF_{(s)}$	$r_{A6} = s_{C_xF_y_on_C} \cdot R_{C_xF_y} \cdot x_C$	C_xF_y neutral adsorption on carbon
$C_xF_y^{+}{}_{(g)} \rightarrow xC_{(s)} + yF_{(s)}$	$r_{A7} = s_7 \cdot R_{C_xF_y^+}$	C_xF_y ion adsorption

Calculating adsorption reactions, the following assumptions are made.

1. Fluorine is adsorbed preferentially on silicon and carbon. There is no fluorine adsorption on oxygen. The McFeely *et al.*[13] and Butterbaugh *et al.*[14] reported that fluorine is preferentially adsorbed on silicon because it is energetically favored.
2. Carbon (or fluorocarbon) is adsorbed preferentially on oxygen and carbon. There is no carbon adsorption on silicon. This is also the observation by McFeely *et al.*[13] and Butterbaugh *et al.*[14]
3. There are two possible adsorption sites per silicon, three possible adsorption sites per

carbon, one possible adsorption site per oxygen. Jin *et al.*[15] reported that a silicon surface exposed to chlorine plasma tend to have $SiCl_2$-like surface, which indicates a silicon atom uses two bonds as adsorption sites, which is also an assumption in Chapter 3. For oxygen and carbon, maximum number of dangling bonds or active sites is assumed to be one less than the total number of bonds per atom because one bond has to be used to be connected to the solid structure.

4. In the translating mixed-layer, the sticking and reaction probability of each species is calculated solely based on the number of possible active sites described above.
5. Ions are 'implanted' in the translating mixed-layer, making adsorption independent of surface composition and sticking coefficient unity.

Based on the assumptions, the effective concentration expressions are written as the followings.

$$x_{Si_for_F} = x_{Si} - \frac{1}{2} x_F \frac{2x_{Si}}{2x_{Si} + 3x_C}$$

$$x_{C_for_F} = x_C - \frac{1}{3} x_F \frac{3x_C}{2x_{Si} + 3x_C}$$

$$x_{O_for_C} = x_O - 3x_C \frac{x_O}{3x_C + x_O + x_F}$$

$$x_{C_for_C} = x_C - \frac{1}{3} \cdot 3x_C \frac{3x_C}{3x_C + x_O + x_F}$$

where $x_{i_for_j}$ is effective concentration of species *i* for adsorption of species *j*.

2. Etching (Removal)

The entire etching reactions and the corresponding reaction rate equations are listed in Table 4.3. The set of ion induced reactions is a lumped reaction set instead of actual detailed complete equations. A lumped set of reactions is a subset of the complete set of reactions which has been selected such that all elemental species can be accounted for and the overall reaction

kinetics adequately modeled. This limited set is desirable as it limits the number of rates that must be experimentally determined, but which adequately represents the systems behavior. In addition, using lumped reactions also minimizes arbitrariness. If there is an excessive number of fitting parameters the problem may become arbitrary. The rates of this set of reactions are determined by the elemental composition of the translating mixed-layer, thereby not requiring the tracking of all the possible chemical molecular species in the surface layer.

Note that a CF_4 surface production reaction, a surface recombination reaction, is included. This reaction rate is proportional to the incoming atomic fluorine flux. Butterbaugh *et al.*[14] reported that the surface CF_4 production reaction is crucial in determining etching yield behavior of silicon oxide etching in fluorocarbon chemistry

Table 4.3 The lumped etching reactions.

Reaction	Rate expression	Comment
$Si_{(s)} \rightarrow Si_{(g)}$	$r_{S1} = Y_{Si} \cdot x_{Si}$	Physical sputtering of Si
$O_{(s)} \rightarrow O_{(g)}$	$r_{S2} = Y_O \cdot x_O$	Physical sputtering of O
$C_{(s)} \rightarrow C_{(g)}$	$r_{S3} = Y_C \cdot x_C$	Physical sputtering of C
$F_{(s)} \rightarrow F_{(g)}$	$r_{S4} = Y_F \cdot x_F$	Physical sputtering of F
$Si_{(s)} + 2F_{(s)} \rightarrow SiF_{2(g)}$	$r_{E1} = \beta_{SiF2} \cdot x_F \cdot \frac{2x_{Si}}{2x_{Si} + 3x_C}$	Ion-induced SiF_2 production reaction
$Si_{(s)} + 4F_{(s)} \rightarrow SiF_{4(s)}$	$r_{E2} = \beta_{SiF4} \cdot (x_F \cdot \frac{2x_{Si}}{2x_{Si} + 3x_C})^2$	Ion-induced SiF_4 production reaction
$C_{(s)} + O_{(s)} \rightarrow CO_{(g)}$	$r_{E3} = \beta_{CO} \cdot x_O \cdot \frac{3x_C}{2x_{Si} + 2x_C}$	Ion-induced CO production reaction
$C_{(s)} + 2F_{(s)} \rightarrow CF_{2(g)}$	$r_{E4} = \beta_{CF} \cdot x_F \cdot \frac{x_C}{x_{Si} + x_C}$	Ion-induced CF_2 production reaction
$C_{(s)} + 4F_{(s)} \rightarrow CF_{4(g)}$	$r_{E5} = \alpha_{CF} \cdot x_F \cdot \frac{x_C}{x_{Si} + x_C} \cdot R_F$	Fluorocarbon film removal by incoming fluorine flux

3. Compensating movement flux and calculating surface composition, etching yield.

Movement flux is the difference between the adsorption flux and the removal flux. In a net etching regime, the removal flux is greater than the adsorption flux making the direction of the movement flux from the substrate to the surface translating mixed-layer.

The movement flux is expressed,

$$r_{movement} = \sum r_{adsorption} - \sum r_{removal}$$

Elemental mass balance equations are

$$\frac{dx_{Si}}{dt} = \sum r_{Si_addition} - \sum r_{Si_removal}$$

$$\frac{dx_{O}}{dt} = \sum r_{O_addition} - \sum r_{O_removal}$$

$$\frac{dx_{C}}{dt} = \sum r_{C_addition} - \sum r_{C_removal}$$

$$\frac{dx_{F}}{dt} = \sum r_{F_addition} - \sum r_{F_removal}$$

Integrating the equations to a steady state with the initial condition of pure silicon oxide (x_{Si}=1/3, x_O=2/3) gives concentration of each species in the translating mixed-layer and the etching yield (which is essentially the movement flux, $r_{movement}$) in terms of incoming fluxes.

The equations could be solved by setting up the above time derivatives to zero, which represent a steady state, and it gives a set of nonlinear equations. When solved with the nonlinear equations with Mathcad or Mathematica, the following solutions were obtained.

$$\begin{pmatrix} x_{Si} \\ x_O \\ x_C \\ x_F \end{pmatrix} = \begin{pmatrix} 0 \\ 0 \\ 0 \\ 1 \end{pmatrix}$$

or

$$\begin{pmatrix} x_{Si} \\ x_O \\ x_C \\ x_F \end{pmatrix} = \begin{pmatrix} 1 \\ 0 \\ 0 \\ 0 \end{pmatrix}$$

or

$$\begin{pmatrix} x_{Si} \\ x_O \\ x_C \\ x_F \end{pmatrix} = \begin{pmatrix} 0 \\ 0 \\ \frac{sR}{\beta + sR} \\ \frac{\beta}{\beta + sR} \end{pmatrix}$$

The case is with CF_2 flux and one lumped ion enhanced etching reaction ignoring surface recombination reaction and sputtering reactions. The above solutions are mathematically correct, but none of them represent the surface composition during the oxide etching, which should be a mixture of all of the elements. To solve the differential equations with algebraic constraints, ABACUSSII was used. ABACUSSII is a simulation environment and a programming language developed to solve differential algebraic systems[16].

Measured neutrals and ion composition (Chapter 2) were used as inputs and the simulation results were compared to the measured etching yield for verification.

4.2 Determining Kinetic Parameters

To determine the kinetic parameters, a systematic approach as shown in Figure 4.1 is used. A published data by Butterbaugh *et al.*[14] were used as the first step. The reaction rate constants and two sticking coefficients for F and CF_2 were determined.

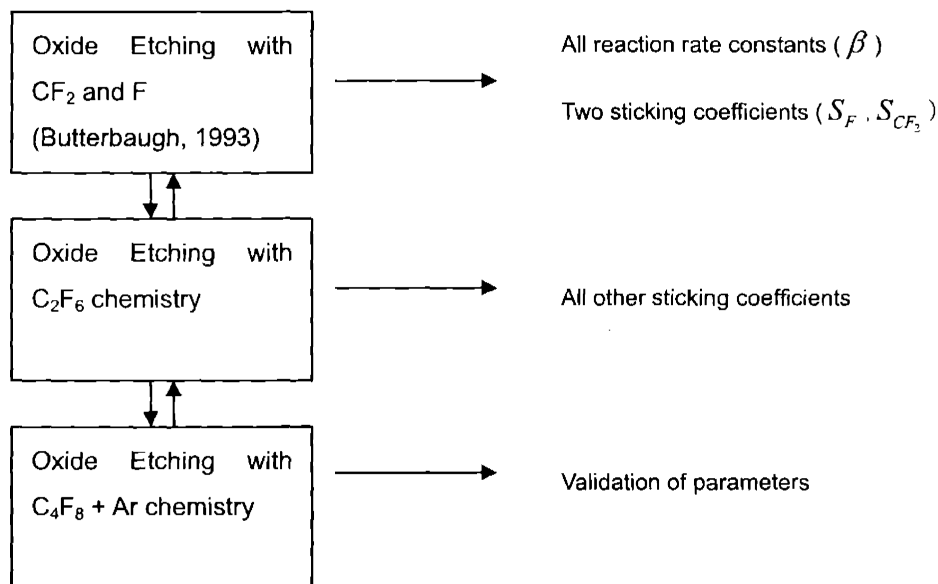

Figure 4.1 A flow diagram for determining kinetic parameters of oxide etching in fluorocarbon chemistry.

The same model was applied to C_2F_6 chemistry with more gas species to find all other sticking coefficients. The C_2F_6 flux composition and etching rate data are collected over a broad range of conditions, thereby providing an adequate basis for determining the number of necessary coefficients. Validation of the model is made by applying these kinetics to the C_4F_8 + Ar chemistry with data again taken over broader ranges of etching conditions and comparing with a measured data set.

Table 4.4 Kinetic parameters of translating mixed-layer model for silicon oxide etching in fluorocarbon plasmas. Ion energy is 300 eV.

symbol	value	comment
$s_{F_on_Si}$	0.7	sticking coefficient of F on Si
$s_{F_on_C}$	0.7	sticking coefficient of F on C
$s_{CF_on_O}$	0.7	sticking coefficient of CF on O
$s_{CF_on_C}$	0.7	sticking coefficient of CF on C
$s_{CF_2_on_O}$	0.7	sticking coefficient of CF_2 on O
$s_{CF_2_on_C}$	0.7	sticking coefficient of CF_2 on C
$s_{CF_3_on_O}$	0.7	sticking coefficient of CF_3 on O
$s_{CF_3_on_C}$	0.7	sticking coefficient of CF_3 on C
$s_{\text{higher mass species}}$	0	sticking coefficient of higher mass species
β_{SiF_2}	8.0	rate coefficient of ion-induced SiF_2 production
β_{SiF_4}	8.0	rate coefficient of ion-induced SiF_4 production
β_{CO}	12.0	rate coefficient of ion-induced CO production
β_{CF}	9.0	rate coefficient of ion-induced CF_2 production
β_{O}	6.0	rate coefficient of ion-induced O removal process
β_{F}	6.0	rate coefficient of ion-induced F removal process
Y_{Si}	0.3	sputtering yield coefficient of Si
Y_{O}	0.3	sputtering yield coefficient of O
Y_{C}	0.3	sputtering yield coefficient of C
Y_{F}	0.6	sputtering yield coefficient of F
α_{CF}	5.0	reaction rate coefficient of CF_4 production by surface recombination

Table 4.4 is a list of kinetic parameters of the translating mixed-layer model for silicon oxide etching in fluorocarbon plasmas. Sticking of high mass fluorocarbon neutrals that contains more than two carbons is neglected because of low sticking coefficients and relatively low fluxes compared to lower mass fluorocarbons.

4.3 Result and Discussion

4.3.1 CF_2-F surface plot

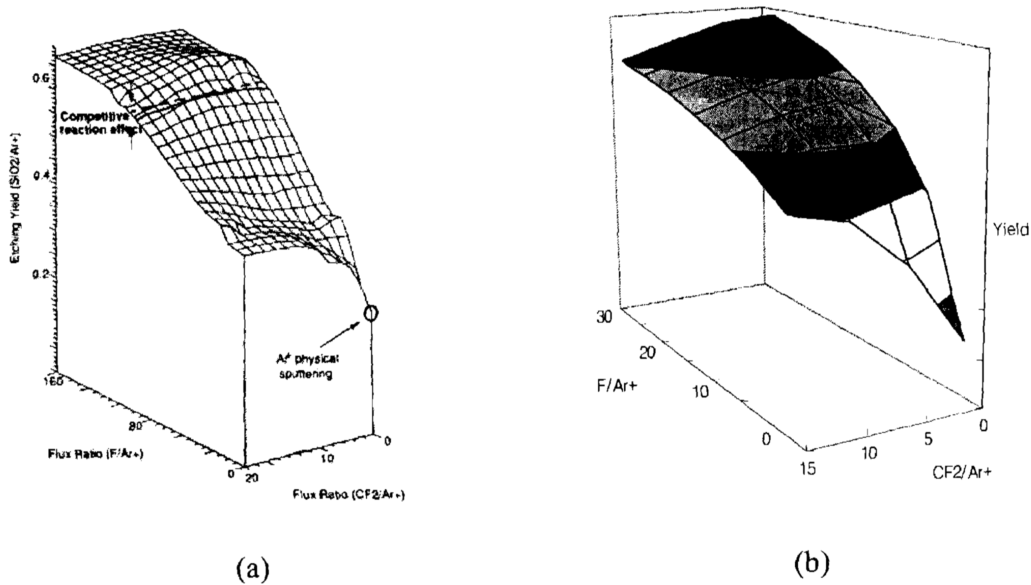

Figure 4.2 A translating mixed-layer simulation result compared with experimental data for oxide etching with F and CF_2.

Figure 4.2 shows a comparison between a measured data and a simulation result. The measured data is from a measurement by Butterbaugh *et al.*[14], where a neutral and ion beams were used to mimic a real plasma etching condition.

In this surface plot there are two major features.

1. Increase in the etching yield with increasing F/ion flux. At higher F/ion flux region, the

etching yield becomes independent of F/ion increase.

2. Increase in the etching yield with increasing CF_2/ion flux at very low F/ion flux and relatively invariant etching yield with increasing CF_2/ion flux at higher/moderate F/ion flux.

The comparison shows that the translating mixed-layer simulation captures the major shapes of the experimental surface plot. The actual etching yield and other detailed shape can be varied with experimental conditions.

4.3.2 Verification of the model with measured data sets

Figure 4.3 shows simulation results compared with measured data for two chemistries, C_2F_6 and C_4F_8 + 80%Ar. RF coil power and operating pressure are varied and measured/simulated etching yield. The data set shown in Chapter 3 was used for the verification. The simulation using the translating mixed-layer model represents all the major trends for two chemistries, which is a good verification of the model.

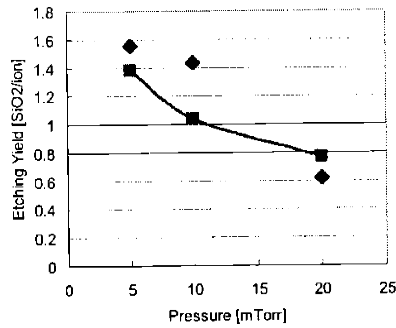

(a)

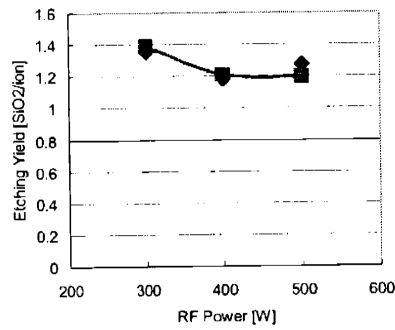

(b)

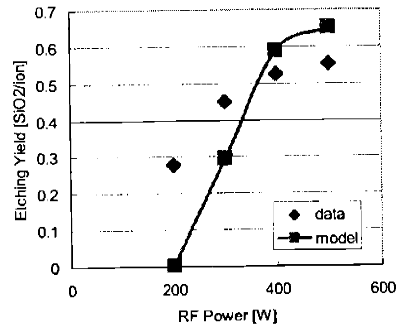

(c)

Figure 4.3 Translating mixed-layer simulation results compared with measured data for two chemistries. (C_2F_6 and C_4F_8 + 80% Ar) (a) C_2F_6 chemistry, varying operating pressure. (b) C_2F_6 chemistry, varying RF coil power. (c) C_4F_8 + 80%Ar chemistry, varying RF coil power.

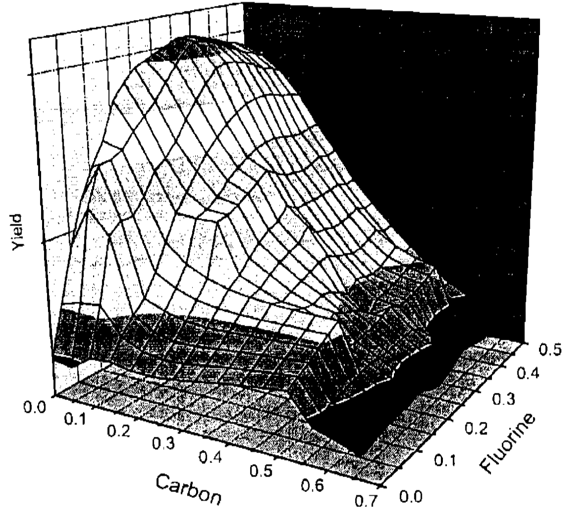

(a)

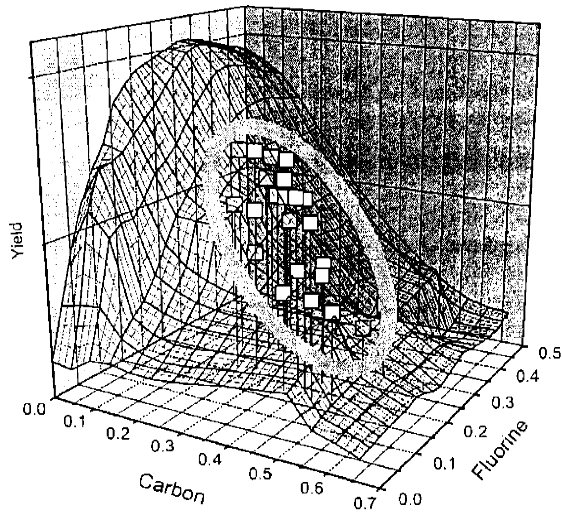

(b)

Figure 4.4 Calculated etching yield as a function of carbon and fluorine concentration in the moving boundary layer. (a) Surface plot. (b) Connected wire plot showing results for C_2F_6 and C_4F_8 + 80% Ar chemistry. Under most etching conditions, the etching yield falls in the oval region. The data points represent simulation results with the following conditions: C_2F_6 plasma, 5 mTorr, 200-500 W RF coil power; C_2F_6 plasma, 300 W RF coil power, 5-20 mTorr; C_4F_8 + 80% Ar plasma, 5 mTorr, 200-500 W RF coil power.

4.3.3 A new surface plot – etching yield as a function of the composition in the translating mixed-layer

Conducting more simulations, a surface plot shown in Figure 4.4 is constructed. It shows etching yield as a function of composition of translating mixed-layer, carbon and fluorine concentration in the translating mixed-layer volume. As the carbon concentration increases etching yield decreases and as the fluorine concentration increases etching yield increases.

Note that under most etching conditions, the etching yield falls in the oval region as shown in Figure 4.4(b). In this region, the etching yield shows a weak dependence on fluorine but a strong dependence on carbon. The data points in the plot represent simulation results with the following conditions: C_2F_6 plasma, 5 mTorr, 200-500 W RF coil power; C_2F_6 plasma, 300 W RF coil power, 5-20 mTorr; C_4F_8 + 80% Ar plasma, 5 mTorr, 200-500 W RF coil power.

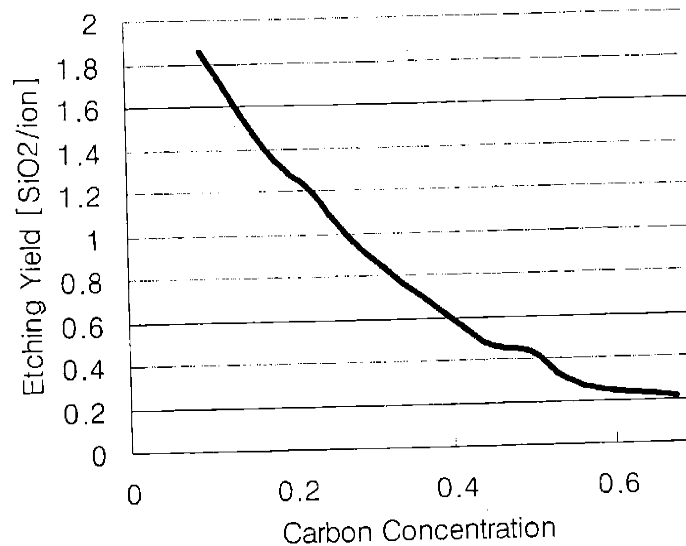

Figure 4.5 Etching yield vs. carbon concentration in the translating mixed-layer at fluorine concentration of 0.3.

A simulation result shown Figure 4.5 is the calculated etching yield as a function of carbon concentration in the moving boundary layer, which is a cross section of the surface plot of Figure 4.4 at fluorine concentration of 0.3. As carbon concentration, which is equivalent to measured fluorocarbon thickness, increases the etching yield is monotonically decreasing. This agrees with previous experimental results reported by Standaert *et al.*[7] The translating mixed-layer simulation adequately explains this measured data. In addition, the translating mixed-layer modeling can also represent etching in C_4F_8 in which F concentrations are sufficiently low, that F etching does not dominate the etching (as was assumed in previous model which is appropriate for etched rich in F such as C_2F_6).

4.3.4 Effect of plasma variables

The effect of neutral composition on etching yield is shown in Figure 4.6. As carbon contents increases in the neutral flux, etching yield decreases. This simulation is done with C_2F_6 chemistry with varying CF and CF_3 ratio. The result confirms that the carbon contents and the fluorine contents in the incoming flux contribute primarily to the deposition and etching, respectively. For this simulation, the plasma composition of C_2F_6 at 5 mTorr, 300 W RF coil power was used. With keeping other species fixed, ratio of CF to CF3 was varied to change neutral composition.

Figure 4.7 shows the effect of neutral-to-ion flux ratio for two chemistries: C_2F_6 and C_4F_8 + 80% Ar. For the simulation, the gas compositions at 5 mTorr, 300 W RF coil power were chosen for both chemistries and varied neutral-to-ion flux ratios.

In C_4F_8 + 80% Ar-like chemistry where 0.3% of neutrals are atomic fluorine, etching yield shows stronger dependence on the neutral-to-ion flux ratio than in C_2F_6-like chemistry with

atomic fluorine concentration of 25%. In a chemistry with very low concentration of atomic fluorine, increase in the neutral flux increases CF_x flux only to cause more deposition. In chemistry with a relatively high concentration of atomic fluorine in the neutral flux, however, increase in CF_x flux due to increase in the neutral flux is compensated by increase in fluorine flux. In addition, atomic fluorine flux causes surface recombination reaction to form CF_4 removing fluorocarbon from the surface making etching yield greater.

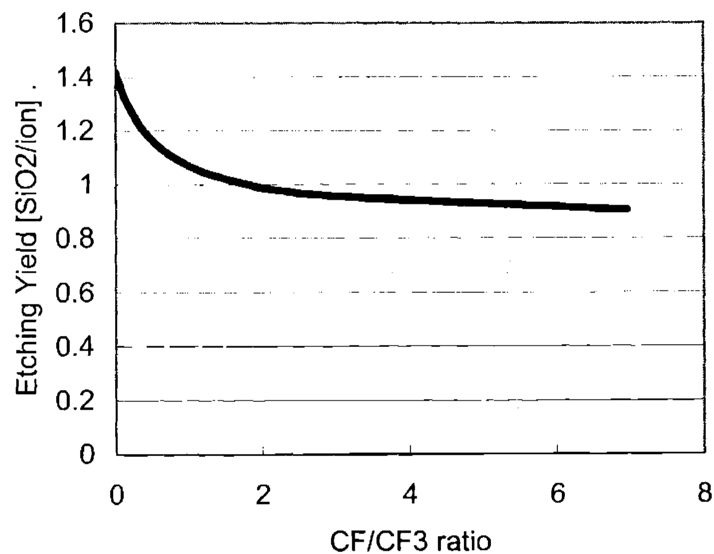

Figure 4.6 Effect of neutral composition on etching yield.

Effect of ion composition is shown in Figure 4.8. The simulation is conducted for two chemistries: C_2F_6-like(25% atomic F), C_4F_8-like(0.3% atomic F). For the simulation, the gas compositions at 5 mTorr, 300 W RF coil power were chosen for both chemistries and varied C/F ratio in the ion flux by varying F^+ ion to CF^+ ratio.

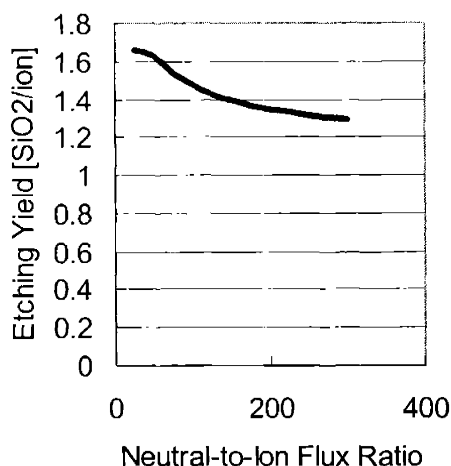

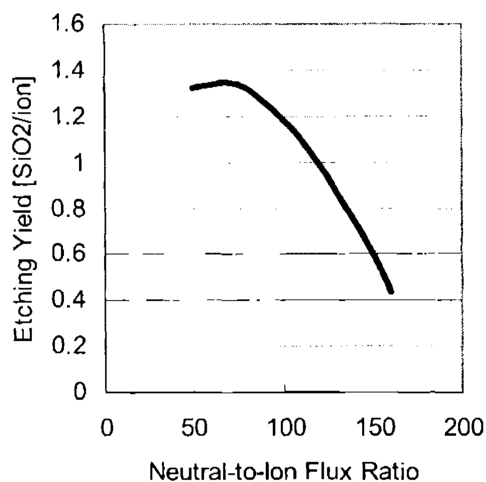

(a) (b)

Figure 4.7 Effect of neutral-to-ion flux ratio on etching yield for (a) C_2F_6–like chemistry with 25% atomic fluorine in the neutral flux. (b) C_4F_8 + 80%-like Ar chemistry with 0.3% atomic fluorine in the neutral flux.

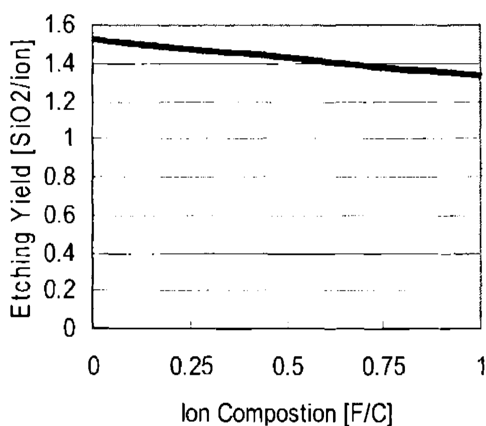

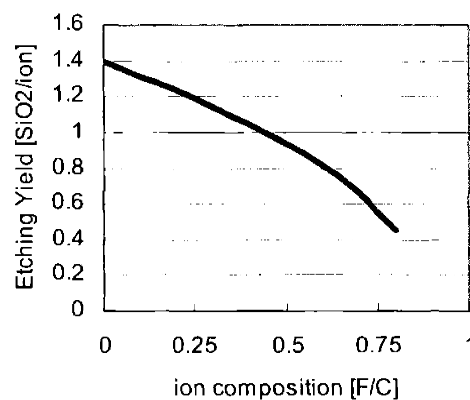

(a) (b)

Figure 4.8 Effect of ion composition on etching yield for (a) C_2F_6–like chemistry with 25% atomic fluorine in the neutral flux. (b) C_4F_8 + 80%-like Ar chemistry with 0.3% atomic fluorine in the neutral flux.

The C_4F_8-like chemistry shows stronger dependence on ion composition. This is because in C_2F_6-like chemistry, the addition of extra carbon is compensated by the surface recombination removal reaction of fluorocarbon film with atomic F flux to form CF_4. In C_4F_8-like chemistry, however, the removal of CF_x film by F flux is negligible because of the low atomic fluorine concentration.

To prove the effect of fluorocarbon film removal by atomic fluorine flux through the surface recombination reaction, the etching yield are calculated with varying ion composition for five different surface recombination reaction coefficient (α) values and the result is shown in Figure 4.9(a). Figure 4.9(b) shows the change in the slope of etching yield vs. ion composition lines (Figure 4.9(a)) with varying α. As α increases the slope decreases. This indicates that the surface recombination reaction controls the "fluorocarbon thickness" very effectively so that the change in the incoming flux composition has less significant effect when the surface recombination reaction is significant (high α). For the simulation the gas composition at 20 mTorr, 300 W RF coil power in C_2F_6 chemistry were chosen, and for seven different α values simulation was conducted with varying ion composition.

In Figure 4.10, flux of each species is increased as the etching yield for two different chemistries are simulated. For the simulation, the gas compositions at 5 mTorr, 300 W RF coil power were chosen for both chemistries and varied each neutral flux to calculate etching yield. In both chemistries increase in F flux increased etching yield, and increase in CF_x flux decreased etching yield. Addition of CF_x species with higher fluorine contents caused less etching yield reduction than those with lower fluorine contents. In C_4F_8-like chemistry, addition of extra carbon or extra fluorine has more impact. This is because at low atomic fluorine concentration, etching is more sensitive to composition change, as explained earlier.

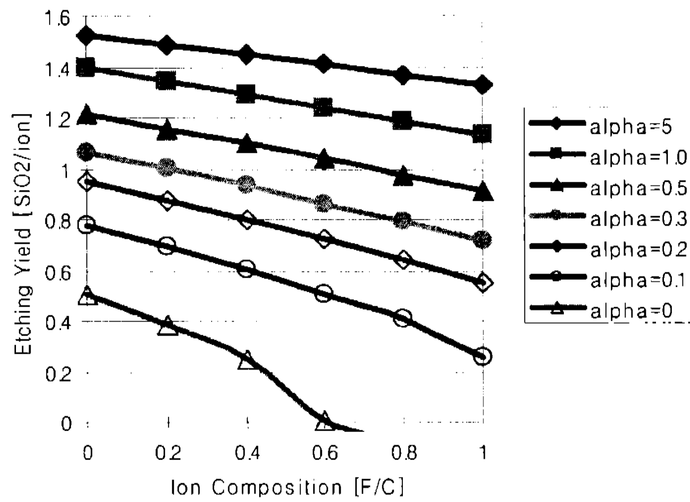

(a)

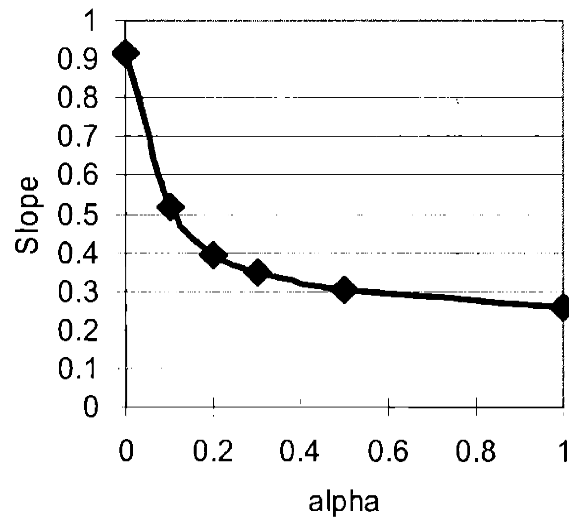

(b)

Figure 4.9 Effect of ion composition on etching yield with varying CF_4 production rate coefficient (α). (a) Etching yield change with ion composition for different alpha values. (b) slope of the curves in (a) with varying alpha.

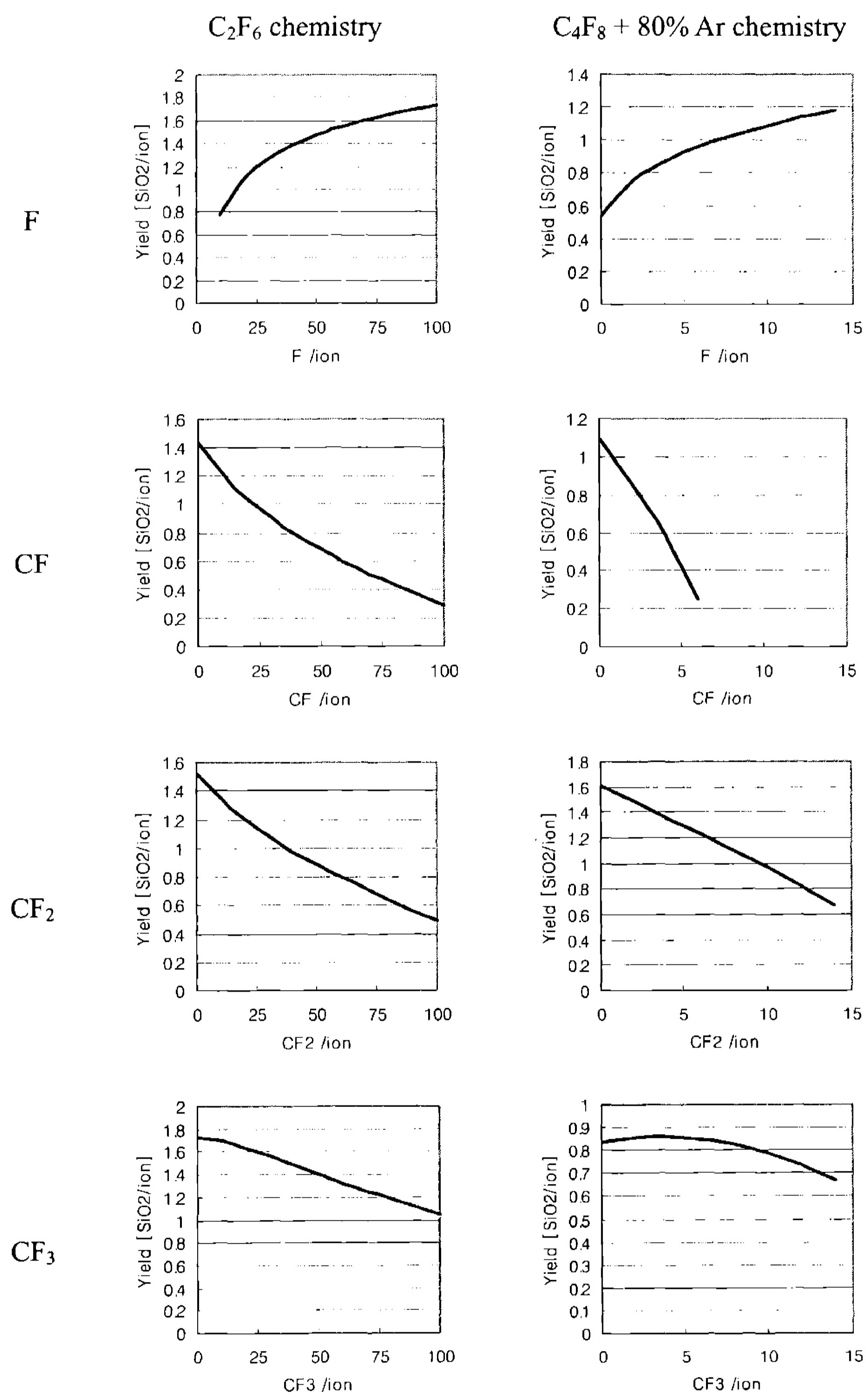

Figure 4.10 Effect of F, CF, CF_2 and CF_3 on etching yield for C_2F_6 and C_4F_8 + 80% Ar chemistries.

4.4 Conclusion

Oxide etching has been modeled using a translating mixed-layer model. Using the new modeling approach, oxide etching with fluorocarbon chemistry was successfully modeled. Carbon and fluorine were identified as primarily contributor to deposition and etching, respectively.

Atomic fluorine flux is a major factor to determine the etching behavior. With a chemistry with small amount of atomic fluorine such as C_4F_8 chemistry, etching yield shows stronger dependence on composition change in the gas flux.

4.5 References

1 J. W. Butterbaugh, D. C. Gray, and H. H. Sawin, J. Vac. Sci. Technol. B **9** (3), 1461 (1991).

2 J. P. Chang and H. H. Sawin, J. Vac. Sci. Technol. A **15** (3), 610 (1997).

3 D. C. Gray, I. Tepermeister, and H. H. Sawin, J. Vac. Sci. Technol. B **11** (4), 1243 (1993).

4 H. Chae, S. A. Vitale, and H. H. Sawin, J Vac Sci Technol A **21** (2), 381 (2003).

5 T. Tatsumi, M. Matsui, M. Okigawa et al., J. Vac. Sci. Technol. B **18** (4), 1897 (2000).

6 M. Schaepkens, G. S. Oehrlein, C. Hedlund et al., J. Vac. Sci. Technol. A **16** (6), 3281 (1998).

[7] M. Schaepkens, T.E.F.M. Standaert, N.R. Rueger et al., J. Vac. Sci. Technol. A **17** (1), 26 (1999).

[8] D. Zhang and M. J. Kushner, J. Vac. Sci. Technol. A **19** (2), 524 (2001).

[9] N. R. Rueger, J. J. Beulens, M. Schaepkens et al., J. Vac. Sci. Technol. A **15** (4), 1881 (1997).

[10] C. F. Abrams and D. B. Graves, IEEE Trans. Plasma Sci. **27** (5), 1426 (1999).

[11] A. P. Mahorowala and H. H. Sawin, J. Vac. Sci. Technol. B **20** (3), 1064 (2002).

[12] N. Layadi, V. M. Donnelly, and J. T. C. Lee, J. Appl. Phys. **81** (10), 6738 (1997).

[13] F. R. Mcfeely, J. A. Yarmoff, A. Talebibrahimi et al., Surf Sci **206** (3), 371 (1988).

[14] J. W. Butterbaugh, D. C. Gray, and H. H. Sawin, J. Vac. Sci. Technol. B **9** (3), 1461 (1991).

[15] W Jin, Ph.D. thesis, MIT, 2004.

[16] P. I. Barton, ABACUSSII syntax manual, MIT, 2001.

Chapter 5. Angular Dependence of Oxide Etching Yield in Fluorocarbon Chemistries

Recently, plasma etching feature profile modeling tools have been developed by several research groups and were able to capture many of the effects seen in real operating plasma conditions[1-6]. These modeling tools, however, cannot be used properly without adequate measurements of experimental parameters. Angular dependence of silicon oxide etching yield is one of the most significant experimental parameters that should be determined.

There have been a number of beam studies using neutral and ion beam systems to measure etching yields. In these systems, separate ion and neutral beams were used to mimic a real plasma[7-10]. This approach is relatively easy for simple ion-induced chemical etching processes, such as silicon etching with chlorine plasma because there are only a few ion and neutral species involved with the process. In oxide etching process, however, it is difficult to make a beam experimental system to simulate a real plasma for there are many chemical species involved including polymerizing neutrals.

There have been several investigations on angular dependence of oxide etching yield[7,11-16]. But these measured angular dependence of etching yields show disagreements: some of them show sputtering-like angular dependence[11-16] while others reported both ion-induced chemical etching characteristics and sputtering-like characteristics[7].

In oxide etching with fluorocarbon plasma, measurement is very sensitive to many experimental parameters including surface temperature, ion-to-neutral flux ratio, ion scattering, etc. Therefore, in order to make a precise measurement representing a real plasma process, these parameters must be controlled accurately. The variation of the previous measurements done by

several research groups may be attributed to the variation of experimental conditions under which the measurements were conducted.

To circumvent these difficulties, a plasma beam / quartz crystal microbalance (QCM) system is employed using a real inductively coupled high density plasma system as the beam source. The detailed description of the system is explained in the next section.

5.1 Experimental

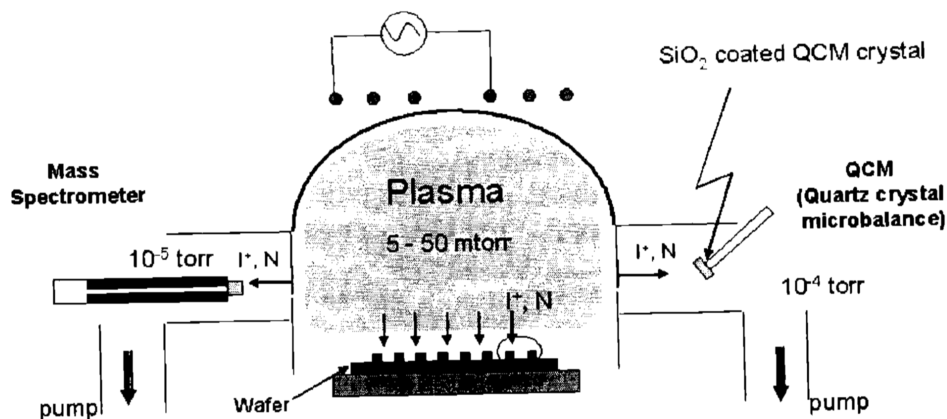

Figure 5.1 A schematic diagram of the plasma beam / QCM apparatus.

The plasma beam / QCM system used is shown in Figure 5.1, which is also described in detail in other previous publications from our group[17-19]. Ions and neutrals are extracted from an inductively coupled plasma etcher through an extraction grid to a differentially pumped QCM side chamber. The QCM sensor crystal is coated with 10,000 Å of silicon oxide deposited by PECVD. The ion bombardment energy is imposed by a negative DC bias on the extraction grid, QCM housing as well as QCM sensor. The bias can be varied from 0 to 500 V. Temperature of the QCM sensor crystal is controlled by cooling fluid, of which temperature can be varied from –

20 °C to 80 °C. To prevent beam broadening and charging of insulating surfaces, electron emitting filament is used, where a current of 1.5 Å is supplied. The QCM sensor head can be also rotated so that the ion impingement angle can be varied from 0 to 85 degrees.

All other plasma parameters such as pressure, RF power, feeding gas can be adjusted as can be done in a real plasma etcher.

5.2 Result and Discussion

5.2.1 Effect of angular dependent etching yield on feature profile

For a better understanding of influence of angular dependent etching yield on feature profile evolution, numerical profile simulations were conducted with two-dimensional (2½D) Monte Carlo technique. The calculation space is gridded into a square cellular array with 25 Å sides, a dimension comparable to the characteristic length for compositional changes in ion induced processes; e.g. the surface mixed layer caused during ion induced etching/deposition processes. Cosine distribution is assumed for neutrals and Gaussian angular distribution with Full Width at Half Maximum (FWHM) of 5° is assumed for ions, which is representative of a high-density inductively coupled plasma etching process.

To simplify the simulation, it is assumed that there is no etching or deposition on the mask, and there is no spontaneous etching of substrate material.

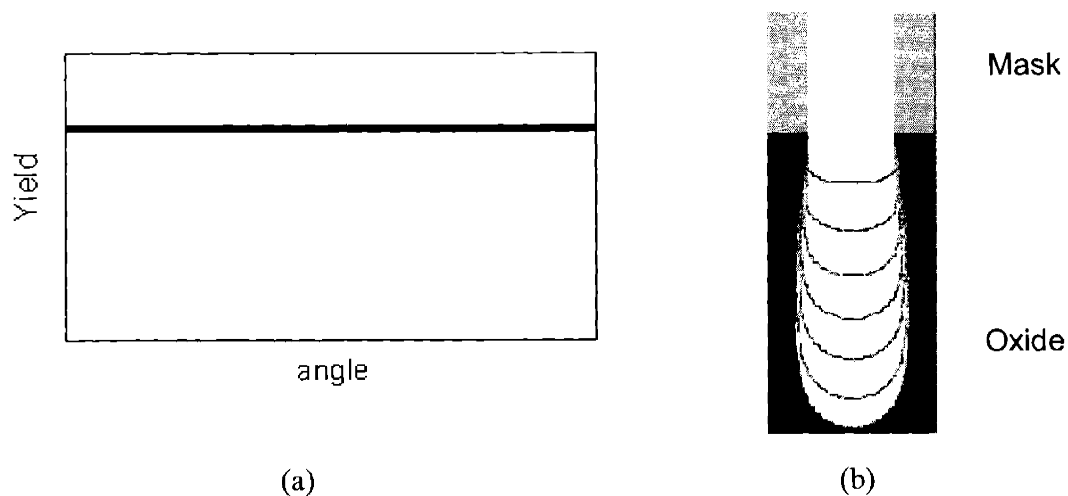

Figure 5.2. Monte Carlo simulation result where the angular dependence of etching yield curve is independent of ion incident angle. (a) Angular dependence of etching yield curve. (b) Feature profile simulation result.

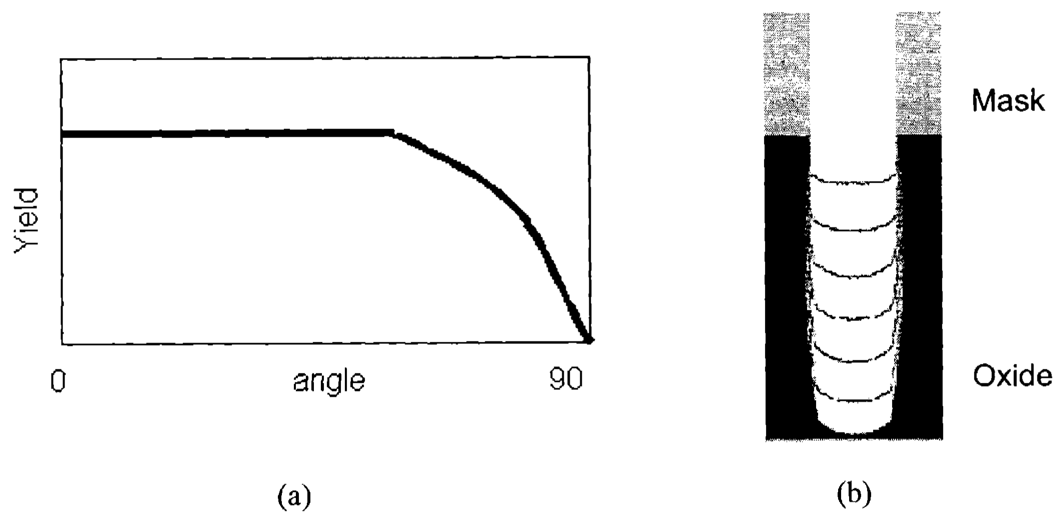

Figure 5.3. Monte Carlo simulation result where the angular dependence of etching yield curve shows a typical ion-induced chemical etching characteristics without ion scattering. (a) Angular dependence of etching yield curve. (b) Feature profile simulation result.

The simplest case is shown in Figure 5.2. In this case, the etching yield of incident ion is independent of incident angle, and each ion etches one molecule from the surface (i.e., etching yield is unity, Figure 5.2(a)) without being scattered back into gas phase. The resultant feature profile is shown in Figure 5.2(b). Significant sidewall outward bowing is observed, due to the initial Gaussian angular distribution of projected ions from the top of the feature. The bottom is also highly bowed, which is also attributed to the angular distribution of ions.

In reality, however, etching yield is dependent upon the ion incident angle. Typical angular dependence of etching yield curve is shown in Figure 5.3 (a), which is commonly observed in case of ion-induced chemical etching systems, such as polysilicon etching in chlorine plasma[20]. Because of reduced etching probability at high ion incident angle, the simulation result shows less sidewall bowing, in Figure 5.3 (b).

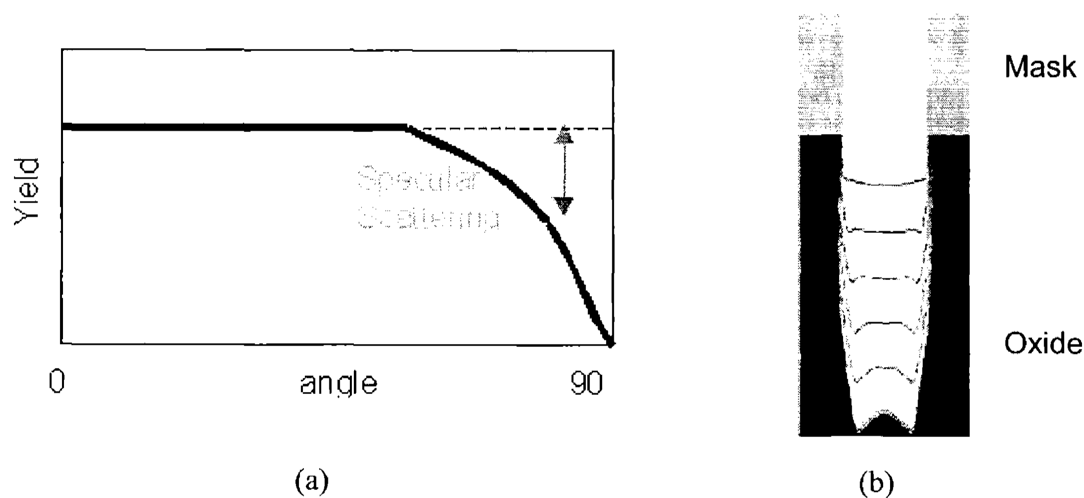

Figure 5.4. Monte Carlo simulation result where the angular dependence of etching yield curve shows a typical ion-induced chemical etching characteristics with ion scattering. (a) Angular dependence of etching yield curve. (b) Feature profile simulation result.

For a more realistic case, the ion scattering is introduced as shown in Figure 5.4 (a). As shown in Figure 5.4 (b), microtrenching is observed. Ions striking the sidewall at glancing angles have high probability of scattering and they tend to be focused to result in an enhanced etching around the foot of the sidewall. There are also slight mask undercutting and sidewall bowing.

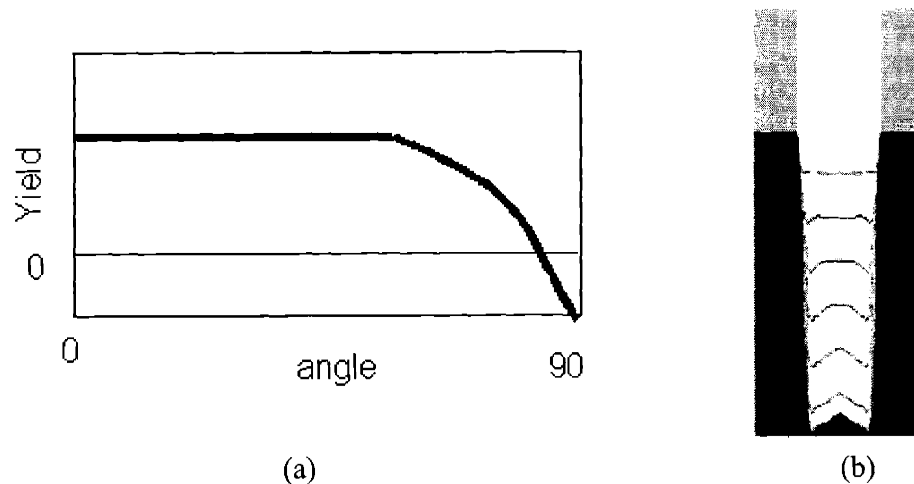

Figure 5.5. Monte Carlo simulation result where the angular dependence of etching yield curve shows a typical ion-induced chemical etching characteristics with isotropic deposition. (a) Angular dependence of etching yield curve. (b) Feature profile simulation result.

In oxide etching with fluorocarbon chemistry, both etching and deposition occur simultaneously. With the inclusion of isotropic deposition, the sidewall is covered with protective fluorocarbon film and becomes straight, as shown in Figure 5.5.

5.3 Etching Yield vs. Ion Bombardment Energy

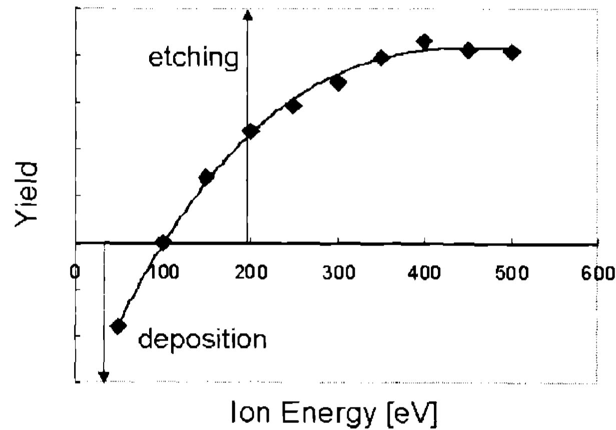

Figure 5.6. Oxide etching yield vs. ion bombardment energy. CHF_3 plasma, 5 mTorr, 20°C sample temperature, 400 W RF source power.

Figure 5.6 shows a typical etching yield curve vs. ion bombardment energy. It is a monotonically increasing curve as ion bombardment energy increases. In oxide etching system with fluorocarbon plasma there are always two competing processes: simultaneous etching and deposition. When overall etching rate is higher than overall deposition rate, net etching occurs as in the case of above 100 eV of ion bombardment energy in Figure 5.6, but when overall deposition rate is higher net deposition occurs as in the case of below 100 eV of ion bombardment energy.

The simple monotonically increasing curve is a combination of complicated processes, involving simultaneous etching and deposition.

5.4 A Simple Model: Combined Ion-Induced Chemical Etching Yield and Isotropic Deposition

To investigate and predict angular dependence of oxide etching in fluorocarbon deposition chemistry, a model can be suggested, which is a combination of ion-induced chemical etching and isotropic deposition, as shown in Figure 7.

With this simple model, we can explain the existence of critical angle, where etching and deposition are compensated by each other. Above the critical angle net deposition occurs because deposition component is greater than etching component, while below the critical angle net etching occurs because etching component is greater than the deposition component. This model also explains the trend of critical angle as the relative magnitude of deposition to etching changes; the critical angle decreases as the deposition component becomes greater. This prediction agrees well with the previous report by Bernacki[21], where existence of critical angle is observed.

This simple model, however, does not explain the shape of real oxide etching yield measurement data, which will be explained in the next section.

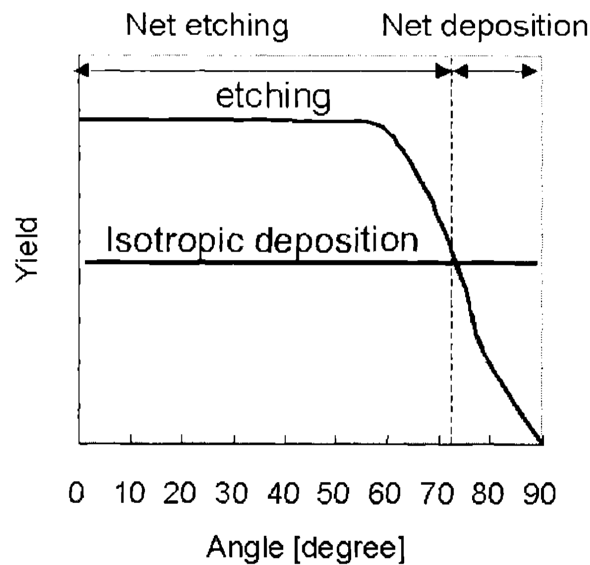

Figure 5.7. A model for angular dependence of oxide etching yield curve. Ion-induced chemical etching and isotropic etching are assumed.

5.5 An Improved Model: Combined Ion-Induced Chemical Etching and Ion-Induced Deposition

Figure 5.8(a) shows the shape of the oxide etching curves when the simple model with isotropic deposition is applied, which is described in the previous section. According to the simple model, as the isotropic deposition component increases, the entire yield curve should be shifted downward. When the actual oxide etching yield is measured, however, the yield curves look very differently (Figure 5.8 (b))[19]. Adding 40 % of oxygen to C_4F_8, which decreases deposition component in the etching process, not just shifts entire yield curve up but also changes the slope of the curve. This indicates that oxide etching in deposition chemistry is not a simple combination of ion-induced chemical etching and isotropic deposition.

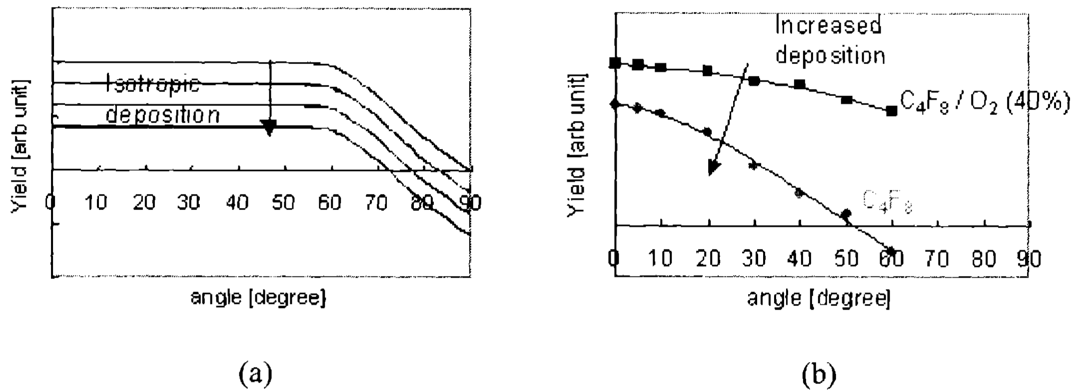

Figure 5.8 (a) Oxide etching yield curves according to the simple model with ion-induced chemical etching and isotropic deposition. (b) Oxide etching yield curves measured[19].

As mentioned earlier, measured etching yield is a combination of etching and deposition occurring simultaneously, as given by the following equation (1).

$$Y_{total} = Y_{etch} + Y_{dep} \qquad (1)$$

where Y_{total} is the measured apparent etching yield, Y_{etch} is the etching component of yield and Y_{dep} is the deposition component of yield.

Reported activation energies for silicon oxide etching are ranging 0.02 to 0.063 eV[8,22,23] and activation energies for fluorocarbon deposition are –0.31 to –0.35 eV[22]. Since the activation energy for etching is about one order of magnitude smaller than that of deposition, variation of etching component can be neglected with varied temperature from 20°C to –10°C. Therefore, it is assumeed that etching component (Y_{etch}) is relatively independent of temperature, and the variation in measured apparent etch yield is due to the change in deposition component (Y_{dep}).

From equation (1) deposition component of yield is given by

$$Y_{dep} = Y_{total} - Y_{etch} \qquad (2)$$

and the curves are shown in Figure 5.9 (In the figures the measured yield curves are subtracted from the etching components showing 'negative' deposition curves.) These deposition curves

show typical characteristics of sputtering curve, indicating the deposition process is an ion-induced process.

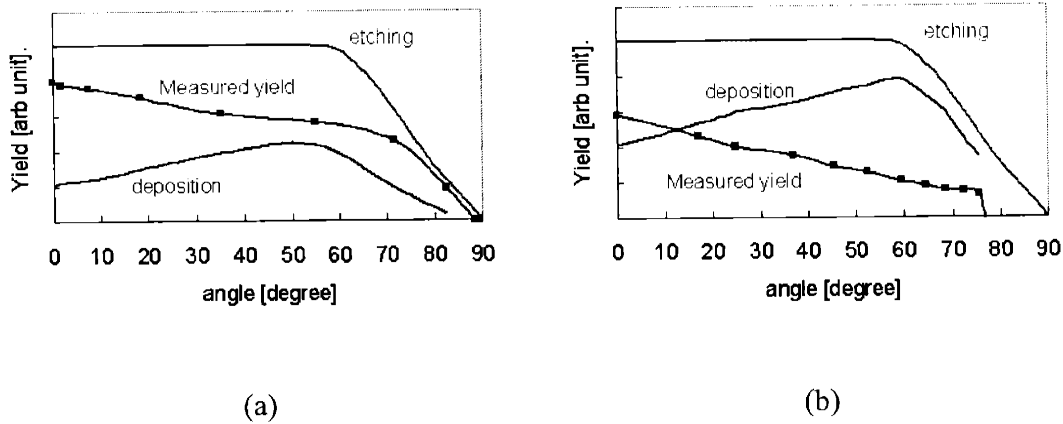

Figure 5.9 Oxide etching yield curves measured at two different temperatures. CHF_3, 5mTorr, 300 eV ion energy, 400 W source power. (a) 20 °C (b) –10°C.

In ion-induced deposition, ions striking the surface deliver kinetic energy to the surface to generate active sites, which react with radicals. The shape of a sputtering curve represents number of atoms ejected from the surface by collision cascade initiated by ion bombardment. Therefore, the amount of energy dissipated at the surface or number of active sites created for deposition should qualitatively have a shape of sputtering process.

As a test, the combination of ion-induced chemical etching and ion-induced deposition is tested to other systems, as shown in Figure 10. For measured SiO_2/Ar^+ etching yield curve and polysilicon/Cl_2 plasma etching yield curve[20] are used for sputtering-shaped deposition component and ion-induced chemical etching component, respectively. The model fits (dotted lines) agree well with measured data (squares and triangles). It is notable that there is only one fitting parameter, which is relative amount of deposition to etching.

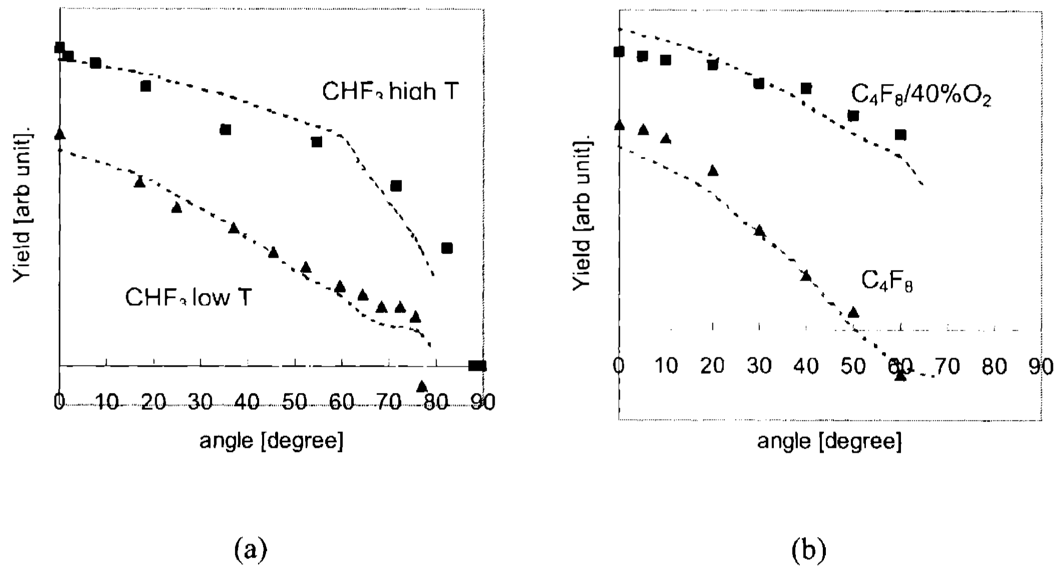

Figure 5.10 Comparison of model fit with measured angular dependent etching yield curve. (a) Temperature variation. (b) Chemistry variation.

5.6 Conclusion

Angular dependence of etching yield of oxide in fluorocarbon plasma shows very unique behavior unlike typical ion-induced chemical etching or physical sputtering. An ion-induced deposition model was suggested and tested. To test the role of deposition in etching feature profile Monte-Carlo simulation was used and it is shown that angular dependence of etching yield curve is a major experimental parameter for determining etching feature profile.

The ion-induced deposition model is consistent with the assumption used in Chapter 3 and Chapter 4.

5.7 References

[1] J. P. Chang, A. P. Mahorowala, and H. H. Sawin, J. Vac. Sci. Technol. A **16** (1), 217 (1998).

[2] R. J. Hoekstra, M. J. Grapperhaus, and M. J. Kushner, J. Vac. Sci. Technol. A **15** (4), 1913 (1997).

[3] Barbara Abraham-Shrauner, J. Vac. Sci. Technol. B **17** (1), 158 (1999).

[4] A. P. Mahorowala and H. H. Sawin, J. Vac. Sci. Technol. B **20** (3), 1064 (2002).

[5] A. P. Mahorowala and H. H. Sawin, J. Vac. Sci. Technol. B **20** (3), 1077 (2002).

[6] A. P. Mahorowala and H. H. Sawin, J. Vac. Sci. Technol. B **20** (3), 1084 (2002).

[7] T. M. Mayer, R. A. Barker, and L. J. Whitman, J. Vac. Sci. Technol **18** (2), 349 (1981).

[8] J. W. Butterbaugh, D. C. Gray, and H. H. Sawin, J. Vac. Sci. Technol. B **9** (3), 1461 (1991).

[9] D. C. Gray, I. Tepermeister, and H. H. Sawin, J. Vac. Sci. Technol. B **11** (4), 1243 (1993).

[10] J. W. Coburn and H. F. Winters, J. Appl. Phys. **50** (5), 3189 (1979).

[11] S. Matsui, T. Yamato, H. Aritome et al., Jpn. J. Appl. Phys. **19** (3), L126 (1980).

[12] A. M. Barklund and H. O. Blom, J. Vac. Sci. Technol. A **11** (4, pt.1), 1226 (1993).

[13] B. O. Cho, S. W. Hwang, G. R. Lee et al., J Vac Sci Technol A **18** (6), 2791 (2000).

[14] D. P. Hamblen and A. Cha Lin, J. Electrochem. Soc **135** (7), 1816 (1988).

[15] C. Hedlund, C. Strandman, I. V. Katardjiev et al., J. Vac. Sci. Technol. B **14** (5), 3239 (1996).

[16] M. Schaepkens, G. S. Oehrlein, C. Hedlund et al., J. Vac. Sci. Technol. A **16** (6), 3281 (1998).

[17] S. A. Vitale, H. Chae, and H. H. Sawin, J Vac Sci Technol A **18** (6), 2770 (2000).

[18] S. A. Vitale, H. Chae, and H. H. Sawin, J. Vac. Sci. Technol. A **19** (5), 2197 (2001).

[19] H. Chae, S. A. Vitale, and H. H. Sawin, J Vac Sci Technol A **21** (2), 381 (2003).

[20] J. P. Chang and H. H. Sawin, J. Vac. Sci. Technol. A **15** (3), 610 (1997).

[21] S. E. Bernacki and B. B. Kosicki, J. Electrochem. Soc **131** (8), 1926 (1984).

[22] Heeyeop Chae, Ph.D., Massachusetts Institute of Technology, 2000.

[23] G. Z. Yin, M. Bendor, M. S. Chang et al., J. Vac. Sci. Technol. A **7** (3), 691 (1989).

Chapter 6. Post Oxide Etching Cleaning

In microelectronic device fabrication processes, plasma processes using fluorocarbon gas mixture are widely used for etching SiO_2. Polymer by-products are formed in this process and play an important role to improve etch selectivity of SiO_2 to Silicon.[1-5] On the other hand, the polymer formation inside contact holes and vias can be detrimental to device performance. Cleaning of this polymer has become increasingly important as dimension of microelectronic device decreases and small amount of contaminants becomes important issue. This work is intended for systematic understanding of integrated post etching gas phase cleaning processes.

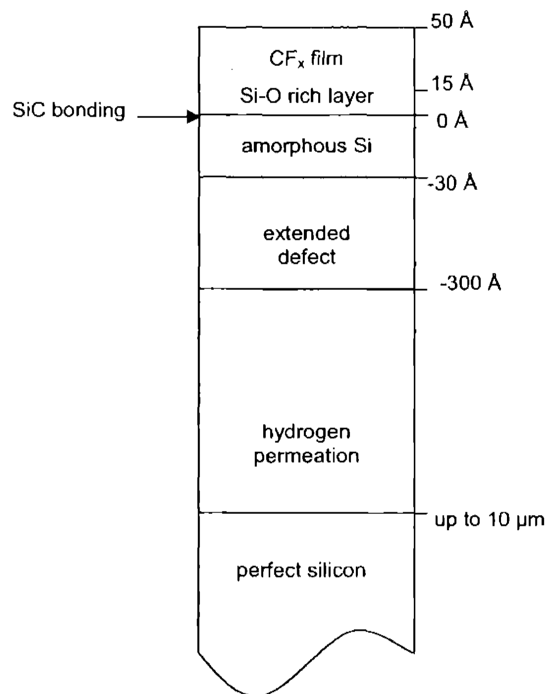

Figure 6.1 A schematic diagram of contamination and damage after a typical plasma etching process

Figure 6.1 shows a schematic diagram of the contamination and damage after a typical oxide etching process. As discussed by many researchers[2,3,6-9], polymer film deposited during plasma oxide etching process using fluorocarbon gases would be Teflon-like. Polymer film formed in etching process plays an important role in enhancing oxide etching selectivity to silicon. Since oxygen is liberated from oxide during etching process to remove polymer film from oxide surfaces, polymer film is deposited preferentially on silicon surface and this hinders silicon etching during the oxide etching process. However, this polymer film has to be removed after oxide etching process because this can increase contact resistance in the contact holes formed by etching process. Coyle *et al.*[10] reported a Si-C layer located at film/silicon interface, while some others such as Thomas *et al.*[11] did not observe it at all.

Many of the literature on plasma etching damage and contamination reported with capacitively-coupled plasma reactor configurations. The contamination and damage induced by inductively-coupled plasma (ICP) sources and other high density plasma sources, however, would be quite similar to damage and contamination in diode type configuration. Many research groups such as Oehrlein *et al.*[2,3,12] ,Yapsir *et al.*[13] reported that similar polymer film was formed in high density plasma etching system, with a lower level of substrate damage.

6.1 Apparatus

6.1.1 Integrated Process Apparatus (VAST tube: VAcuum Sample Transfer tube)

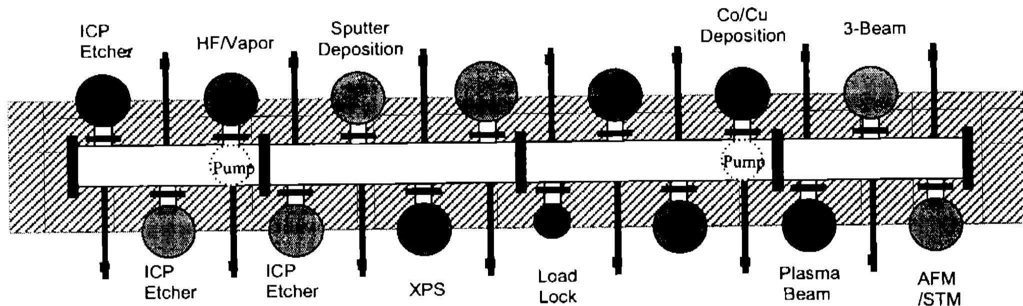

Figure 6.2 A schematic diagram of the Integrated Process Apparatus VAST tube (VAcuum Sample Transfer tube).

Figure 6.2 is a schematic diagram of the integrated processing apparatus. Each processing chamber is connected to the central transfer tube and most of the chambers are capable of processing 4 inch wafers. In the central transfer tube, a cart is installed to transfer samples along the tube. For loading and removing sample from each processing chamber, transfer rods are used. The transfer tube is maintained in the vacuum of low 10^{-8} to mid 10^{-9} torr to minimize contaminations during the transfer. This sample transfer system allows transfer of the sample between chambers in vacuum. The chambers used in this research are ICP etcher, HF vapor cleaning chamber, analytical chamber, and sputtering chamber.

6.1.2 Inductively Coupled Plasma (ICP) Etcher

Figure 6.3 shows a schematic diagram of inductively coupled plasma etcher. In this configuration, RF power at 13.56 MHz for generating plasma is supplied to top coil, which is on 0.5 inch thick quartz window. To reduce capacitive coupling, Teflon spacers are placed between

the coil and the quartz window. A separate power is supplied to the substrate to manipulate ion bombarding energy, which is also 13.56 MHz.

The wafer is cooled by backside cooling water and to enhance thermal contact between the wafer and the electrode electrostatic chuck (ECS) is used with 5 Torr helium backside cooling.

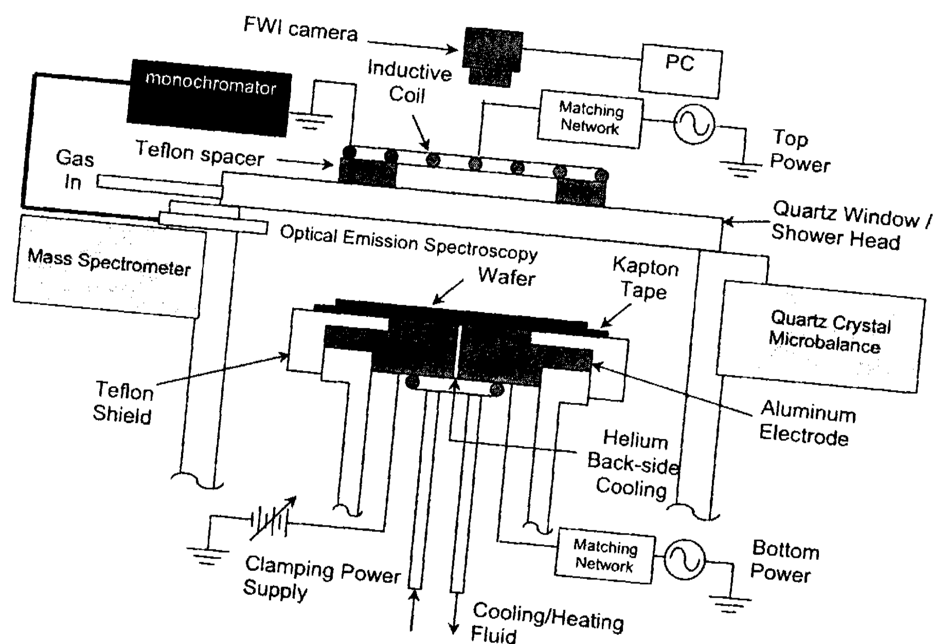

Figure 6.3 A schematic diagram of inductively coupled plasma etcher used in this research

6.1.3 HF Vapor Cleaning Chamber

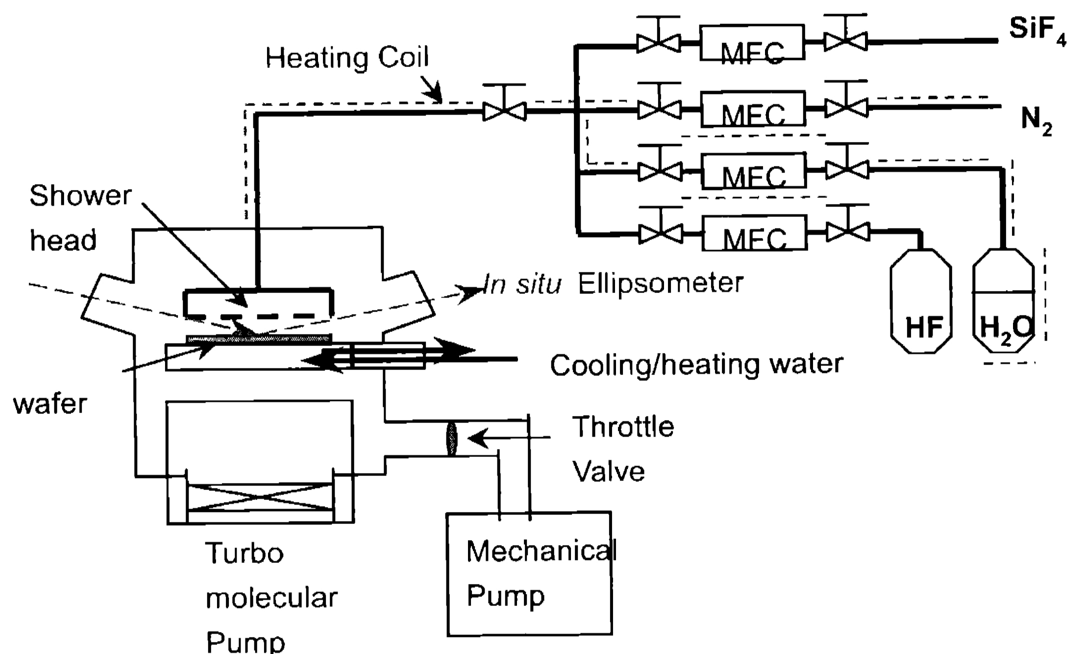

Figure 6.4 A schematic diagram of HF vapor cleaning apparatus.

The HF/Vapor chamber is configured to accept 4 inch wafers or smaller samples. Anhydrous HF and heated water as well as other additive gases such as nitrogen are delivered through stainless steel gas lines. All the gas lines as well as the chamber wall are heated to prevent condensation during gas delivery. Wafer temperature is separately controlled by heating/cooling fluid, which can be varied from room temperature to 150 °C.

The gas mixture flows through a showerhead and is distributed over the wafer. Process gas is exhausted with a mechanical pump through a liquid nitrogen trap. The base pressure of the chamber is in the order of 10^{-7} torr.

Figure 6.4 schematically shows HF vapor cleaning chamber.

6.2 Experimental Procedure

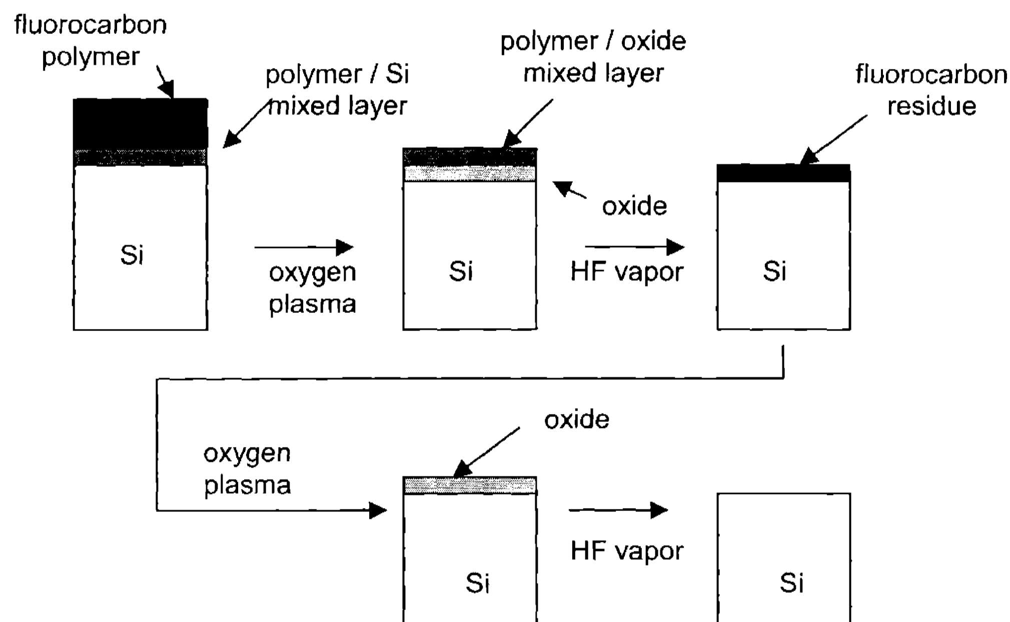

Figure 6.5 A schematic diagram of contaminated/damaged films and the removal procedure.

Figure 6.5 shows a schematic diagram of the contaminated films and the removal procedure. After etching the contaminating film consists of a layer of bulk fluorocarbon polymer approaching up to 50 Å in thickness, atop relatively "clean" silicon. At the interface between the polymer and silicon is a transition region of mixed composition, 5-10 Å in thickness. First oxygen plasma cleaning / ashing removes virtually all of the bulk fluorocarbon film, such that most of the remaining polymer was in a mixed fluorocarbon polymer/oxide environment. First HF cleaning strips oxide off leaving polymer or polymer-like residue on the surface. Another cycle of oxygen plasma and HF vapor cleaning removes the remaining contamination to obtain a clean silicon surface. Since oxygen plasma forms plasma induced oxide and HF vapor strips it off, about 20 Å of damaged silicon layer is removed as well as fluorocarbon contamination.

6.2.1 Etching

100% CHF_3 is used for etching gas with 10 sccm flow rate. 5500 Å of thermally grown silicon oxide is used for etching. To build up sufficient amount of polymer 50% over etch is performed. RF power of 175 W is supplied to top coil and 100W of bottom power is used. 1.2 kV of DC is applied for the electrostatic chuck. The etching rate is 1500 to 2000 Å/min.

6.2.2 Oxygen Plasma Cleaning

100% oxygen is used for 1st and 2nd oxygen plasma process. Flow rate is 20 sccm and operating pressure is 40 mTorr. RF power of 200 W is used without bottom RF bias. Processing time is 3 minutes.

6.2.3 HF Vapor Cleaning

HF process used in this research has been developed by Yong-Pil Han[14]. Figure 6.6 shows the two regimes of HF vapor etching process. In non-condensation regime, the etch rate is in the order of 10s of Å/min, which is two orders of magnitude lower than in condensation regime. By using this process, we can remove the contaminated oxide. The conditions used in this study are as follows: 90°C for sample temperature, 125 torr for processing pressure, flow rate of 80 sccm for HF, 32 sccm for H_2O, 388 sccm for N_2. The etch rate under this condition is 8 Å/min and the processing time is 1 minute, which etches 80 Å of oxide.

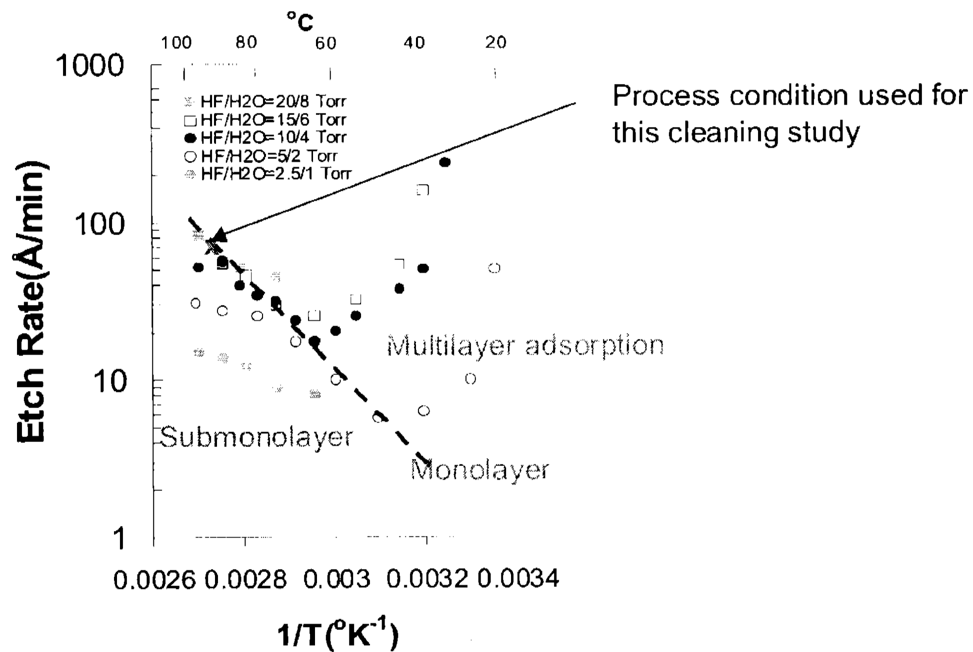

Figure 6.6 Condensation and non-condensation regimes in HF vapor etching[14].

6.2.4 Sputter Cleaning

Prior to metal deposition, sputter cleaning is usually done to form a good electrical contact. To simulate the real process conditions, sputter cleaning is performed after finishing second HF vapor cleaning process. It is done at 20 mTorr 100% Ar with 40 W RF power to the wafer for 1 minute.

6.2.5 XPS Analysis

Al K_{α} is used for X-ray source. Pass energy is 20 V, and number of scans for each element is 50. Take-off angle, which is the angle between detector and the sample, is fixed to 90 degree. The steady state charge shift is corrected by setting metallic silicon 1s peak to 99.15 eV.

Number of monolayer analysis was made as follows.

With the thickness of contamination layer is d and electron escape depth of the contaminated layer is λ_1, the Si peak intensity from the contaminated sample is

$$I = I_o \exp(-\frac{d}{\lambda_1}) \quad (1)$$

where I is Si XPS peak intensity from the contaminated film and I_0 is Si XPS peak intensity from the clean sample. By comparing I and I_0, we can know d and number of monolayers N is given by

$$N = \frac{d}{d_m} \quad (2)$$

where d_m is monolayer thickness.

Electron escape depth values used in this work is 35 Å for Si and SiO_2 and 15 Å for polymeric contamination[15].

To investigate contamination on trench bottoms and sidewalls, angle-resolved XPS is used. Figure 6.7 is a schematic diagram illustrating angle-resolved XPS technique.

To see the contamination on trench bottom and top of patterned line the electron detector (analyzer) is placed at 90-degree take-off angle and 25 take-off angle is used to see contamination on sidewalls. Line width used is 1.0 μm and pitch is 2.0 μm with 5500 Å of oxide thickness.

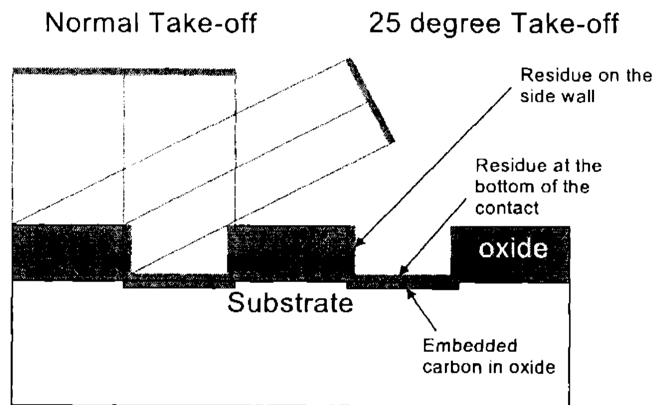

Figure 6.7 A Schematic diagram of angle resolved XPS showing normal take-off angle and 25-degree take-off angle

6.2.6 Contact Resistance Measurement

To measure contact resistance, contact chain structure is as shown in Figure 6.8. A contact chain consists of 50 contacts. An applied potential across the contact chain of 3 V is used in all measurements corresponding to 60 mV per contact. Measurement is performed for both 1.0 and 1.5 μm size contacts. Boron doped n^+ well has a sheet resistance of 5 Ω/sq and the surface doping concentration is $5x10^{19}$ cm^{-3}. Oxide thickness is 5500 Å.

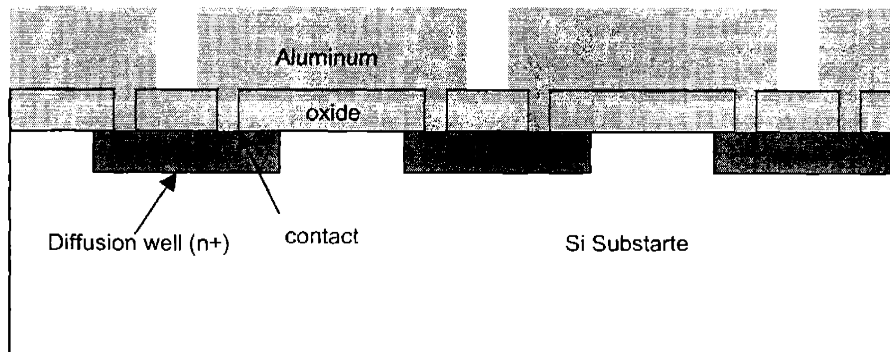

Figure 6.8 Contact chain structure used for measuring contact resistance

6.3 RESULTS AND DISCUSSION

6.3.1 Cleaning Planer Silicon Surface

Figure 6.9 shows amount of contamination left on the silicon surface after each process step. After oxide etching using fluorocarbon plasma, there is approximately 25 Å of fluorocarbon deposition on silicon surface based on the calculation using equation (1). Taking 5 Å as the monolayer thickness, 25 Å corresponds to approximately 5 monolayers.

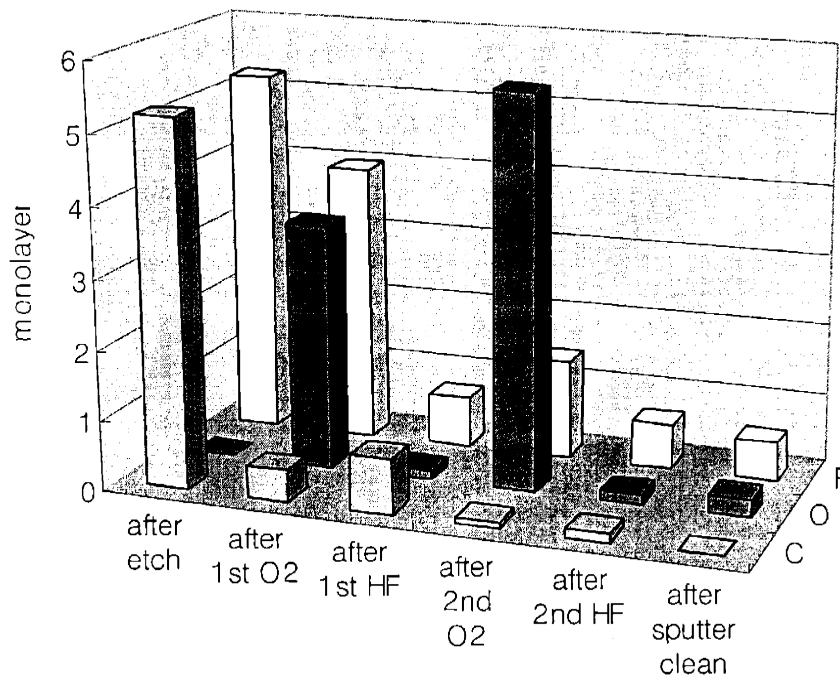

Figure 6.9 A histogram showing amount of carbon, oxygen and fluorine contamination left on the surface after each process step.

First oxygen plasma treatment or ashing process removes carbon contamination from the surface leaving only 0.46 monolayer of carbon coverage on the surface. Oxygen contamination peak, however, becomes large because of plasma-induced oxide is formed.

First HF vapor cleaning removes the plasma-induced oxide leaving less than 0.1 monolayer of oxygen on the surface. Carbon contamination increases after stripping oxide because carbon contamination that has been imbedded in the oxide is now revealed although the carbon contamination is still less than one monolayer.

After second oxygen plasma treatment, there is only 0.1 monolayer coverage of carbon contamination with approximately five monolayers of oxygen due to plasma induced oxidation.

Second HF vapor cleaning again removes plasma-induced oxide from the surface leaving approximately 0.1 monolayer for both carbon and oxygen while fluorine contamination level is approximately 0.5 monolayer.

After sputter cleaning, which is commonly done right before metal deposition, carbon is removed to XPS detection limit while oxygen and fluorine contamination is still detected. The submonolayer coverage of oxygen and fluorine is attributed primarily to the transfer procedure. Even at 1×10^{-8} torr, where sample transfers are performed monolayer formation time is about 100 seconds assuming sticking probability is unity, and sample transfer time is typically 5 minutes.

6.3.2 Cleaning Line and Space Structure

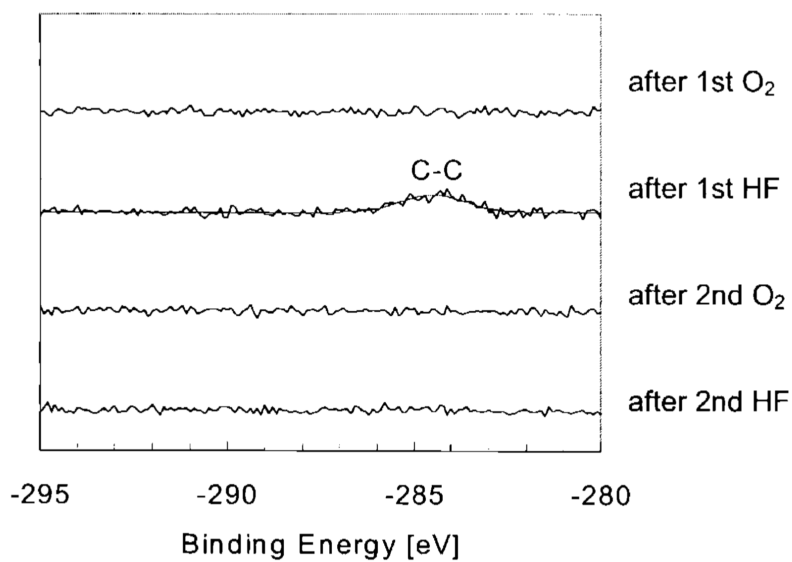

(a)

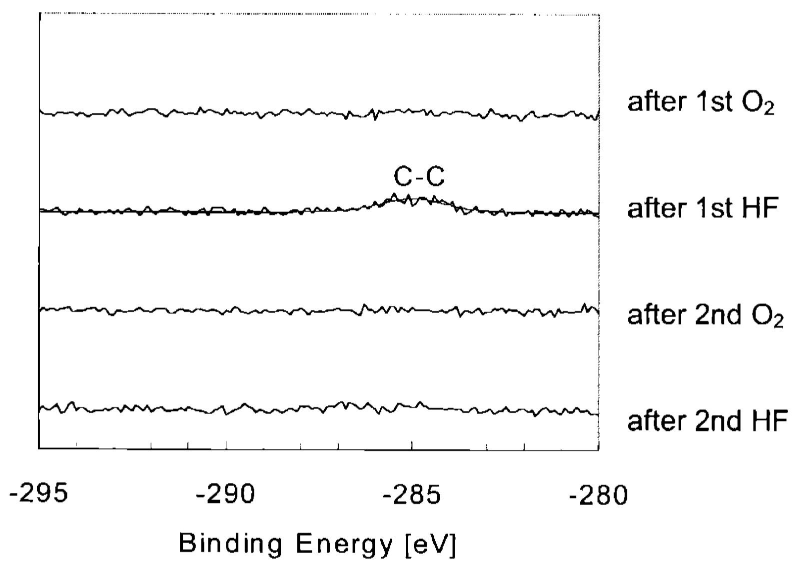

(b)

Figure 6.10 XPS spectra showing carbon contamination on the surface after each processing step. (a) Normal take-off angle. (b) 25 degree take-off angle.

The integrated cleaning process is also applied to line and space structure to show its capability of cleaning vertical sidewalls as well as bottom of the feature.

Figure 6.10 shows XPS signal after each processing step with normal take-off angle as well as 25-degree take-off angle. At normal take-off angle, the XPS signal is from the top of the line and the bottom of the feature, while at 25-degree take-off angle, the signal is from the top of the feature and the sidewall.

After ashing the carbon contamination is removed from the surface by the oxygen plasma. After first HF cleaning, very small amount of carbon (< monolayer) is revealed which has been imbedded in the oxide because HF vapor removes oxide from the surface. This small amount of carbon contamination, however, is completely removed from the surface with another cycle from the bottom as well as sidewall of the feature.

6.3.3 Contact Resistance Measurement

Figure 6.11 and Figure 6.12 show electrical contact resistance measurements for chains of 50 contacts in series, which are for 1.0 micron contacts and 1.5 micron contacts, respectively. The resistance values shown are for 50 contacts. In both cases, 'after ash' resistances are very high, which are 2,500 KΩ per 50 contacts for the contact chains where currents are measurable. About 1/3 of the chains shows infinite resistances. This is due to the presence of plasma-induced oxide on the silicon surface of which thickness is about 20-30 Å mixed with fluorocarbon compounds. Because of the variability of this plasma grown oxide, the standard deviation of the resistance is also very high, which is up to 3,000 KΩ.

After the first HF cycle of the process, however, the resistance drops significantly to 3.45 KΩ and 2.63 KΩ for 1.0 μm contacts and 1.5 μm contacts, respectively. This is due to the removal of fluorocarbon-contaminated oxide from the surface as shown in Figure 6.5.

Repetition of the cleaning cycle slightly reduces resistance to show 3.34 KΩ and 2.49 KΩ for 1.0 μm and 1.5 μm contacts, respectively. It is, however, difficult to confirm that repetition of the process cycle definitely reduces contact resistance because of relatively large standard deviation. Sputter cleaning process reduces these values further to 2.43 KΩ and 1.83 KΩ. It is notable that after sputter cleaning the measurement shows smaller deviation. This reduction could in part be due to the reduction in contamination in the transfer process.

The contact chain resistance of the 25 diffusion wells (one diffusion well / two contact holes) is computed to be a minimum of 1.25 KΩ using the sheet resistance of the wells and their dimensions. Contact current spreading resistance that increases the expected value of the chain resistance has not been added. And 'ideal' contact resistance for n^+ to Al is 10Ω-μm^2 for the surface doping concentration of $5x10^{19}cm^{-3}$, which yields an expected 'ideal' contact resistance of 0.50 KΩ for 1.0 μm contact chain and 0.22 KΩ for 1.5 μm contact chain[16]. Based on these simple calculations, the 'ideal' expected resistance values (ignoring current spreading at the contact) are 1.75 KΩ for 1.0 μm contact chains and 1.47 KΩ for 1.5 μm contact chains.

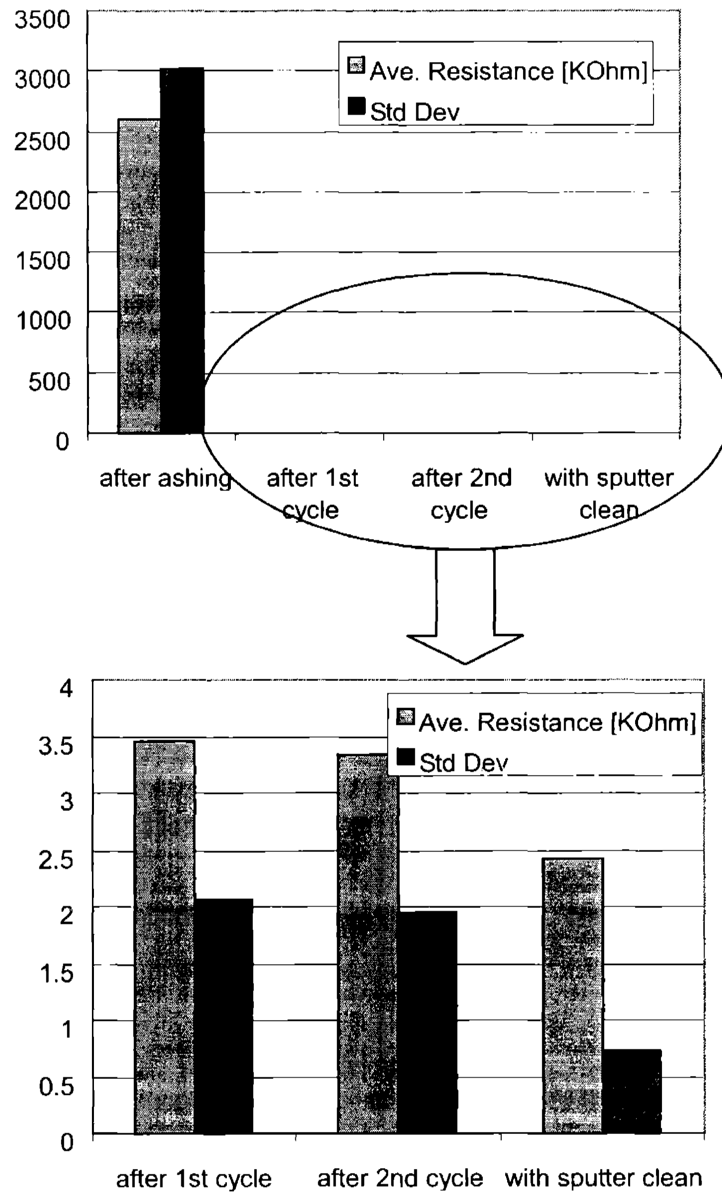

Figure 6.11 Contact resistance and standard deviation for a chain of 50 contacts with 1.0 μm contact size. The contact resistance values shown are for 50 contacts. The chain measurement voltage was 3 V. The minimum expected contact chain resistance assuming 'ideal' contacts is 1.75 kΩ.

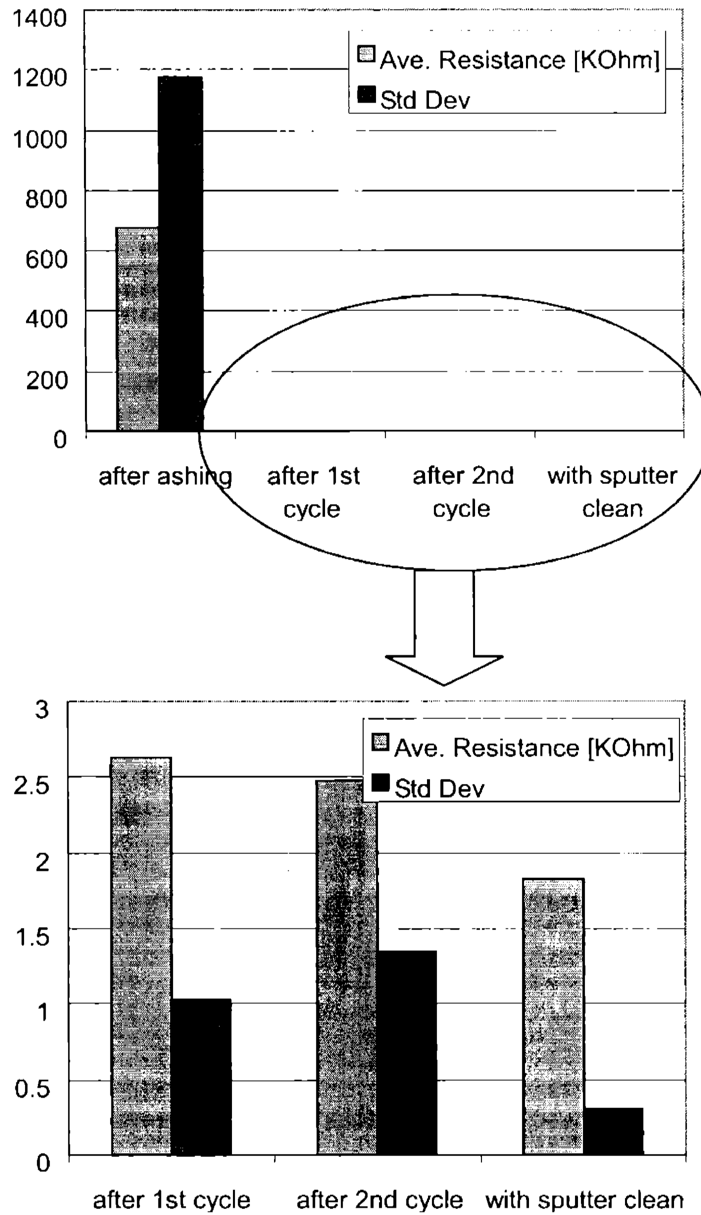

Figure 6.12 Contact resistance and standard deviation for a chain of 50 contacts with 1.5 μm contact size. The contact resistance values shown are for 50 contacts. The chain measurement voltage was 3 V. The minimum expected contact chain resistance assuming 'ideal' contacts is 1.47 kΩ.

The measured contact chain values of 2.43 KΩ and 1.83 KΩ approach the expected values of 1.75 KΩ for 1.0 μm contact chains and 1.47 KΩ for 1.5 μm contact chains. No opens are observed in any measurements of the contact chains after HF vapor cleaning. The variability of the contact chain is comparable to the chain resistance, but is reduced greatly by sputter cleaning of the contacts in the sputter deposition chamber.

6.4 Conclusion

Experiments on integrated post oxide etch cleaning process have been performed, with oxygen plasma cleaning process and HF vapor cleaning process with blanket oxide films. The results indicate that polymeric contamination, which is formed during oxide etching process, can be removed by using oxygen plasma - HF vapor - oxygen plasma - HF vapor process sequence. The integrated process effectively removes the polymeric contamination formed under high ion energy etching condition and under low ion energy etching condition. Measured contact resistance values after cleaning sequence is close to theoretical minimum.

6.5 References

1. J. W. Coburn, J. Appl. Phys. **50** (8), 5210 (1979).
2. G. S. Oehrlein, Y. Zhang, D. Vender et al., J. Vac. Sci. Technol. A **12** (2), 323 (1994).
3. G. S. Oehrlein, Y. Zhang, D. Vender et al., J. Vac. Sci. Technol. A **12** (2), 333 (1994).
4. Y. Wang, S. W. Graham, L. Chan et al., J. Electrochem. Soc **144** (4), 1522 (1997).
5. H. Shan, B. K. Srinivasan, D. W. Jillie et al., J. Electrochem. Soc **141** (10), 2904 (1994).
6. O. Joubert, G. S. Oehrlein, and M. Surendra, J. Vac. Sci. Technol. A **12** (3), 665 (1994).

[7] O. Joubert, G. S. Oehrlein, and Y. Zhang, J. Vac. Sci. Technol. A **12** (3), 658 (1994).

[8] T. Ono, R. Hamasaki, and T. Mizutani, Jpn. J. Appl. Phys. Pt 2 **33** (12A), L1717 (1994).

[9] J. W. Coburn, J. Vac. Sci. Technol. A **12** (4), 1417 (1994).

[10] G. J. Coyle and G. S. Oehrlein, Appl. Phys. Lett. **47** (6), 604 (1985).

[11] J. H. Thomas, X. C. Mu, and S. J. Fonash, J. Electrochem. Soc **134** (12), 3122 (1987).

[12] G. S. Oehrlein, J. Vac. Sci. Technol. A **11** (1), 34 (1993).

[13] A. S. Yapsir, G. Fortunowiltshire, J. P. Gambino et al., J. Vac. Sci. Technol. A **8** (3), 2939 (1990).

[14] Y-P. Han, Ph.D. thesis, Massachusetts Institute of Technology, 1999.

[15] G.E. Muilenberg, *Handbook of X-ray Photoelectron Spectroscopy.* (Perkin-Elmer Corporation, Eden Prairie, MN, 1979).

[16] H. H. Berger, J. Electrochem. Soc **119** (4), 507 (1972).

Chapter 7. Conclusion

7.1 Summary of the work

We have measured etching yield and gas composition for C_2F_6 and C_4F_8 + 80% Ar varying RF coil power and pressure. In C_2F_6 plasma, concentration of atomic fluorine in the neutral flux was 5-25% while there was less than 0.5% of atomic fluorine in C_4F_8 + 80% Ar plasma. A surface plot representing etching yield as a function of incoming fluxes was constructed and using the surface plot etching yield behaviors were qualitatively explained using the surface plot.

In C_2F_6 chemistry, etching yield decreased slightly with increasing because both of F/ion and CF_x/ion decreased caused by increase in ion flux with more significant effect of decrease in F/ion. In C_4F_8 + 80% Ar chemistry, however, etching yield increased with increasing RF coil power due to decrease in CF_x without the effect of F/ion because of low atomic fluorine concentration.

With increasing operating pressure, etching yield decreased for both chemistries because as the pressure increases ion current decreased and CF_x neutral increased to have more deposition and less etching.

This measurement and analysis give a good insight about the relationship between gas composition and etching yield during the etching process. The measured data can also be used for other simulations, as was done in the work described in Chapter 3.

A novel surface kinetic model using translating mixed-layer representation is proposed

and demonstrated.

In this model, a translating mixed-layer is constructed where total number of atoms is conserved as the etching proceeds, to have a convection or movement flux from or to the substrate volume which corresponds to the difference between the adsorption flux and removal flux.

The model is demonstrated for silicon etching with chlorine chemistry and silicon oxide etching with fluorine chemistry showing that the results agree well with measured data as well as previously developed Monte-Carlo simulation result. The computation speed of the moving boundary layer model was 100 to 10000 times faster than that of Monte-Carlo simulation.

This is the first to use a 'mixed layer' for modeling etching process. Using this technique, adequate surface kinetics models can be developed rapidly, which is necessary for feature profile simulation, especially for complex systems such as oxide etching with fluorocarbon plasmas.

Oxide etching has been modeled using a translating mixed-layer model. Using the new modeling approach, oxide etching with fluorocarbon chemistry was successfully modeled. Carbon and fluorine were identified as primarily contributor to deposition and etching, respectively.

Atomic fluorine flux is a major factor to determine the etching behavior. With a chemistry with small amount of atomic fluorine such as C_4F_8 chemistry, etching yield showed stronger dependence on composition change in the gas flux.

Based on the simulation result, a new oxide etching model is suggested. In the new model, adsorbed species act as etchants, where in the previous model, atomic fluorine is the major etchant. The etching yield is controlled by the composition of the mixed layer, which has a strong dependence on incoming atomic flux.

Angular dependence of etching yield of oxide in fluorocarbon plasma shows very unique behavior unlike typical ion-induced chemical etching or physical sputtering. It was ion-induced deposition model is suggested and tested. To test the role of deposition in etching feature profile Monte-Carlo simulation is used and it is shown that angular dependence of etching yield curve is a major experimental parameter for determining etching feature profile.

This measurement and analysis gives a useful basis and insight that can be embedded in a feature profile simulator.

Experiments on integrated post oxide etch cleaning process have been performed, with oxygen plasma cleaning process and HF vapor cleaning process with blanket oxide films. The results indicate that polymeric contamination, which is formed during oxide etching process, can be removed by using oxygen plasma - HF vapor - oxygen plasma - HF vapor process sequence. The integrated process worked very well to remove polymeric contamination formed under high ion energy etching condition and under low ion energy etching condition. Measured contact resistance values after cleaning sequence was close to theoretical minimum.

7.2 Future Work

To obtain a better set of kinetic parameters of the surface kinetic model, it is desired to conduct more statistical regression with more data collection. To do this, the ABACUSS II code may be imbedded into a C++ or FORTRAN code. This can be also done by making a package of code to solve the differential equations without using ABASUSS II.

Extensive work on the precise calibration of mass spectrometer and measurement of neutral and ion composition should be done in a broader parameter space to have a good statistical sampling. Other fluorocarbon gases may be also investigated, which would provide with data with broader parameter space.

The kinetic model with the kinetic parameters obtained provides a useful basis that can be used in a feature profile simulator. Converting kinetic parameters into probability of reactions and using the set of reactions that has been proven to be an adequate set to represent the surface kinetics, the result of this result can be utilized in a Monte-Carlo feature profile simulator. For simpler etching systems such as silicon etching with chlorine chemistry, developing a proper surface kinetic model may not be necessary because the surface reaction is very simple. For more complex systems, however, feature profile simulator cannot be built without a adequate surface kinetics model.

Ion induced chemical etching reaction rates (β) and sputtering yield coefficients (Y_i) are known to have energy dependence and energy dependence of the kinetic parameters also needs to be investigated. In this study, only one ion energy was used for each modeling. This work also needs more experimental measurement with different ion energy.

The angular dependence of oxide etching yield measurement presented in Chapter 5 should be incorporated into a feature profile simulator to conduct more accurate simulation.

Appendix. ABACUSS II code

A.1 Silicon Etching with Chlorine Chemistry

```
DECLARE

  TYPE
    # identifier         # default  # lower  # upper
    Concentration =               1.0    :  -1E-12   : 1E5
    Rate         =            0.0    :  -1E-4    : 1E9
    Yield        =         0.0    :  -1E9     : 1E9

END # DECLARE block
#10

MODEL Etch

  PARAMETER
    S1         AS REAL
    S2         AS REAL

    B          AS REAL

    Y_Si       AS REAL       #20
    Y_Cl       AS REAL

    R_Cl       AS REAL
    R_Cl_i     AS REAL

  VARIABLE
    X_Si , X_Cl                                 AS Concentration
    R1, R2, R3, R4, R5                      AS Rate
    Y                                       AS Yield
#30
  EQUATION
```

```
    R1 = S1 * R_Cl * (X_Si - 0.5*X_Cl) ;

    R2 = S2 * R_Cl_i * (X_Si - 0.5*X_Cl) ;

    R3 = B * X_Cl ;

    R4 = Y_Si * X_Si ;

    R5 = Y_Cl * X_Cl ;      #40

    Y = -R1 - R2 + 3*R3 + R4 + R5 ;

    $X_Si = -R1 - R2 + 2*R3 + R5 ;

    $X_Cl = R1 + R2 - 2*R3 - R5 ;

END #  MODEL block!!

#50
SIMULATION Etch_Simul   # identifier for future reference

  OPTIONS
    DYNPRINTLEVEL := 1 ;
    DYNATOLERANCE := 1.0e-5 ;
    DYNRTOLERANCE := 1.0e-5 ;

    DATAOUTPUT := TRUE ;
    CSVOUTPUT := TRUE ;
#60
  UNIT
    Etch       AS Etch

  SET
    WITHIN Etch DO
      S1 := 0.3 ;
      S2 := 1.0 ;
```

```
    B := 5.0 ;
    Y_Cl := 0.0 ; #ignoring Cl sputtering
    Y_Si := 0.07 ; #70
    R_Cl := 500     ;
    R_Cl_i := 0 ; # all the ions are Ar+
  END # within structure

PRESET
  WITHIN Etch DO
    # identifier      # default # lower # upper
    X_Si           :=     1.0   :  0.0  : 1.0 ;
    X_Cl           :=     0.0   :  0.0  : 1.0 ;
  END # within structure #80

INITIAL
  WITHIN Etch DO
    X_Si = 1.0 ;
    X_Cl = 0.0 ;
  END # within structure

SCHEDULE
  SEQUENCE
    CONTINUE FOR 1.0      #90
    EXPORT
      Etch.X_Si,
      Etch.X_Cl,
      Etch.Y
    END #export
  END #sequence

END # simulation
```

A.2 Silicon Oxide Etching with Fluorine Chemistry

```
DECLARE

  TYPE
   # identifier     # default  # lower  # upper
   Concentration =  1.0    :  -1E-12   : 1
   Reaction_Rate =     0.0    :  -1E2   : 1E9
   Yield       =          0.0       :  -1e9     : 1e9

END # DECLARE block
# 10

MODEL Etch

  PARAMETER
   S1         AS REAL       # Cl on Si
   S2         AS REAL       # Cl on O
   S3         AS REAL       # Cl+ on Si
   S4         AS REAL       # Cl+ on O

   B1         AS REAL       # for etching reaction # 20
   B2         AS REAL

   Y_Si       AS REAL       # sputtering yield for Si
   Y_O        AS REAL       # sputtering yield for O
   Y_F        AS REAL       # sputtering yield for F

   R_F        AS REAL       # flux of F(g) / total flux of ions
   R_F_i      AS REAL       # flux of F+ / total flux of ions


  VARIABLE    #30
   X_Si       AS Concentration     # Concentration of Si
   X_O        AS Concentration     # Concentration of O
```

```
X_F        AS Concentration     # Concentration of F

R1         AS Reaction_Rate
R2         AS Reaction_Rate
R3         AS Reaction_Rate
R4         AS Reaction_Rate
R5         AS Reaction_Rate
R6         AS Reaction_Rate     #40
R7         AS Reaction_Rate
R8         As Reaction_Rate
R9         AS Reaction_Rate
R10        AS Yield
Yield      AS Yield


EQUATION   #50

R1 = S1 * R_F * (X_Si - 0.5 * X_F * 2*X_Si / (2*X_Si + X_O)) ;

R2 = S2 * R_F * (X_O -  1.0* X_F * X_O/(2*X_Si+X_O))  ;

R3 = S3 * R_F_i * (X_Si - 0.5 * X_F * 2*X_Si / (2*X_Si + X_O)) ;

R4 = S4 * R_F_i * (X_O -  1.0* X_F * X_O/(2*X_Si+X_O)) ;

R5 = B1 * X_F * X_Si / (X_Si + X_O) ;      #60

R6 = B2 * X_F * X_O / (X_Si + X_O) ;

R7 = Y_Si * X_Si ;

R8 = Y_O * X_O ;

R9 = Y_F * X_F ;

R10 = (1/3) * (-R1 - R2 - R3 - R4 + 3*R5 + 2*R6 + R7 + R8 + R9) ;
```

```
    Yield = 3*R10 ;

    $X_Si = -R5 - R7 + R10 ;       #70

    $X_O = -R6 - R8 + 2*R10 ;

    $X_F = R1 + R2 + R3 + R4 - 2*R5 - R6 - R9 ;

    #  Concentration_Si + Concentration_O + Concentration_F = 1.0 ;

END # MODEL block

#80
SIMULATION Etch_Simul

  OPTIONS
    DYNPRINTLEVEL := 1 ;
    DYNATOLERANCE := 1.0e-5 ;
    DYNRTOLERANCE := 1.0e-5 ;

  UNIT
    Etch      AS Etch  # Reactor is an instance of MODEL type Etching
#90
  SET
    WITHIN Etch DO
      R_F       := 20 ;              # neutral to ion flux ratio is 100
      R_F_i     := 0 ;               # all ions are Ar+

      S1        := 0.04 ;
      S2        := 0.04 ;
      S3        := 1.0 ;             # sticking coefficient of ions are unity
      S4        := 1.0 ;             # sticking coefficient of ions are unity
      B1        := 1.3 ;
      B2        := 1.3 ;
      Y_Si      := 0.2 ;
```

```
    Y_O      := 0.2 ;
    Y_F      := 0.2 ;      #100
  END # within structure

 PRESET
  WITHIN Etch DO
                  # default    # lower      # upper
    X_Si    :=     0.33 :       0.0 :        1.0 ;
    X_O     :=     0.67 :       0.0 :        1.0 ;
    X_F     :=     0.00  :      -1e-5 :              1.0 ;

  END # within structure # 110

 INITIAL
  WITHIN Etch DO
    X_Si = 0.33 ;
    X_O = 0.67 ;
    X_F = 0.0 ;
  END

 SCHEDULE
  SEQUENCE
    CONTINUE FOR 1000.0
#129
    EXPORT
      #Etch.X_Si
      Etch.X_O
      Etch.X_F
      Etch.R1
      Etch.R2
      Etch.Yield   #80
    END #export
  END #sequence

END # SIMULATION block
```

A.3 Silicon Oxide Etching with Fluorocarbon Chemistry

```
# SiF2, SiF4, O2, F2, CO as etching products
# CF4 production (thermal etching) - proportional to F flux
# 3F per C, 3C per C, 1C per O, 2F per Si
```

data set used is for C_2F_6, 5mTorr, 300 W coil power, 300eV bias

```
DECLARE

  TYPE
    # identifier          # default  # lower  # upper
    Concentration =          1.0    :  -0.1   : 1.0    UNIT = "concentration"
    Reaction_Rate      =     0.0    :  -1E99    : 1E99    UNIT =
"concentration/ion"
    Yield              =              0       :      -1e99  :      1e99           UNIT
= "concentration/ion"
    E_Conc             =              0.0     :      -0.1   : 1.01

END


MODEL Series_Reactions

PARAMETER

  S_F_on_Si          AS REAL
  S_F_on_C           AS REAL
  S_CF_on_O          AS REAL
  S_CF_on_C          AS REAL
  S_CF2_on_O         AS REAL
  S_CF2_on_C         AS REAL
  S_CF3_on_O         AS REAL
  S_CF3_on_C         AS REAL
  S_C2F3_on_O        AS REAL
```

```
S_C2F3_on_C        AS REAL
S_C2F4_on_O        AS REAL
S_C2F4_on_C        AS REAL
S_C2F5_on_O        AS REAL
S_C2F5_on_C        AS REAL
S_C3F3_on_O        AS REAL
S_C3F3_on_C        AS REAL
S_C3F5_on_O        AS REAL
S_C3F5_on_C        AS REAL

S_F_i              AS REAL
S_CF_i             AS REAL
S_CF2_i            AS REAL
S_CF3_i            AS REAL
S_C2F3_i           AS REAL
S_C2F4_i           AS REAL
S_C2F5_i           AS REAL
S_C3F3_i           AS REAL
S_C3F5_i           AS REAL

B_SiF2             AS REAL
B_SiF4             AS REAL
B_CO               AS REAL
B_CO2              AS REAL
B_COF              AS REAL
B_CF               AS REAL
B_O                AS REAL
B_F                AS REAL
A_CF               AS REAL

Y_Si               AS REAL
Y_O                AS REAL
Y_C                AS REAL
Y_F                AS REAL

R_F                AS REAL
```

```
  R_CF                  AS REAL
  R_CF2                 AS REAL
  R_CF3                 AS REAL
  R_C2F3                AS REAL
  R_C2F4                AS REAL
  R_C2F5                AS REAL
  R_C3F3                AS REAL
  R_C3F5                AS REAL
  R_F_i                 AS REAL
  R_CF_i                AS REAL
  R_CF2_i               AS REAL
  R_CF3_i               AS REAL
  R_C2F3_i              AS REAL
  R_C2F4_i              AS REAL
  R_C2F5_i              AS REAL
  R_C3F3_i              AS REAL
  R_C3F5_i              AS REAL
  R_Ar_i                AS REAL

  N2I                   AS REAL

VARIABLE

  X_Si AS Concentration
  X_O  AS Concentration
  X_C  AS Concentration
  X_F  AS Concentration

  X_Si_F        AS E_Conc
  X_C_F         AS E_Conc
  X_O_C         AS E_Conc
  X_C_C         AS E_Conc

  RA1, RA2, RA3, RA4, RA5, RA6, RA7, RA8, RA9, RA10   AS Reaction_Rate
  RA11, RA12, RA13, RA14, RA15, RA16, RA17, RA18, RA19, RA20       AS
Reaction_Rate
```

```
 RA21, RA22, RA23, RA24, RA25, RA26, RA27     AS Reaction_Rate

 RE1, RE2, RE3, RE4, RE5, RE6    AS Reaction_Rate
 RE7, RE8                        AS Reaction_Rate

 RS1, RS2, RS3, RS4              AS Reaction_Rate

 RF, RCF, RCF2, RCF3, RC2F3, RC2F4, RC2F5,  RC3F3, RC3F5          AS
Reaction_Rate
 RY1, RY_AD, RY_E                             AS Reaction_Rate

 Rion                                         AS Reaction_Rate
#  R_N2I
                          AS Reaction_Rate

#  F_Si, C_Si, F_C               AS Reaction_Rate

SET

EQUATION

#     X_Si_F = X_Si;

#     X_C_F = X_C;

#     X_O_C = X_O;

#     X_C_C = X_C;


#     X_Si_F = X_Si - 0.5*X_F * X_Si / (X_Si + X_C) ;

#     X_C_F = X_C - 0.5*X_F * X_C / (X_Si + X_C) ;

#     X_O_C = X_O - X_C * X_O / (X_O + X_C) ;
```

```
#     X_C_C = X_C;


    X_Si_F = X_Si - (1/2)*X_F * 2*X_Si / (2*X_Si + 3*X_C) ;

    X_C_F = X_C - (1/3)*X_F * 3*X_C / (2*X_Si + 3*X_C) ;

    X_O_C = X_O - 3*X_C * X_O / (3*X_C + X_O + X_F) ;

    X_C_C = X_C - (1/3)*3*X_C * 3*X_C / (3*X_C + X_O + X_F);


  Rion = R_F_i + R_CF_i + R_CF2_i + R_CF3_i + R_C2F3_i + R_C2F4_i + R_C2F5_i +
R_C3F3_i + R_C3F5_i + R_Ar_i ;

# R_N2I = (RF + RCF + RCF2 + RCF3 + RC2F3 + RC2F4 + RC2F5 + RC3F3 +
RC3F5)/Rion ;


  RF = RA1 + RA2 + RA3 ;

  RCF = RA4 + RA5 + RA6 ;

  RCF2 = RA7 + RA8 + RA9 ;

  RCF3 = RA10 + RA11 + RA12 ;

  RC2F3 = RA13 + RA14 + RA15 ;

  RC2F4 = RA16 + RA17 + RA18 ;

  RC2F5 = RA19 + RA20 + RA21 ;

  RC3F3 = RA22 + RA23 + RA24 ;
```

```
RC3F5 = RA25 + RA26 + RA27 ;


RA1 = S_F_on_Si * R_F * X_Si_F ;

RA2 = S_F_on_C * R_F * X_C_F ;

RA3 = S_F_i * R_F_i ;


RA4 = S_CF_on_O * R_CF * X_O_C ;

RA5 = S_CF_on_C * R_CF * X_C_C ;

RA6 = S_CF_i * R_CF_i ;


RA7 = S_CF2_on_O * R_CF2 * X_O_C ;

RA8 = S_CF2_on_C * R_CF2 * X_C_C ;

RA9 = S_CF2_i * R_CF2_i ;


RA10 = S_CF3_on_O * R_CF3 * X_O_C ;

RA11 = S_CF3_on_C * R_CF3 * X_C_C ;

RA12 = S_CF3_i * R_CF3_i ;
```

```
RA13 = S_C2F3_on_O * R_C2F3 * X_O_C ;

RA14 = S_C2F3_on_C * R_C2F3 * X_C_C ;

RA15 = S_C2F3_i * R_C2F3_i ;


RA16 = S_C2F4_on_O * R_C2F4 * X_O_C ;

RA17 = S_C2F4_on_C * R_C2F4 * X_C_C ;

RA18 = S_C2F4_i * R_C2F4_i ;


RA19 = S_C2F5_on_O * R_C2F5 * X_O_C ;

RA20 = S_C2F5_on_C * R_C2F5 * X_C_C ;

RA21 = S_C2F5_i * R_C3F5_i ;


RA22 = S_C3F3_on_O * R_C3F3 * X_O_C ;

RA23 = S_C3F3_on_C * R_C3F3 * X_C_C ;

RA24 = S_C3F3_i * R_C3F3_i ;


RA25 = S_C3F5_on_O * R_C3F5 * X_O_C ;

RA26 = S_C3F5_on_C * R_C3F5 * X_C_C ;
```

```
RA27 = S_C3F5_i * R_C3F5_i ;


RE1 = B_SiF2 * (X_F * 2*X_Si / (2*X_Si + 3*X_C)) ;

RE2 = B_SiF4 * (X_F * 2*X_Si / (2*X_Si + 3*X_C))^2 ;

RE3 = B_CO * X_O * 3*X_C / (2*X_Si + 3*X_C) ;

RE4 = B_CO2 * (X_O * 3*X_C / (2*X_Si + 3*X_C)) ;

RE5 = B_CF * X_F * 3*X_C / (2*X_Si + 3*X_C);

RE6 = (A_CF * (X_F * 3*X_C / (2*X_Si + 3*X_C) * X_F)) * R_F ;

RE7 = B_O * (X_O)^2   ;

RE8 = B_F * (X_F)^2   ;


RS1 = Y_Si * X_Si ;

RS2 = Y_O * X_O ;

RS3 = Y_C * X_C ;

RS4 = Y_F * X_F ;


RY_AD = (1/3)*(RF + 2*RCF + 3*RCF2 + 4*RCF3 + 5*RC2F3 + 6*RC2F4 + 7*RC2F5 +
6*RC3F3 + 8*RC3F5) ;

RY_E = RE1 + (5/3)*RE2 + (2/3)*RE3 + RE4 + RE5 + (5/3)*RE6 + (2/3)*RE7 +
(2/3)*RE8 + (1/3)*(RS1 + RS2 + RS3 + RS4) ;
```

```
 RY1 = RY_E - RY_AD ;


 $X_Si = -RE1 - RE2 - RS1 + RY1 ;

 $X_O = -RE3 - 2*RE4 -2*RE7 - RS2 + 2*RY1 ;

 $X_C = RCF + RCF2 + RCF3 + 2*RC2F3 + 2*RC2F4 + 2*RC2F5 + 3*RC3F3 + 3*RC3F5 -
RE3 - RE4 - RE5 - RE6 - RS3 ;

 $X_F = RF + RCF + 2*RCF2 + 3*RCF3 + 3*RC2F3 + 4*RC2F4 + 5*RC2F5 + 3*RC3F3 +
5*RC3F5 - 2*RE1 - 4*RE2 - 2*RE5 - 4*RE6 - 2*RE8 - RS4 ;

#  F_Si = X_F / X_Si ;
#  C_Si = X_C / X_Si ;
#  F_C = X_F / X_C ;



END # end of model block


SIMULATION Etch_Simul

OPTIONS
  DYNPRINTLEVEL := 1 ;
  DYNATOLERANCE := 1.0e-5 ;
  DYNRTOLERANCE := 1.0e-5 ;

UNIT
  Etch AS Series_Reactions

SET


  WITHIN Etch DO
```

```
N2I          := 157.75 ;

R_F          :=  0.2544 * N2I ;
R_CF         :=  0.0119 * N2I ;
R_CF2        :=  0.0493 * N2I ;
R_CF3        :=  0.3312 * N2I ;
R_C2F3       :=  0.0068 * N2I ;
R_C3F3       :=  0.0069 * N2I ;
R_C2F4       :=  0.0695 * N2I ;
R_C2F5       :=  0.1757 * N2I ;
R_C3F5       :=  0.0114 * N2I ;

R_F_i        := 0.05159 ;
R_CF_i       := 0.049354 ;
R_CF2_i      := 0.463803 ;
R_CF3_i      := 0.015095 ;
R_C2F3_i     := 0.0 ;
R_C2F4_i     := 0.088614 ;
R_C2F5_i     := 0.296285 ;
R_C3F3_i     := 0.015095 ;
R_C3F5_i     := 0.03526 ;
R_Ar_i        := 0.0 ;


S_F_on_Si    := 0.7 ;
S_F_on_C     := 0.7 ;

S_CF_on_C    := 0.7 ;
S_CF_on_O    := 0.7 ;

S_CF2_on_C   := 0.7 ;
S_CF2_on_O   := 0.7 ;

S_CF3_on_C   := 0.7 ;
S_CF3_on_O   := 0.7 ;
```

```
S_C2F3_on_C := 0.0 ;
S_C2F3_on_O := 0.0 ;

S_C2F4_on_C := 0.0 ;
S_C2F4_on_O   := 0.0 ;

S_C2F5_on_C := 0.0 ;
S_C2F5_on_O   := 0.0 ;

S_C3F3_on_C := 0.0 ;
S_C3F3_on_O := 0.0 ;

S_C3F5_on_C := 0.0 ;
S_C3F5_on_O   := 0.0 ;


S_F_i         := 1.0 ;
S_CF_i        := 1.0 ;
S_CF2_i       := 1.0 ;
S_CF3_i       := 1.0 ;
S_C2F3_i      := 1.0 ;
S_C2F4_i      := 1.0 ;
S_C2F5_i      := 1.0 ;
S_C3F3_i      := 1.0 ;
S_C3F5_i      := 1.0 ;

B_SiF2        := 8.0 ;
B_SiF4        := 8.0 ;
B_CO          := 12.0 ;
B_CO2         := 0.0 ;
B_CF          := 9.0 ;
B_COF         := 0.0 ;
B_O           := 6.0 ;
B_F           := 6.0 ;
```

```
  Y_Si        := 0.3 ;
  Y_O         := 0.3 ;
  Y_C         := 0.3 ;
  Y_F         := 0.6 ;

  A_CF        := 5.0 ;

  END # within structure


PRESET

  WITHIN Etch DO
    # identifier      # default # lower # upper
    X_Si :=     0.34  :  -1e-1  : 1.0 ;
    X_O  :=     0.66  :  -1e-1  : 1.0 ;
    X_C  :=     0.0   :  -1e-1  : 1.0 ;
    X_F  :=     0.0   :  -1e-1  : 1.0 ;

  END

INITIAL

  WITHIN Etch DO
    X_Si = 0.34 ;
    X_O = 0.66 ;
    X_C = 0.0 ;
    X_F = 0.0 ;

  END

  SCHEDULE
    SEQUENCE
      CONTINUE FOR 100000.0

      DISPLAY Etch.X_Si
```

```
    DISPLAY Etch.X_O
    DISPLAY Etch.X_C
    DISPLAY Etch.X_F
    DISPLAY Etch.RY1


#     DISPLAY Etch.RE1
#     DISPLAY Etch.RE3


#     DISPLAY Etch.F_Si
#     DISPLAY Etch.C_Si
#     DISPLAY Etch.F_C


   END #sequence


END # end the SIMULATION block

# To have a steady state, adsorption on C < removal of C-F < adsorption on C
```

A.4 Mass Spectrometry Data

A.4.1 C_2F_6, 300 W RF coil power, varying pressure

Neutral composition

	5 mTorr	10 mTorr	20 mTorr	30 mTorr	40 mTorr	50 mTorr
F	0.2544333	0.1729	0.0586742	0.0378443	0.0260278	0.0190329
CF	0.0119284	0.0158013	0.0150433	0.0189109	0.0220659	0.0242011
CF2	0.0492845	0.0517521	0.0682011	0.1058392	0.1459103	0.1594309
CF3	0.3312073	0.3126	0.413005	0.4044037	0.3889249	0.3978884
C2F3	0.0068164	0.0101	0.0039922	0.0060497	0.0239625	0.0190102
C3F3	0.0069082	0.0058398	0	0	0.0775222	0.0666889
C2F4	0.0695387	0.0920623	0.1004244	0.0917634	0	0
C2F5	0.1756735	0.2214059	0.2490519	0.2374392	0.2339908	0.2362878
C3F5	0.0113865	0.0164828	0.0129245	0.0134193	0.0146709	0.0180309

Ion composition

	5 mTorr	10 mTorr	20 mTorr	30 mTorr	40 mTorr
CF	0.0515896	0.025735	0.0100157	0.0094826	0.021539
CF2	0.0493541	0.0134417	0.0034277	0.0041818	0.0111359
CF3	0.4638029	0.4920794	0.3784462	0.4252603	0.4536216
C3F3	0.015095	0.0303087	0.0503302	0.0197524	0.0080672
C2F4	0.0886142	0.1033072	0.1214939	0.0756126	0.0719193
C2F5	0.2962846	0.2255579	0.0972801	0.0383931	0.0929296
C3F5	0.0352597	0.1095701	0.3390063	0.4273172	0.3407874

The data represents mass spectrometry signal strength with arbitrary unit.

The neutral composition is shown in Figure 2.9 and the ion composition is shown in Figure 2.11

A.4.2 C_2F_6, 5 mTorr, varying RF power

Neutral composition

	200 W	300 W	400 W	500 W
F	0.1725759	0.1786889	0.1779829	0.1819416
CF	0.0174654	0.0190124	0.0219917	0.0220136
CF2	0.0937122	0.1130477	0.1241954	0.1379447
CF3	0.3996646	0.3980947	0.4029544	0.3976739
C2F3	0.0043866	0.0049981	0.0048191	0.0077041
C3F3	0	0	0	0
C2F4	0.0601833	0.0714289	0.0800298	0.0825084
C2F5	0.252012	0.2147293	0.1880268	0.1702138
C3F5	0	0	0	0

Ion composition

	200 W	300 W	400 W	500 W
CF	0.0316478	0.0539019	0.0725345	0.0783505
CF2	0.0290883	0.0510994	0.046033	0.0696688
CF3	0.4665917	0.5004533	0.4812858	0.495696
C3F3	0.008169	0.0132384	0.0191768	0.0206351
C2F4	0.0786018	0.0823495	0.0929532	0.0951489
C2F5	0.3388924	0.2668706	0.2494936	0.2155847
C3F5	0.0470091	0.0320871	0.0385231	0.0249161

The data represents mass spectrometry signal strength with arbitrary unit.

The neutral composition is shown in Figure 2.14 and the ion composition is shown in Figure 2.16

A.4.3 C_4F_8 + 80% Ar, 300 W RF coil power, varying pressure

Neutral composition

	5 mTorr	10 mTorr	20 mTorr	30 mTorr	40 mTorr
F	0.0065	0.0054202	0.0038546	0.0028345	0.0015592
CF	0.0239223	0.0375912	0.0324472	0.0287067	0.0226775
Ar	0.5816914	0.5986477	0.6386923	0.6741118	0.7135833
CF2	0.0970376	0.1511957	0.156202	0.1461047	0.1158981
CF3	0.0970776	0.0796246	0.0647414	0.0597635	0.0632188
C3F3	0.0183311	0.0157769	0.0093172	0.0080372	0.0065042
C2F4	0.0327107	0.0256044	0.0184312	0.0155794	0.0147427
C3F4	0.0207699	0.0190417	0.0120898	0.0084594	0.0058976
C2F5	0.0221416	0.0081996	0.0081122	0.008726	0.0119321
C3F5	0.0261669	0.0203717	0.0179444	0.0145474	0.0147103

Ion composition

	5 mTorr	10 mTorr	20 mTorr	30 mTorr	40 mTorr
C	0.0156064	0.0050224	0	0	0
F	0.0012696	0	0	0	0
CF	0.3865512	0.5378486	0.6851426	0.7419656	0.726086
Ar	0.198276	0.0615899	0	0	0
CF2	0.1613648	0.111521	0.0445333	0	0
CF3	0.2065447	0.2554598	0.2703241	0.2580344	0.273914
C2F4	0.0259475	0.0183898	0	0	0
C3F5	0.0044398	0.0101684	0	0	0

The data represents mass spectrometry signal strength with arbitrary unit.

The neutral composition is shown in Figure 2.19 and the ion composition is shown in Figure 2.21.

A.4.4 C_4F_8 + 80% Ar, 5 mTorr, varying RF coil power

Neutral composition

	300 W	400 W	500 W
F	0.0065175	0.006774	0.0043072
CF	0.0371399	0.0296935	0.0238083
Ar	0.5376371	0.5683113	0.6011906
CF2	0.1547309	0.1338802	0.1127879
CF3	0.1015554	0.1191879	0.1259585
C3F3	0.0169565	0.0189682	0.0128869
C2F4	0.0368418	0.0226613	0.017681
C3F4	0.0221015	0.0220031	0.01537
C2F5	0.0113077	0.0146218	0.0164814
C3F5	0.0293522	0.0170702	0.0127933

Ion composition

	300 W	400 W	500 W
C	0.019436	0.03373	0.0466281
F	0.0015191	0.0042587	0.008182
CF	0.3821097	0.316706	0.2738664
Ar	0.1916423	0.2619903	0.3133004
CF2	0.1484964	0.1532267	0.1508323
CF3	0.2069137	0.2155571	0.197081
C2F4	0.0363914	0.0145312	0.0101098
C3F5	0.0134914	0	0

The data represents mass spectrometry signal strength with arbitrary unit.

The neutral composition is shown in Figure 2.24 and the ion composition is shown in Figure 2.26.